

Fatima-GB: Searching Clarity within Marine Fog

H.J.S. Fernando¹, C. Dorman¹³, E. Pardyjak¹⁶, L. Shen¹⁵, Q. Wang⁷, E. Creegan³, S. Gaberšek⁸, I. Gultepe^{1,11}, S. Hoch¹⁶, L. Lenain¹³, D. Richter¹, R. Chang⁵, T.C. VandenBoer¹⁷, S. Bardoel¹, A. Barve¹⁵, B. Blomquist⁹, T. Bullock⁶, Z. Chen¹⁷, L. Colosi¹³, R.S. Coppersmith¹, I. Crawford¹⁴, L.R. Crilley¹⁷, R. Dimitrova¹, A. Dowling¹, D. Eleuterio¹⁰, S. Fiorino², M. Gallagher¹⁴, N. Gapp¹², G. Giacosa⁵, A. Grachev³, L. Grare¹³, T. Hintz¹, C. Hocut³, K.Y. Huang¹, O. Hyde¹, K. Keefer², D.G. Ortiz-Suslow⁷, A. Perelet¹⁶, W. Perrie⁴, J. Ruiz-Plancarte⁷, L. Salehpoor¹⁷, D. Singh¹⁶, N. Statom¹³, P. Taylor¹⁷, S. Wang¹, R. Yamaguchi⁷

¹University of Notre Dame, Notre Dame, IN 46556, USA

²Air Force Institute of Technology, Wright Patterson Air Force Base, Dayton, OH 45433, USA

³Army Research Laboratory, White Sands Missile Range, NM 88002, USA

⁴Bedford Institute of Oceanography, Dartmouth, NS B2Y 4A2, Canada

⁵Dalhousie University, Halifax, NS B3H 4R2, Canada

⁶Digital Environment, WSP Canada Inc., St. John's, Newfoundland & Labrador, A1B 3X4, Canada

⁷Naval Postgraduate School, Monterey, CA 93943, USA

⁸Naval Research Laboratory, Monterey, CA 93943, USA

⁹NOAA Physical Sciences Laboratory, Cooperative Institute for Research in Environmental Sciences, University of Colorado, Boulder, CO 80305, USA

¹⁰Office of Naval Research, Arlington, Virginia, VA 22203-1995, USA

¹¹Ontario Technical University, Oshawa, ON L1G 0C5, Canada

¹²Science Applications International Corporation (SAIC), San Diego, CA

¹³Scripps Institution of Oceanography and University of California, San Diego, CA 92037

¹⁴University of Manchester, Manchester, M13 9PL, UK

¹⁵University of Minnesota, Minneapolis, MN 55414, USA

¹⁶University of Utah, Salt Lake City, UT 84112, USA

¹⁷York University, Toronto ON, M3J 1P3, Canada

Corresponding Author:

Harindra J.S. Fernando

Departments of Civil and Environmental Engineering and Earth Sciences,
and Aerospace and Mechanical Engineering

University of Notre Dame, Notre Dame, IN 46556

Phone: 574-631-9346; Fax: 574-631-9236

e-mail: fernando.10@nd.edu

Abstract

39
40
41
42
43
44
45
46
47
48
49
50
51
52
53
54
55
56
57
58
59
60
61
62
63

Fog constitutes a thick, opaque blanket of air hugging the Earth's surface, laden with small water droplets or ice crystals. Fog disrupts transportation, poses security threats, disorients human perception and impacts communications and ecosystems. Collusion of atmospheric, terrestrial and hydrologic processes produces fog droplets that pullulate over hygroscopic aerosols that act as condensation nuclei. Marine fog is particularly complex, since underlying dynamic, thermodynamic and (bio)physicochemical processes span fifteen decades of spatial scales, from megameter-sized synoptic weather systems to nanometer-scale bioaerosols. This paper overviews the first international field campaign (Fatima-GB) of the project dubbed Fatima (Fog and turbulence interactions in the marine atmosphere) conducted during 01-31 July, 2022 in the Grand Banks region of North Atlantic. Therein, weather systems and commingling cold and warm oceanic waters provide entrée for fog genesis. Measurement platforms included an islet southwest of Nova Scotia (Sable Island), a research vessel (Atlantic Condor), an offshore Oil Platform and autonomous surface vehicles. The instrument array comprised of extant remote and in-situ sensors augmented by novel sensing systems prototyped and deployed in marine fog to penetrate the smallest scales of turbulence, examine aerosols, and quantify radiation budget. The comprehensive data set so gathered, together with satellite and reanalysis products, mesoscale-model and large-eddy simulations demonstrated that the long-held hypotheses of marine fog formation by warm air advection over colder water and in areas of enhanced (shelf) turbulence need to be revisited. The study also elicited new phenomena, for example, the Fog Shadow (clearings of fog downstream of islands).

64 **Significance Statement**

65 Fog research has escalated recently per climate-change implications and directed-energy
66 (electromagnetic systems) applications. Here we report selected findings of Fatima-GB, a
67 comprehensive multidisciplinary field campaign conducted in Grand Banks, one of the world's
68 foggiest areas, for improving the understanding and predictability of marine fog. Our findings
69 indicate historical understanding of marine-fog lifecycle requires a fundamental rethink to
70 incorporate complexities of scale interactions. Fog covers 15 decades of spatial scales, wherein
71 megameter-scale synoptic systems sway millimeter-scale turbulent eddies, within which
72 micron-scale fog droplets spawn on either tens (bioaerosols) or hundreds (sea salt) of
73 nanometers sized marine aerosols. We demonstrate the collusion of meteorological,
74 oceanographic, turbulence, thermodynamic and (bio)physicochemical processes during marine
75 fog evolution, which should help develop future sub-grid parameterizations for numerical
76 weather prediction models (NWPs).

77

78 Introduction

79 Fog is a collection of small airborne water droplets (size $\sim 1\text{-}30\ \mu\text{m}$) that forms near the
80 earth's surface when an air mass becomes cooled and saturated, causing the horizontal near-
81 surface visibility to drop below 1km (Myers 1968, WMO 1992). Aerosols are essentials for fog
82 genesis, since they form the substrate (or fog condensation nuclei FCN) on which water vapor
83 condenses to form droplets (Pruppacher and Klett 2010). The droplet growth is dependent on
84 the (bio)physiochemical properties of atmospheric aerosols, meteorology, radiative forcing and
85 turbulence. Hygroscopic aerosols are considered 'activated' when droplets reach a size
86 conducive for further growth (Gerber 1981; Poku et al. 2019), while un-activated aerosols take
87 up water and may remain airborne or settle through deposition processes (Farmer et al. 2021).

88 While the physical appearance of fog and clouds is nominally the same, profound
89 dynamical differences exist between the two, due mainly to the earth's surface influence on
90 fog. Fog occupies the lower Atmospheric Boundary Layer (ABL), and processes therein
91 undergird the *lifecycle* of fog, namely, the formation, evolution/maturation and dissipation
92 (Nakanishi 2000). The vertical air velocities in the lower ABL are much smaller than the
93 horizontal velocities, causing fog to be deprived of the main cooling mechanism that drives
94 clouds: adiabatic expansion of ascending air (Rodhe 1962). Instead, fog relies on surface
95 processes such as ground radiative cooling, moisture/heat fluxing, mixing of air masses, and
96 surface turbulence (MacDonald et al. 2020). Additionally, such local mechanisms are
97 synoptically regulated, making fog a veritable multiscale phenomenon across a wide spatial
98 continuum of fifteen decades – from global ($10^7\ \text{m}$) to microphysical (aerosols, $10^{-8}\ \text{m}$) scales.

99 Fog is broadly [and probably subjectively] classified into three categories: radiation,
100 advection and mixing fogs (Fernando et al. 2021). Nocturnal radiative cooling of a moist
101 surface air layer leads to *radiative fog*. Advection of warmer air over colder water causes
102 *advection fog*. Nonlinear mixing between nearly saturated warm and colder air masses
103 produces *mixing fog* (Taylor 1917). Special categories are also common, for example, clouds
104 of ice crystals near the surface (*ice fog*), fog droplets freezing on surfaces (*freezing fog*), steam
105 streaks arising within colder fog (*steam fog*), rain evaporating into drier air (*precipitation fog*)
106 as well as location-based fogs such as valley, upslope and land fogs (Gultepe et al. 2016; Pu et
107 al. 2023). Location fogs also include fog in the Marine ABL (MABL), *Marine Fog* – a type of
108 extreme complexity and amongst the least predictable in meteorology.

109 Contributing to intricacy of marine fog are a myriad of upper-ocean, air-sea interaction
110 and MABL processes illustrated in Fig. 1. Additional phenomena may appear at the transition

111 between ocean and land (Coastal Zone). Koračin et al. (2014) and Koračin & Dorman (2017)
 112 provide extensive reviews of marine fog. Coastal fog has been studied extensively, e.g., along
 113 the US West (Leipper 1994) and East coasts (Fernando et al. 2021) and elsewhere (Spirig et al.
 114 2019). Both the *Sea Fog*, marine fog in the shallower “green” water away from the coastal
 115 zone, and *Open-Ocean Fog* over the deeper “blue” water remain under-researched. The
 116 megaproject described in this article, dubbed Fog and turbulence interactions in the marine
 117 atmosphere (Fatima), shifts attention to these understudied deeper waters, and explores new
 118 frontiers of knowledge on Sea Fog; see Appendix A. For general acronyms, see Appendix L.

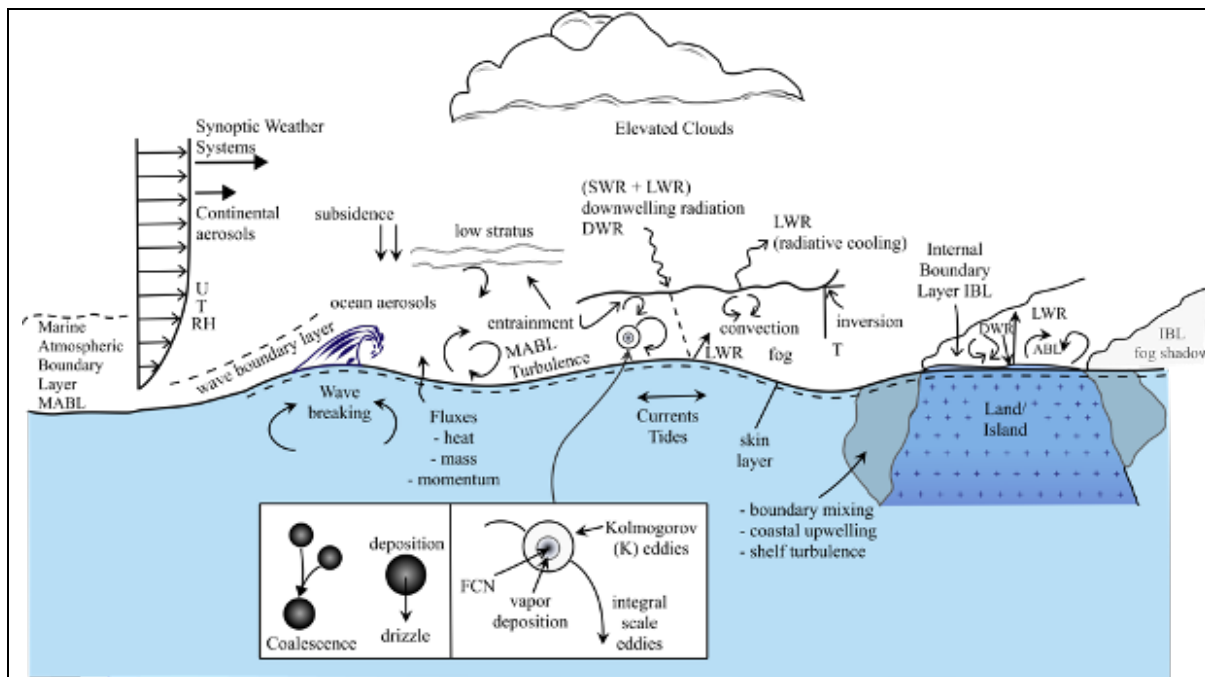


Figure 1: Marine Fog Processes - Advected continental or marine hygroscopic aerosols act as FCNs. Water droplets grow around FCNs by diffusional deposition of vapor (inset). Kohler (1936) argued that droplet growth requires exceeding of a critical radius determined by opposing effects of surface tension and solute concentration (whence droplet vapor pressure increase/decrease, respectively). The role of smallest turbulent (Kolmogorov or K) eddies in the ABL, within which FCNs are imbedded, however, is yet to be understood (inset). Note that, for the air, K scales and (Obukhov-Corrsin O-C) temperature dissipation scales are of the same order, and hence temperature within the K eddies or immediately surrounding FCNs is homogeneous. Spawning droplets undergo coalescence and settling (inset). Contributing upper-ocean processes/phenomena include waves and breaking, nocturnal convection, turbulence and mixing, tides, and currents. The corresponding lower-atmospheric phenomena include wave boundary layer and shear and convective turbulence. At the air-sea interface, turbulent heat, mass, momentum and aerosol exchanges occur by wave breaking and surface renewal via [molecular] skin layer, which fuel air-sea interactions. Short/Long Wave Radiative (SWR/LWR) and advective processes also affect Sea Surface Temperature (SST). Vital contributions of MABL come from synoptic and mesoscale [advective] systems including fronts, highs and lows, inversions, heating/cooling of the sea surface and fog top, diel cycle, clouds, turbulence and aerosols. If present, coastal contributions from boundary mixing, upwelling, escalated wave breaking, land/ocean [differential] heating, and internal boundary layers (IBL) have significant impacts on fog life cycle.

119 Low visibility in fog disrupts all modes of transportation, critical industrial operations
120 such as oil platforms and free-space optical communications (Gultepe et al. 2009). The
121 hazardous human health impacts of chemically active, pollutant-trapped, *smoky fog* (smog and
122 thicker super fogs, visibility < 3.3 m) have been well documented (NWS 2024). Coastal fog
123 has profound ecological consequences (Torregrosa et al. 2014). Marine fog is considered as an
124 ‘unknown’ in asymmetric warfare, for example, when a swarm of small boats or UAVs are the
125 blurred threat whence, for defense, directed energy systems such as High Energy Lasers (HEL)
126 and optically-guided weapons are tools of choice (Pawlak 2012; Niece & Kaiser 2018). The
127 shorter the wavelength, the higher the intensity of Lasers on the target (Jumper & Gordeyev
128 2017), and thus HELs applications prefer near-IR and visible wavelengths; such beams are
129 stymied by the presence of fog (Perram et al. 2010). Fog is also evaluated as a potable water
130 source amidst dwindling water supplies due to climate change (Bhushan 2020).

131 Understanding the nexus between fog, aerosols, radiation, flow and turbulence is
132 critical for prediction of fog life cycle. Notwithstanding, owing to lack of high-resolution data
133 and solid theoretical bases, NWP models employ parameterizations based on cloud-research for fog
134 prediction, and unsurprisingly struggle for accuracy (Gultepe et al. 2006, Van der Velde et al.
135 2010; Boutle et al. 2018). Modeling studies typically invoke similarities between stratocumulus
136 clouds and fog (Karimi 2020). Thus, melding of knowledge from multiple disciplines --
137 meteorology (ABL and free atmospheric flow), fluid mechanics (advection, turbulence and
138 instabilities), thermodynamics (heat transfer), microphysics (aerosols and droplets) and
139 (bio)geochemistry (gas-aerosol production, interactions and transformations) -- is imperative
140 for improvements in fog prediction, which was the approach used in Fatima.

141 Fatima focused on two geographical areas of highest summer marine fog occurrences
142 in the world. Based on climatology maps, Dorman et al. (2017) identified sixteen fog maxima
143 over shallower water during the warm season. The two most prevalent (excluding anti-
144 access/area-denial) sites were the southeast of the Grand Banks off Newfoundland (~ 50 - 200
145 m water depth) with a peak fog occurrence of 45% during June-July-August (JJA) and the
146 Yellow Sea with 18% fog occurrence (~10 - 80 m depth, JJA); both belong to the Sea Fog
147 category. Field campaigns at both sites have been completed, with the Grand Banks Campaign
148 (Fatima-GB) during 01-31 July 2022 and Fatima-YS during 20 June – 08 July 2023. Given
149 different basin, geographic and synoptic settings, stark disparities between fog-genesis
150 mechanisms (e.g., oceanic versus continental aerosols) were expected from the two sites.

151

152 Given the intrinsic merits of each campaign, this article exclusively concerns Fatima-
153 GB. Dorman et al. (2017, 2020) hypothesized that southerly/southwesterly airflow over the
154 negative SST gradients in Grand Banks, caused by mingling between Gulf Stream and
155 Labrador waters, are important contributors to Sea Fog therein (Appendix A). Contrary to
156 common belief that fog correlates with low ABL turbulence, the fog maximum in Grand Banks
157 occurs at relatively higher median wind speeds (Isaac et al. 2020) and elevated turbulence
158 levels associated with cyclonic systems passing over toward the North Atlantic. This article
159 summarizes the execution and a few representative results of Fatima-GB, simultaneously
160 covering synoptic to microscales – a pioneering study of its kind. Continuing challenges to Sea
161 Fog research are also discussed.

162 **Design and Execution of Fatima-GB**

163 Capturing larger-scale weather systems down to K scales (Van der Hoven 1957) and
164 investigating regions of enhanced oceanic turbulence apropos of Grand-Banks summer fog
165 were the principal design considerations. The selected geographic area of the campaign and the
166 Canadian Research Vessel, Atlantic Condor (R/V-Condor), that traversed the domain are
167 discussed in Appendix B. The principal measurement locations were the (i) Grand Banks, a
168 region with complex topography on the North American Continental Shelf, and (ii) Sable
169 Island, an isolated, Canadian-owned, croissant shaped sand bar well exposed to the advection
170 path of fog. Both R/V-Condor (Fig. 2) and Sable Island (Fig. 3; Appendix C) were densely
171 instrumented for capturing synoptic to mesoscale weather and ABL parameters such as
172 turbulence and fluxes, turbulent kinetic energy (TKE) and temperature-fluctuation dissipations
173 at K and O-C scales (at Sable), radiation, water vapor and hydrometeors, visibility, electro-
174 optic and electro-magnetic (at Sable) propagation, (bio)physicochemical properties of aerosols,
175 SST, hydro-physical and turbulence properties of upper ocean, and surface waves. Continuous
176 meteorological and visibility data from cooperating offshore installations (e.g., Hibernia oil
177 platform) were also available. Instruments are listed below, and further elaborated in Appendix
178 K with acronyms. For research group acronyms, see Appendix A.

179 ***Instrumentation on R/V-Condor (Fig. 2)***

180 ***Instruments:***

181 **UND:** Microwave Rain Radar (MRR-PRO), Microwave Radiometer (MWR), Uprising
182 Vertical Microstructure Profiler (VMP-250), Optical Disdrometer, CTD, 300-kHz ADCP, Sea
183 Snake, Visible and Cloud/IR cameras, Remote Ocean Sensing Radiometer (ROSR), FD70
184 Visibility Sensor, Ceilometer-CL61

185 NPS: Small Moored Wave Buoy, Rawinsondes, Surface and Scene Visualization Cameras
186 UU: Pyrgeometer and Optical Particle Counter (OPC-N3) for Tethered Lifting System (TLS)
187 DU: Fog Water Collector, Scanning Mobility Particle Sizer (SMPS), Aerodynamic Particle
188 Sizer (APS), Fog Monitor FM120
189 YorkU: Micro Orifice Uniform Deposit Impactor (MOUDI), Nano-MOUDI-II, Ion
190 Chromatograph, Gas Monitors
191 AFIT/NPS: Integrating Nephelometer, Black Carbon Aethalometer, Condensation Particle
192 Counter (CPC)
193 *Instrument Systems:*
194 UND: Doppler Lidar and W-Band (cloud) Radar, both on motion stabilized platforms
195 PSL-NOAA/UND: Bowmast (3D-Sonic, LiCOR-7500, Weather Transmitter WXT520, GPS,
196 Pressure (HMP), Pyrgeometer, Pyranometer)
197 UU/ARL/UND: TLS with Meteorological and Turbulence packages. Gimballed Pyrgeometer
198 NPS: C-CAMS [Crane-based Cloud and Aerosol Measurement System - an in-house
199 developed fog/aerosol/turbulence sampling system measuring CO₂ and water vapor
200 fluctuations (IRGASON), Platform Motion (VN-300), Pressure fluctuations (MET4A),
201 Radiometric SST (CT-15), Relative humidity (RH) and Temperature (T) (HMP155),
202 Visibility and meteorology (CS-125), Upwelling Radiation (Infrared Pyranometer), Net
203 Radiation, Surface elevation (Radar Altimeter), Aerosol Absorption (Soot Photometer),
204 Aerosol size spectra (Portable Optical Particle Spectrometer, POPS), Fog droplet parameters
205 (FM120)], D-CAMS (same as C-CAMS but Deck-mounted)
206 OntTechU: Backscatter Cloud Probe (BCP) and Cloud Droplet Probe (CDP-2) on the Gondola
207 Platform
208 Scripps/UCSD: Instrumented wave gliders [3D Sonic, WXT530, CTD, Profiling CTD,
209 300KHz ADCP, Current Profiler, Dual-GPS receiver, GPS-IMU]; and Uncrewed Surface
210 Vessel [A/V Wallace, L3Harris C-Worker-5 with 2xSonics on a Flux Mast, FM120, Towed
211 CTD, 500 Hz ADCP, Visible and IR 360 Cameras, X-band Radar]
212

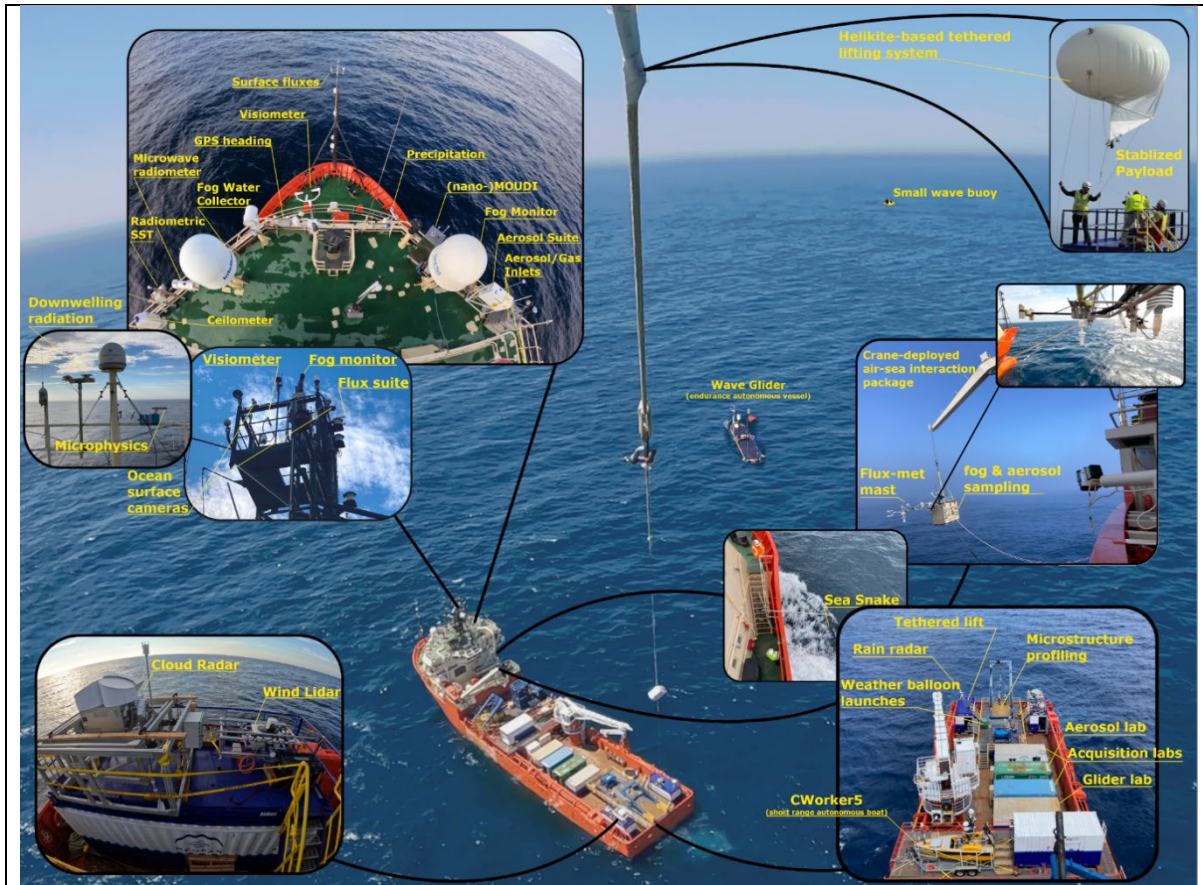


Figure 2: Instrumentation on R/V-Condor. This deep-sea supply vessel was converted to a research vessel by the Fatima group after extensive retrofitting. R/V-Condor was on lease from the Atlantic Towing Ltd. through the MEOPAR (Marine Environmental Observation, Prediction and Response), a Canadian National Network of Centers of Excellence on marine research. It was made available at a time when US vessels were unavailable due to Covid-related postponements/queuing.

213 **Sable [Island] Campaign (Fig. 3)**

214 Sable has an average width of ~ 700m (1.2 km at its widest point), length ~ 40 km, and
 215 is characterized by relatively simple topography with maximum elevation 30 m, minimal
 216 geographic changes from ocean to land, and low (~ 1 m height) grass coverage without
 217 vegetation. Being devoid of human footprint (i.e., anthropogenic heat and factitious elements
 218 that may alter fog thermodynamics), Sable is an ideal location to study marine fog and land
 219 interactions. Operated by the Parks Canada Agency as a strict Nature Reserve, it is a migratory
 220 bird sanctuary for over 2500 pairs each of terns and gulls nesting and breeding in the summer.
 221 During Fatima-GB, Sable was the homestead for 569 feral horses, with beaches roamed by a
 222 colony of harbor and grey seals.

223 Appendix C shows a plan view of Sable Island, along with two main deployment areas
 224 (Main Station and West Light), instruments and their owners. The Main Station was operated
 225 remotely, without disturbing tern nests that may eschew bird strikes. The backbone of West Light
 226 was an array of three (North, Center and South) towers along the climatologically streamwise

227 (southwest - northeast) transect, with instrument clusters surrounding them. Parks Canada
228 required strict compliance with Canadian ecological conservation ordinances, accompanied by
229 permits. Accordingly, instrument clusters were located in Parks-approved areas of little to no
230 protected vegetation within electric-fenced enclosures to safeguard both the horses and
231 equipment. Food and power are not available at Sable, and Parks-provided gas-powered
232 generators were the electricity source. Routine charter aircraft services (and occasional
233 helicopters in bad weather) were the reliable transportation link between mainland and Sable.
234 An eight-member research team occupied an existing house in the West Light, with supplies
235 flown in from Halifax. According to Parks Canada, Fatima-GB was the first large-scale
236 meteorological field study ever conducted at Sable. The instrumentation listed below including
237 acronyms are further detailed in Appendix K.

238 Instruments:

239 UND: FD70, PWD22 Visibility Sensors, Scanning Doppler Lidar, Net Radiometers, LiCOR,
240 Sonics, Fine Wire T/RH sensors, Ceilometer-CL31.

241 NPS: MWR, Sodar, Scintillometer, Differential Image Motion Monitor, Wide Angle
242 (Telerradiometric) Transmissometer, Non-coherent Extended Source Beacon,
243 Rawinsondes, TLS, CS120 Visibility Sensor, CDP, transmissometer, differential temperature
244 sensors, IRGASON, video cameras

245 UU: MRR-PRO, Ceilometer-CL31, Infrared Electromagnetic Propagation System
246 (Scintillometer-BLS900), Microwave Scintillometer (RPG-MWSC-160), OPC-N3, visibility
247 cameras, Liquid Water Content (LWC) probes, Soil Heat Flux Sensor, Soil moisture and
248 temperature T Sensor (CS650), Soil T probe, CS125

249 AFIT: Cloud Ice Nucleation Characterization System (CINCS)

250 UMAN: Multi-parameter Bioaerosol Spectrometer (MBS)

251 Instrumented Systems:

252 UND: Super Combo Probe (In-house built) to capture T and scalar dissipation in turbulence

253 NPS/UU: TLS with temperature, RH, wind speed/direction, pressure, OPC-N3, pyrgeometer

254 UU/UND: Flux towers

255 UU: LEMS Automated Weather System; Precision Radiation Balance Sawhorse (4
256 components of SW, LW and net radiation)

257 OntTechU: Unmanned Aerial System UAV (with T, P, RH, OPC-N3 probes), Microphysics
258 Supersite (Ceilometer-CL51, WXT520, PWD52, FM120, Ground Cloud Imaging Probe
259 (GCIP), 3D Sonic, Sunshine Pyranometer, Digital Camera for local view)

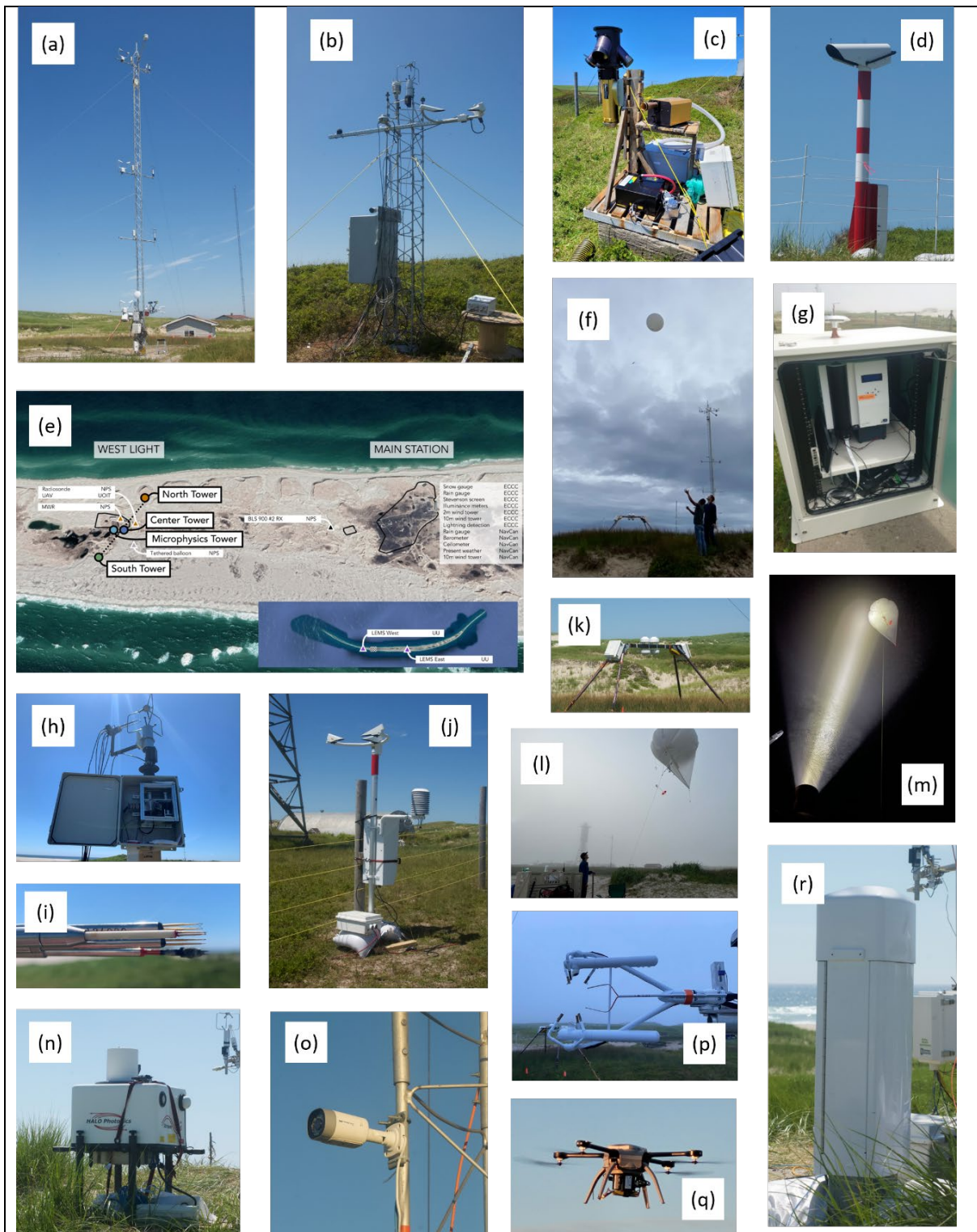


Figure 3: A sample of instruments at Sable. (a) The central flux tower; (b) the microphysics tower; (c) FM120 and GCIP; (d) Transmissiometer (LT31); (e) map showing the tower transect and two satellite sites; (f) rawinsonde releases; (g) CINCS; (h) Super combo system for TKE and T dissipation measurements; (i) Super combo probe ensemble; (j) FD70; (k) radiation balance measurements on saw-horse structure; (l) TLS profiling system; (m) TLS profiling with fog/mist visualization using a powerful flashlight; (n) Halo Photonics Doppler wind Lidar; (o) webcam; (p) LWC probe within an IRGASON probe volume; (q) UAV with meteorological instruments; (r) Vaisala CL31 ceilometer. Instruments on each tower are also in Appendix C.

261 WXT520, CL31) at 1 minute, mixed with 15 minute and 1-hour data were provided by the
 262 Hibernia site during June-August 2022.

263 **Intense Operational and Study Periods (IOPs and ISPs)**

264 Although most instruments operated continuously, expensive, labor-intensive, and
 265 high-maintenance systems such as high-frequency rawinsonde launches (8-24/day instead of
 266 4/day), VMP-250 and C-CAMS were operated only during IOPs. In general, IOPs were called
 267 during [virtual] weather briefings conducted daily at 1300 ADT by a group of ~ 13-20
 268 participants. For guidance, NRL used COAMPS^{®1} operational mesoscale model at 1 km
 269 resolution with initializations at 48, 24 and 12 hrs ahead (Hodur 1997). YorkU used WRF
 270 model (Skamarock et al. 2008) with 10 km resolution, generating simulations from 1800 UTC
 271 to 1800 UTC next day after a spin-up time of 12 hrs. Both models used Global Forecast System
 272 (GFS) model for initial and boundary conditions, and generated hourly forecasts. Horizontal
 273 maps and vertical profiles at selected locations were examined. Also used were GFS (resolution
 274 0.25°) output, GOES Satellite Imagery, Weather Radar, RAOB and NOAA HYSPLIT back-
 275 trajectories (UCSD and OntTechU). For Sable, an IOP was invoked by group consensus when
 276 conditions for capturing at least parts of the fog lifecycle appear favorable. IOPs typically lasted
 277 24-36 hours, except for propitious 72-hour “Super-IOPs.” Table 1 lists the IOPs. Fog (Visibility
 278 < 1 km) appeared during 9 of the 14 IOPs.

279 **Table 1:** IOPs for Sable Island (in Atlantic Daylight time ADT = UTC - 3 hrs.)

IOP #	Start (ADT)	End (ADT)	Hydrometeor Type (PWD22/FD70)	UAV	TBS	Rawinsonde frequency	Observer notes	Synoptic Set up
1	J03 1800	J04 1800	FG/BR/DRZ/RN	√	x	√ (3 hr)	Mix hydrometeors	HP/MX
2	J06 1800	J07 1800	DRZ/RN	√	x	√ (3 hr)	Rain/mist	CG/MX
3	J09 2100	J11 0130	BR/patchy fog	√	√	√ (3 hr)	IOP-wavy structures	LP/ST
4	J12_1800	J13_1500	CLR	x	√	√ (3 hr)	Failed fog/reference case/visibility fluctuations	LP/ST
5	J13_1800	J15_1500	BR/CLR	x	√	√ (3 hr)	Super-IOP, excellent FG event	HP/MX
6	J15 1500	J16 0900	FG/BR/DRZ/RN	x	x	√ (3 hr)	FG but windy	HP/ST
7	J17 1800	J18 1800	FG/BR/DRZ/RN	x	√	√ (3 hr)	FG front, Ext IOP	HP/ST
8	J18 1800	J20 0900	FG/BR/DRZ/RN	x	x	√ (3 hr)	FG and high wind	HP/ST
9	J21_1500	J22_1500	FG/BR	x	√	√ (3 hr)	Excellent FG formation/persistent	HP/ST
10	J23_1200	J25_1800	FG/BR/DRZ/RN	x	√	√ (3 hr)	Super IOP, Advection FG; strong winds; FG shadow predicted	HP/ST

¹COAMPS is a registered trademark of the U.S. Naval Research Laboratory

11	J26_0600	J27_0600	BR	x	x	√ (1 hr)	Late FG shadow possible, dissipates early morning	CG/MX
12	J28_2100	J28_2330	FG/BR/DRZ/RN	x	√	√ (12 hr)	Thin barely visible FG layer/BR, Radiation impact, light drizzle	CG/ST
13	J29_1600	J30_1800	BR/RN	x	√	√ (3 hr)	Post frontal FG/Stratus lowering/light rain after fog	LP/MX
14	J30_1800	J31_0900	FG/BR/RN	x	x	√ (3 hr)	Rain and 1.5 hr FG on next morning	LP/MX

280 J = July. BR, FG, DRZ, and RN signify mist, fog, drizzle, and rain conditions, respectively. HP, LP,
281 CG, MX, and ST refer to the high pressure, low pressure, convergence zone, mixing, and stable synoptic
282 conditions, respectively. Local conditions may change over the course of IOPs. Note that FG, BR, and
283 DRZ transitions (identified by FD70) are not very smooth and may be lumped all together.

284 Naturally, IOPs for Sable Island were not optimal for R/V-Condor, which trekked in
285 and out of fog (Figs. 4a-c). As such, suitable study periods, dubbed Intense Study Periods
286 (ISPs), were identified *posteriori* using the following criteria beneficial for later analysis: (i)
287 visibility < 1 km, (ii) relative wind direction within $\pm 60^\circ$ of the bow course, and (iii) ship speed
288 < 3 m s⁻¹ (and winds generally > 5 m s⁻¹). Fig. 4 shows the visibility, rawinsonde,
289 meteorological, and microphysical information for six ISP periods identified using above
290 criteria. A list of ISPs is in Table 2.

291 **Table 2:** ISPs at R/V Atlantic Condor

ISP	# of Rawinsondes	Start Time (UTC)	End Time	Comments
1	32	July 8, 06:10 am	July 14, 2:50 pm	Significant synoptic systems passing through (at the shelf break; Near Hibernia)
2	13	July 13, 03:10 pm	July 16, 07:00 pm	Approximately constant wind direction (at the shelf break; Near Hibernia)
3	15	July 21, 12:40 pm	July 23, 1:00 pm	Near Sable Island on the shelf
4	13	July 23, 09:00 pm	July 25, 08:30 pm	-ditto-
5	19	July 25, 09:30 pm	July 27, 01:30 pm	Sable Lee Observing Period (SLOP)

292

293

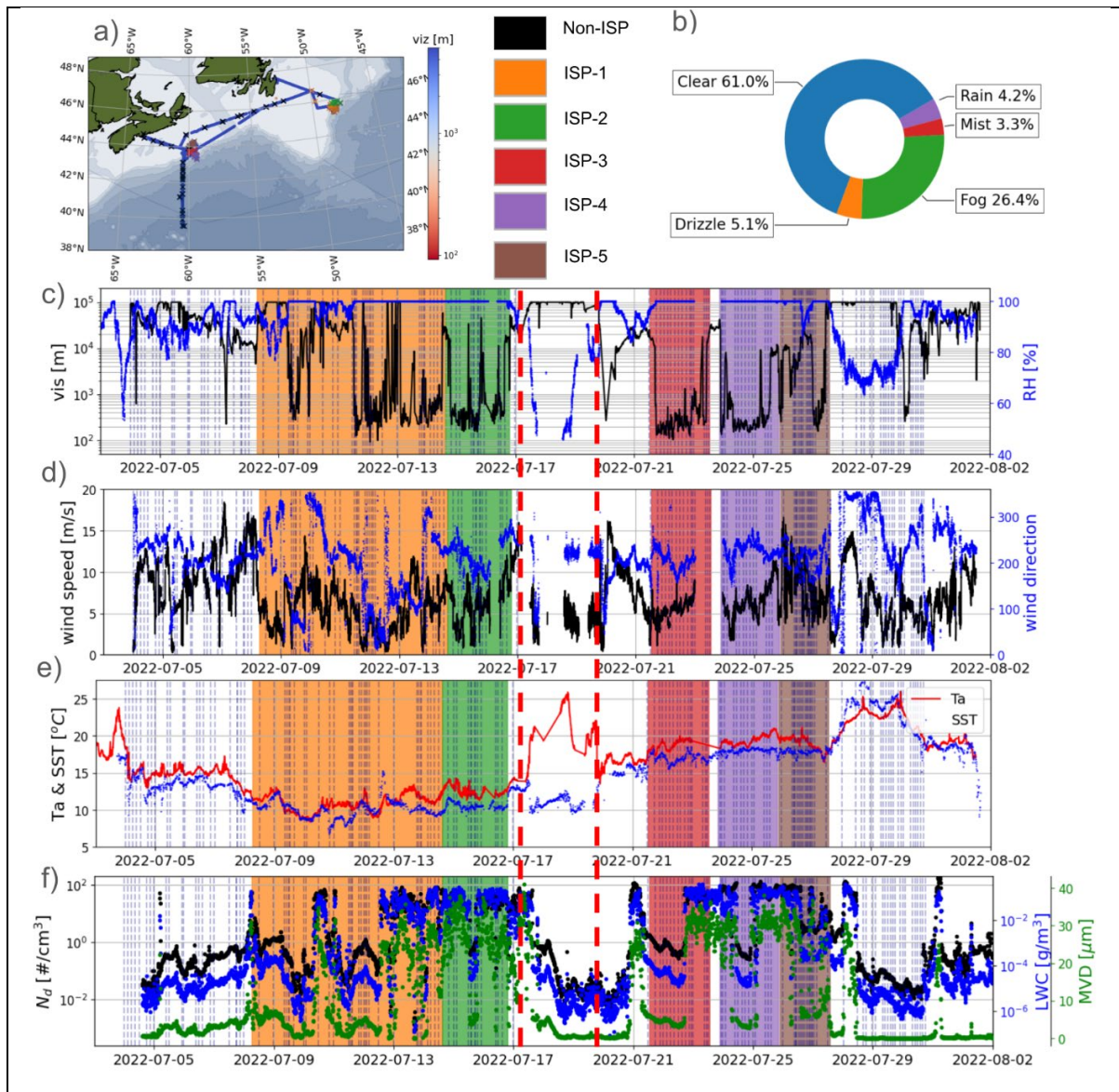


Figure 4: (a) Condor track with rawinsonde release locations (x), color at each location indicating visibility (from FD70); (b) Pie chart of hydrometeor status (FD70) during the campaign; (c) visibility (FD70) and ISP durations identified in color shading based on the criteria in the text (also see Table 2); (d) Ambient wind speed WS and direction WD (bow mast) (e) Air T and SST (bow mast and ROSR) (f) Aerosol number concentration (N_d), LWC (FM120) and Mean Volume Diameter (MVD). Red vertical broken lines demarcate the port call of R/V-Condor at St. Johns, Newfoundland. The vertical dashed lines indicate the times of radiosonde launches, corresponding to (a).

294 Data Repository

295 The primary means of data storage is a google drive, allowing quick and convenient
 296 access and secure cloud storage. At present, data from individual groups have been saved into
 297 a shared google drive. A mirrored hard drive is also maintained. Types of data being uploaded
 298 include raw data, processed intermediate data and quality-controlled data for improved
 299 accountability in data analysis. Supporting datasets such as satellite imagery and model

300 forecast/reanalysis used by the forecasting group are also catalogued and saved. All datasets
301 will be available for the science community after 01 August, 2025.

302 **General Observations**

303 In addition to those of R/V-Condor shown in Fig. 4, representative observations at or
304 near the Sable Island are shown in Fig. 5 as time series of meteorological, thermodynamic,
305 turbulence, microphysical, and surface variables from the central tower, a total of 182
306 soundings, and by the wave glider “Carson” operating in the shallow waters southwest of Sable
307 that provided nominal upwind upper-ocean and lower-atmospheric conditions. Shaded periods
308 in Fig. 5 (a-o) are IOPs. Note the (i) predominant southerly/southwesterly wind direction (a),
309 (ii) wind perturbations in response to diurnal temperature cycle at low wind speeds (a), (iii)
310 weak diurnal variability of SST and marine T_{air} (l); (iv) elevated LWC, MVD and N_d during
311 IOPs with fog, consistent with previous measurements (Gultepe et al. 2021) in marine fog in
312 North Atlantic (g-i); (v) [predominant southwesterly/westerly] winds punctuated by occasional
313 periods of heightened wind speeds aloft up to 20 m s^{-1} (p); and (v) persistently moist air ($\text{RH} >$
314 80%) with propensity for saturation that frequently extends beyond 1.5 km (r). Extensive
315 campaign-wide data of the ilk illustrated in Figs. 4 and 5 have motivated a variety of ongoing
316 process- and numerical studies.

317 The daily averaged aerosol number concentration on the R/V-Condor is shown in Fig.
318 6a for both fog and no fog conditions. During 04-17 July, the R/V-Condor was in Grand Banks
319 away from Sable Island (dubbed Grand-Banks Period) whereas it was in the vicinity of Sable
320 Island during 19 July – 01 August (Sable Period). A larger aerosol concentration occurred in
321 coastal areas close to Nova Scotia during 03-04 and 30-31 July, around Sable (21-25 July), and
322 towards the Gulf Stream (27-29 July). Lower aerosol concentrations were observed in Grand-
323 Banks (10-13 July), suggesting less continentally-influenced air, consistent with the CO
324 measurements shown in Fig. 6b. In contrast, a higher aerosol concentration occurred in coastal
325 areas close to Nova Scotia during 03-04 and 30-31 July, around Sable (21-25 July), and towards
326 the Gulf Stream (27-29 July), suggesting more pollution influence, also consistent with the CO
327 measurements (Fig. 6b).

328 Overall, $< 100 \text{ nm}$ aerosols accounted for $\sim 60\%$ and $100\text{-}200 \text{ nm}$ for $\sim 30\%$ of the total
329 number concentration (Appendix D), demonstrating the controlling influence of smaller
330 particles. During fog, the median particle number concentration decreased by 40% and 30%
331 for particles in the ranges of $10\text{-}100 \text{ nm}$ and $100\text{-}200 \text{ nm}$, respectively, but did not show
332 significant change for the larger particles. It appears that smaller particles were more

333 susceptible to losses due to Brownian diffusion leading to wet scavenging, as observed in
 334 clouds (Greenfield 1957). Conversely, particles > 200 nm were unaffected by fog, causing an
 335 increase of their relative contribution (Wu et al. 2022).

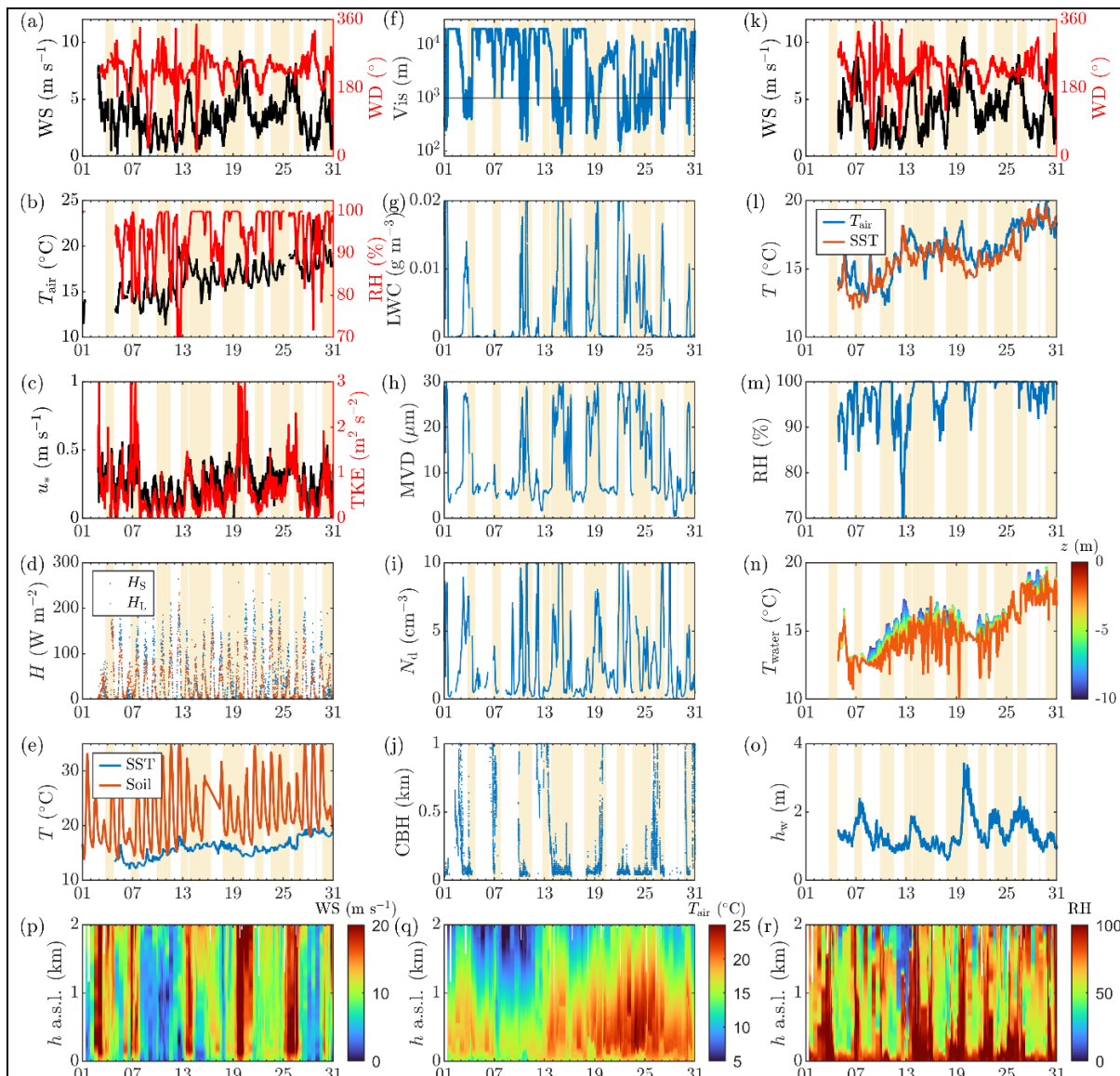


Figure 5: Data from the (a-e) center tower (15 m), (f-j) microphysics station, (k-o) wave glider Carson operating 30-60 km southwest of Sable (Grare et al. 2021), and (p-r) radiosondes (3-4/hour). (a) 2 m wind speed WS and wind direction WD; (b) 2 m air temperature T_{air} and relative humidity RH; (c) 2 m friction velocity u_* and turbulent kinetic energy TKE; (d) 2 m sensible and latent heat fluxes (H_s , H_L); (e) soil temperature T_s and SST; (f) visibility Vis (1 km threshold or fog is identified by a horizontal line); (g) liquid water content LWC; (h) MVD; (i) droplet number density N_d ; (j) cloud base height CBH; (k) WS and WD (k-o, from wave glider Carson); (l) T_{air} and SST; (m) RH; (n) water temperature T_{water} ; (o) significant wave height h_w ; (p) WS (p-r, from rawinsondes); (q) T_{air} ; and (r) RH. a.s.l – above sea level. For instrument details, see Appendix K.

336

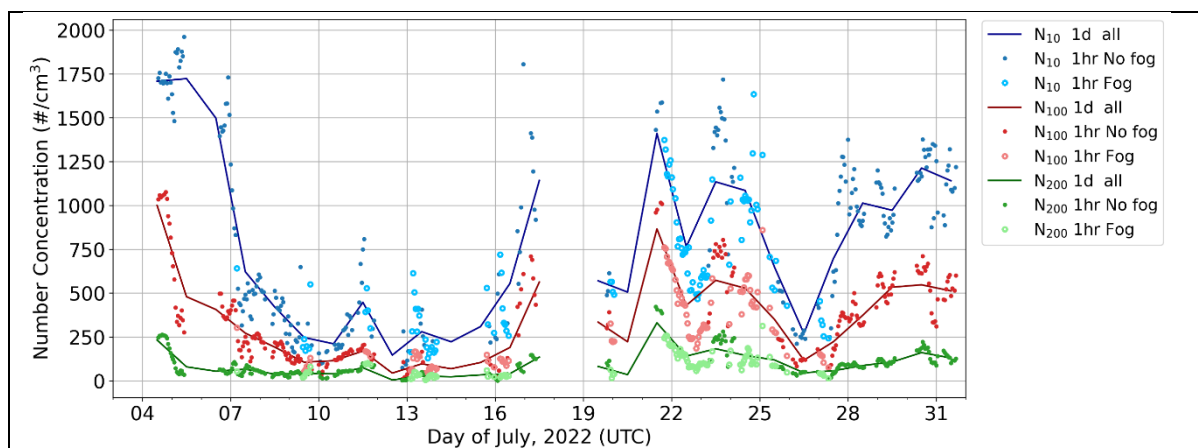


Figure 6(a): Aerosol number concentration from 10.6 to 496 nm measured with the SMPS on the ship bridge (Appendix K). N10 (blue), N100 (red) and N200 (green) indicate the number concentrations of all aerosols with diameter > 10 nm, 100 nm, and 200 nm, respectively. The solid lines represent daily (1d) averages, small dark solid circles are hourly (hr) averages during no fog, and large bright circles are hourly averages during fog. The aerosol inlet sampled dry aerosols at 19 m a.s.l. and travelled through 11.35 m of stainless-steel tubing before being measured by the SMPS. The gap of observations during July 17-19 was due to the port call.

337

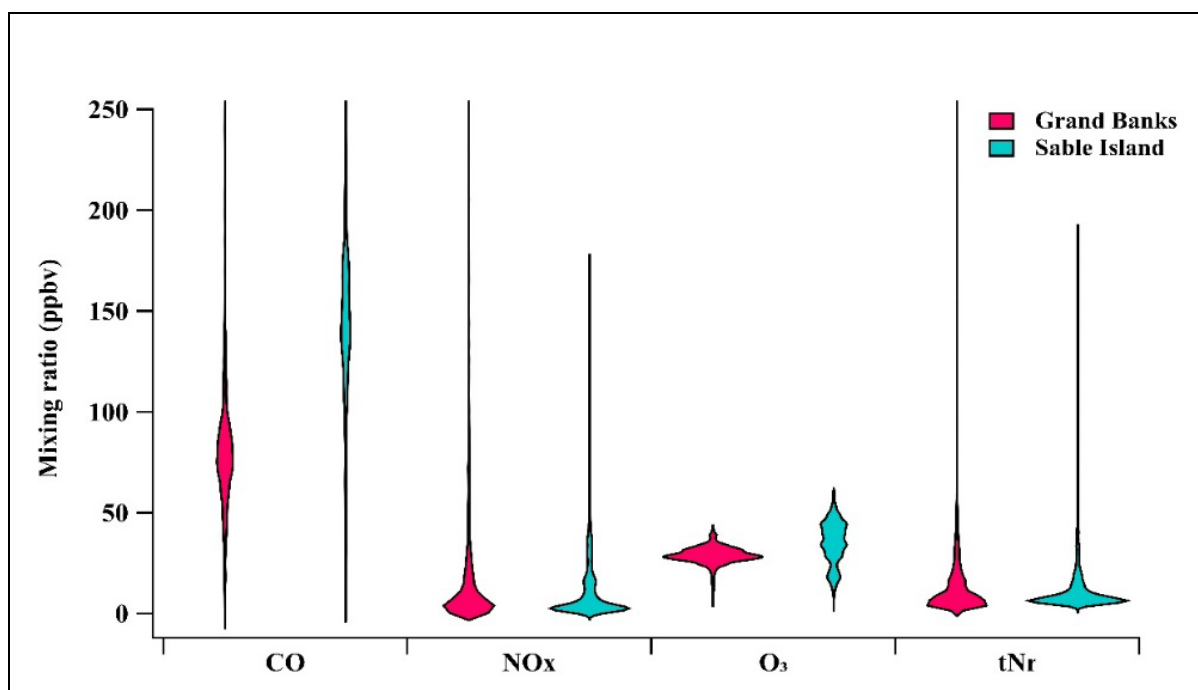


Figure 6(b): A Violin plot of atmospheric pollutant distributions of combustion product mixing ratios that are long-lived like carbon monoxide (CO) or moderately-lived like nitrogen oxides ($\text{NO} + \text{NO}_2 = \text{NO}_x$). NO_x was analyzed via chemiluminescence (Ecotech EC9841), ozone via nondispersive ultraviolet absorption (Ecotech S10) and carbon monoxide CO via infrared absorption spectroscopy (Ecotech EC9830). The instruments were on the ship bridge, and sampled outdoor air from a common sampling manifold passing through the ceiling to the deck above the pilothouse and positioned bow-side (upwind) of the ship exhaust. A custom-built instrument for measuring total gaseous reactive nitrogen (tNr) and its basic fraction (e.g., species like ammonia and amines; NH_3/NR_3) were also sampled from the manifold (Crilly et al. 2023).

338 In matters of gridded gas mixing-ratio observations (Fig. 6b), being further from major
339 anthropogenic emissions regions, the Grand-Banks period is less burdened with the combustion
340 tracer CO compared to the heavily trafficked Sable period (75 ppbv vs 140 ppbv), the latter
341 being closer to the dominant continental outflow of the North American seaboard. Similarly,
342 enhanced O₃ were present in the Sable region (40 ppbv vs 30 ppbv for Grand-Banks).
343 Observations of NO_x and total reactive Nitrogen tN_r were similar in both locations, indicative
344 of NO_x being the primary component of tN_r. Secondary photochemical species (e.g., O₃) are
345 indicative of the pollution regime (Lakra and Avishek 2022), and novel chemical measurements
346 such as tN_r accomplished in Fatima-GB enable the study of particle and droplet composition
347 thermodynamics of fog.

348 **Archetypal Process and Case Studies**

349 ***Synoptic Weather Systems – A Trigger for Fog***

350 Synoptic analyses during Fatima-GB suggest that the [longstanding] hypothesis –
351 northward advection of air masses over Gulf Stream causes them to be warm and humid, which,
352 when passing aloft colder Labrador water creates conditions for escalated summer fog in
353 Atlantic Canada (Appendix A) -- is untenable. The bulk of the July 2022 surface winds at Sable
354 were southwesterly, following the northward advection path, but fog occurred at Sable only
355 30% of the time. Fog genesis mostly required a synoptic trigger, a prospect being eastward
356 propagating deep lows across Eastern Canada. Such systems have broad southward oriented
357 trough that extend across the Atlantic coast and beyond Sable, almost-always accompanied by
358 a broad cloud band with low overcast ceilings (~60 m) and lowered visibility (~1-3 km). After
359 the leading edge passes over Sable, there are occasional fog periods, and a trailing ridge
360 encroaching into the middle and lower layers lowers the cloud top and ultimately terminates
361 fog and clouds.

362 An example is the IOPI, with a cloud band lowering over Sable at 0200 UTC 03 July,
363 and dropping visibility below 4.8 km and ceiling below 915 m. There were two fog periods
364 within this event, one long (1100 UTC 03 July to 0120 UTC 04 July) and the other short (0900
365 to 1145 UTC 04 July). At 1200 UTC 03 July, the driving Low was centered in northeastern
366 Quebec with a deep trough (low) extending along the eastern coast of Quebec, off the
367 Newfoundland eastern coast and southward in the Atlantic to 42°N (Fig. 7a), generating strong
368 southwesterly surface winds over most of Atlantic Canada and a concomitant cyclonic cloud
369 band along the Quebec coast and then extending to the southwest over water (Fig. 7b). This

370 was the first fog period, under a mid-level cloud band. Rawinsondes show that the saturated
371 fog layer included a surface-based air temperature inversion, in the height range of 187-730 m.

372 With time, MSLP trough and cloud band moved eastward. A ridge on the westside of
373 the cloud band began to encroach on the band, lowering the cloud top. A low cloud, fog bank
374 appendage began to extend out from the cloud band, with the second fog forming at 0900 UTC
375 04 July. This is evident in 1200 UTC visual satellite image, extending well out from the sharp,
376 western wall of the band (Fig. 7c). The second fog period had ended 16 minutes before this
377 image. Sable was on the edge of the cloud bank in this image 5 minutes before. Rawinsondes
378 show that the fog layer during this second period was a single isothermal layer 170 m deep
379 capped by a dry air inversion. Thus, the two events differed in structure. While details vary,
380 the broad features of the two events were captured by the WRF-ARW simulations (Appendix
381 E) such as patchiness of fog and dry inversions aloft the potential fog layer. The visibility
382 during 0000 UTC 2 July-0000 UTC 05 July was directly related to the divergence (Fig. 7d).
383 The lowest visibility and fog occurred with the most negative divergence (i.e.,
384 convergence). The maximum visibility occurred with the greatest convergence that triggered
385 surface layer lifting.

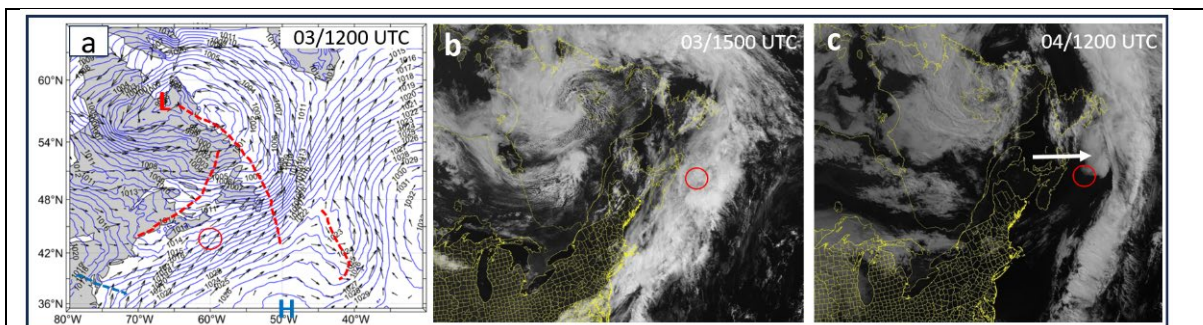


Figure 7: (a) A plot of the GFS Mean Sea Level Pressure (MSLP) at 1200 UTC 03 July 2022. L is a deep low pressure on northeastern Canada which dominates Atlantic Canada with a trough (dashed red line) extending to the south along the coastline past Newfoundland. A second trough (dashed red line) extends to the southwest toward New England coast. The H is the center of a high pressure to the South that dominates the surface layer over water. These features cause strong southwesterly surface winds off Atlantic Canada and over Sable (the center of the red circle). (b) GOES East satellite visual image at 1500 UTC 03 July. A high-topped cloud band extending from the US southwest follows the coastline over water, with Sable in fog, through the Labrador Sea, and cyclonically curls around to the center of the Low in a). (c) Same as (b) but at 1200 UTC 04 July when the cloud band shifted farther east offshore while anticyclonic conditions cleared the sky over Nova Scotia, the surrounding water and over a low cloud/fog bank extending from the main cloud band (white arrow) that contained a second fog period at Sable Island that ended soon afterward with clear sky. Almost all July fog at Sable occurred in the presence of a synoptic scale cloud.

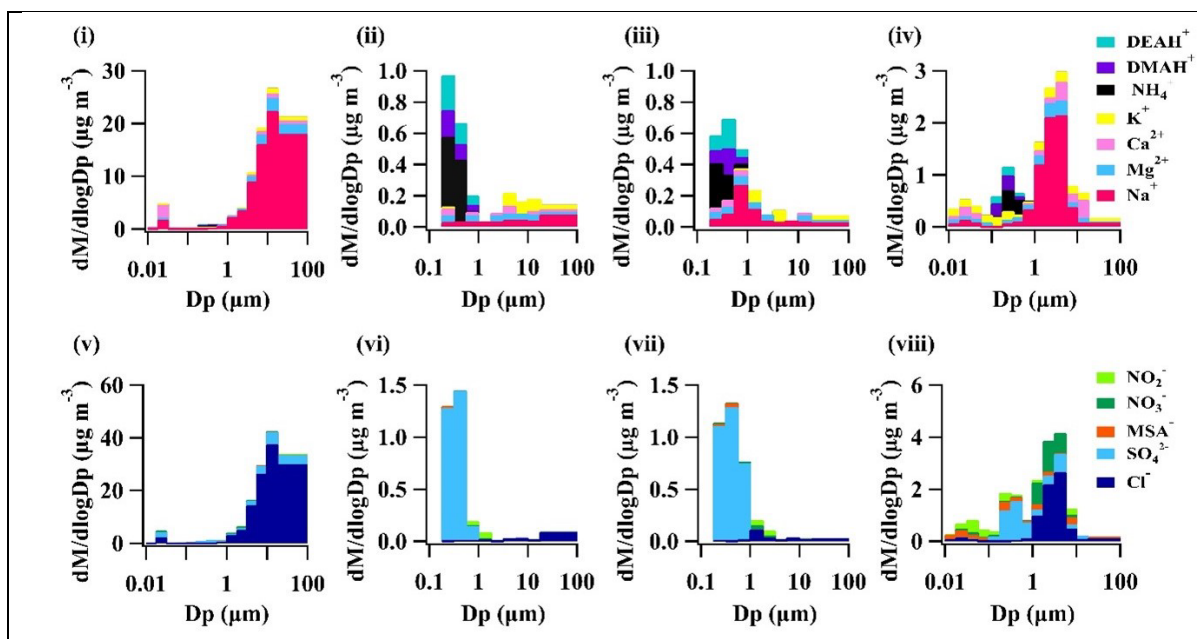


Figure 8: Ion mass loading ($\mu\text{g m}^{-3}$) data samples taken near the Sable Island during IOP9 (19-23 July) by R/V Condor: Ion mass loading of major cations (top row) and anions (bottom row) taken under ambient conditions (pre-fog; i and v, covering 19-21 July), during the fog persistence period sampled during two consecutive intervals (ii and vi during 21-22 July, and iii and vii during 22-23 July), and after the dissipation of fog (iv and viii, 23-24 July) are shown.

A MOUDI and nanoMOUDI II was positioned within a weatherproof enclosure mounted to the railing on the deck above pilothouse (~ 10 m asl) were used. Samples were collected using MOUDI during fog events while nanoMOUDI sampled ambient aerosols, both instruments sampling with a flow rate of 30 L min^{-1} . The MOUDI uses 9 impaction stages to capture particles of aerodynamic diameters from 0.1 to $100 \mu\text{m}$ (Chisholm et al. 2021) whereas nanoMOUDI uses additional 5 impaction stages to collect $0.01 - 0.1 \mu\text{m}$ particles. Fifteen samples during fog events and fourteen ambient samples were collected with durations spanning 197 to 2490 min.

396 During the fog event, the mass loading of sea-salt ions like Na^+ , Mg^{2+} , Cl^- , and sea salt
 397 sulfate (ss-SO_4^{2-}) in the coarse mode ($1-100 \mu\text{m}$) decreased by two orders of magnitude
 398 compared to pre-fog conditions due to scavenging and deposition. Following fog dissipation,
 399 sea salt aerosols returned, but their mass loadings were lower by a factor of ten compared to
 400 the pre-fog period. These findings are consistent with the expected role of sea salt aerosols
 401 acting as effective FCN, given their high hygroscopicity (Zhao et al. 2022; Sasakawa et al.
 402 2003; Jung et al. 2013). In the fine mode ($0.1-1 \mu\text{m}$), the mass loadings of reduced nitrogen
 403 (NH_4^+ , DMAH^+ , and DEAH^+) and processed sulfur (MSA^- and non-sea salt sulfate) increased
 404 during the fog event compared to the boundary periods, suggesting that droplets and
 405 meteorological conditions supporting fog formation potentially facilitate gases and interstitial
 406 aerosol to participate in chemical reactions and gas-to-aqueous partitioning (Ge et al. 2012;
 407 Meng & Seinfeld 1994). The mass loading of interstitial aerosol, therefore, increased during
 408 fog events and persisted afterwards. This confirms the well-known fog scavenging mechanisms
 409 of supermicron sea salt aerosols into droplets beyond $20 \mu\text{m}$ in diameter (Richter et al. 2021;

410 Wagh et al. 2021). The findings are also consistent with marine fog-facilitated gas-particle
411 partitioning recently reported in the Arctic (Kecorius et al. 2023). Upon fog dissipation,
412 supermicron sea-salt aerosols were generated faster than their losses and returned to observable
413 levels.

414 In addition to aerosols $> 0.1 \mu\text{m}$ discussed above, attempts were made to characterize
415 bioaerosols using novel, high-resolution detection technologies. Biological species and organic
416 compounds with sizes from tens of nanometers to $100 \mu\text{m}$ are prevalent in sea spray aerosols
417 (SSA), thus making nascent growth factors (e.g., hygroscopicity and nucleation) for SSA
418 deviate from pure salt particles (Bertram et al. 2018). The roles of bioaerosols as CCN or FCN
419 are poorly characterized at present (Schiffer et al. 2018), but bioaerosols containing ice
420 nucleating proteins are known to act as ice nuclei and possibly FCNs for rapid mixed-phase
421 cloud/ice-fog formation via heterogeneous processes (Knopf et al. 2018; Huang et al. 2021;
422 Crawford et al. 2020, 2023). Two bioaerosol instruments were deployed: CINCS, a novel
423 instrument designed for sizing, and MBS designed for concentration. Imitating the human lung,
424 CINCS ingests biological cells with minimal stress to the organism, thus maintaining their
425 viability and facilitating post-collection analysis using standard techniques. *Pseudomonas*
426 *syringae* (PS), known to be conducive for ice-nucleation, was selected as the target bioaerosol
427 (Soveizi et al. 2023). The second, MBS is a biofluorescence spectrometer that detects and
428 classifies bioaerosols in real-time time via the collection of autofluorescence spectra, size, and
429 morphological parameters on a single particle basis. Following Freitas et al. (2022), MBS data
430 were classified into following representative groups: weakly fluorescent populations (e.g., SSA
431 with organic content), fluorescent sea spray aerosols (FSSA), highly fluorescent sea spray
432 aerosols (HFSSA), primary biological aerosol particles (PBAP) and non-fluorescent aerosols.

433 Initial analysis of CINCS data from 25-30 July suggested an increased presence of PS
434 on 29 and 30 July (IOPs 13/14) as compared to the other days, suggesting microphysical
435 enhancing capability may have had more of a hand in Fatima-GB rain events as much or more
436 so than the onset/presence of fog (Appendix F(i)). The processed MBS data indicate notable
437 PBAP events during 07-08, 28-29 and 30-31 July, and 31 July – 01 Aug, which are consistent
438 with CINCS PS observations (Appendix F(ii)). There are more frequent, and extended HFSSA
439 events throughout the deployment. Interestingly, while HFSSA concentrations are generally
440 greater than PBAP, during the PBAP emission events the PBAP concentration significantly
441 exceeds that of HFSSA. Increase of PBAP during drizzle or rain events is generally evident,
442 while both HFSSA and PBAP are suppressed by fog via nucleation or scavenging/deposition.

443 These observations provide pointers for future multi-instrument interrogations on fog-
444 bioaerosol nexus.

445 *Lifecycle of Fog – Pursuing a Stratus-Cloud-Lowering Event*

446 IOP13 encompassed a stratus-cloud lowering event, a common mechanism of fog
447 formation (Koračin et al. 2001; Fathalli et al. 2022; Singh et al. 2024), as evidenced by synoptic
448 analysis (not shown). Ceilometer backscatter, Doppler Lidar velocity vectors and contours of
449 vertical velocity variance s_w show that preceding the event (2100 UTC, 29 July), the surface
450 winds were southerly with RH ~ 85% while winds aloft were southwesterly/southerly (Fig. 9a).
451 Rawinsondes indicate an unstable surface layer up to ~50 m with an overlying inversion up to
452 ~200 m, topped by a relatively mixed layer up to ~300 m (Fig. 9b). Around 2230 UTC, winds
453 aloft shifted more westerly and a stratus cloud appeared at 600-800 m (Fig. 9a), accompanied
454 by stratus top cooling and temperature inversions beneath (see Singh et al. 2024), as evident
455 from the 2058 UTC sounding (Fig 9b). Ensuing top-down convection (note the s_w contours)
456 concomitant with light precipitation moistened the lowest 600 m (Figs. 9b, Appendix G).
457 Convective turbulent mixing was observed both aloft by the Doppler Lidar (Fig. 9a) and at the
458 surface by sonic anemometers (TKE, Appendix G). The stratus cloud descended approximately
459 600 m in 3.5 hours (starting 0030 UTC), leading to a dense, persistent, ~125 m thick fog layer.
460 With the appearance of stratus, turbulence levels decreased and the winds throughout the
461 lowest km shifted westerly.

462 The fog event was rather homogenous across Sable, based on visibility from the FD70
463 and BLS900 (Appendix G). The significant deviation between the BLS900 and FD70 at 1000
464 UTC was due to the full attenuation of BLS900 signal where lower visibility could not be
465 resolved. The LWC at lower heights during most of the fog event was dominated by larger
466 droplets (10-20 μm) captured by FD70. In combination, FM120 and FD70 data painted a
467 clearer picture of what was occurring, especially near the dissipation of fog just after sunrise
468 (1030 UTC) when the fog layer began to lift (Fig. 9a).

469 During fog dissipation, TLS captured the profiles of T, RH, WS, LWC, and the net
470 longwave radiation LW_{net} (Fig. 9c). Between 1130 and 1200 UTC, when the fog was still
471 relatively dense, the LW_{net} profiles showed relatively strong radiative cooling. As the fog
472 dissipation began, the larger droplets evaporated to augment the smaller-particle population
473 and hence an increased LWC (by FM120) and an abrupt drop of visibility (Appendix G).

474

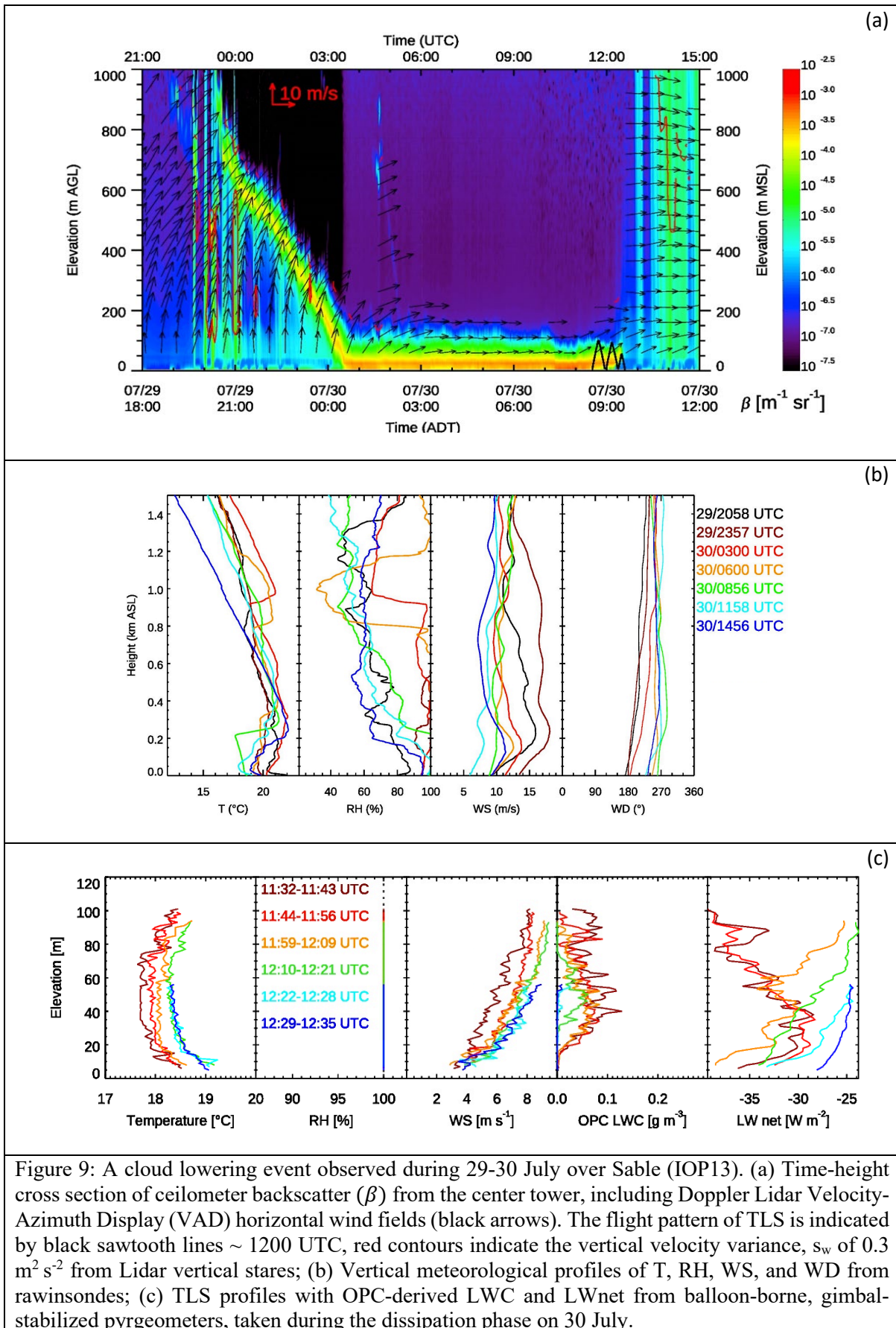


Figure 9: A cloud lowering event observed during 29-30 July over Sable (IOP13). (a) Time-height cross section of ceilometer backscatter (β) from the center tower, including Doppler Lidar Velocity-Azimuth Display (VAD) horizontal wind fields (black arrows). The flight pattern of TLS is indicated by black sawtooth lines ~ 1200 UTC, red contours indicate the vertical velocity variance, s_w of $0.3 \text{ m}^2 \text{ s}^{-2}$ from Lidar vertical stares; (b) Vertical meteorological profiles of T , RH, WS, and WD from rawinsondes; (c) TLS profiles with OPC-derived LWC and LWnet from balloon-borne, gimbal-stabilized pyrgometers, taken during the dissipation phase on 30 July.

476 Concomitant were a LWnet profiles shift (Fig 9c) and tendency toward radiative
 477 heating. By 1200-1300 UTC, incoming SWR further increased, the concentration of larger
 478 droplets disappeared, resulting in a complete evaporation/dissipation of the fog layer.
 479 Interestingly, as a result of being optically thin, the fog layer eroded from the bottom (Fig.
 480 9a,c), permitting sufficient surface heating to trigger an increased sensible heat flux and
 481 radiative heating over Sable.

482 ***A Tale of the Unexpected – Fog Shadow***

483 During 1-km resolution COAMPS® mesoscale model simulations (Appendix H)
 484 conducted during 30 June to 31 July to support IOP forecasts, a clearing in an otherwise
 485 reduced horizontal visibility could be frequently noticed downstream of Sable Island. After 22
 486 July, this phenomenon became conspicuous, and was dubbed *fog shadow*. Eight consecutive
 487 forecasts starting 1200 UTC 22 July consistently predicted, at least in initial runs, this
 488 [unanticipated] phenomenon. For example, in Fig. 10, a large, uniform patch of dense fog
 489 (visibility < 500 m) is visible to the east of Nova Scotia, in a clearing downstream of Sable
 490 Island.

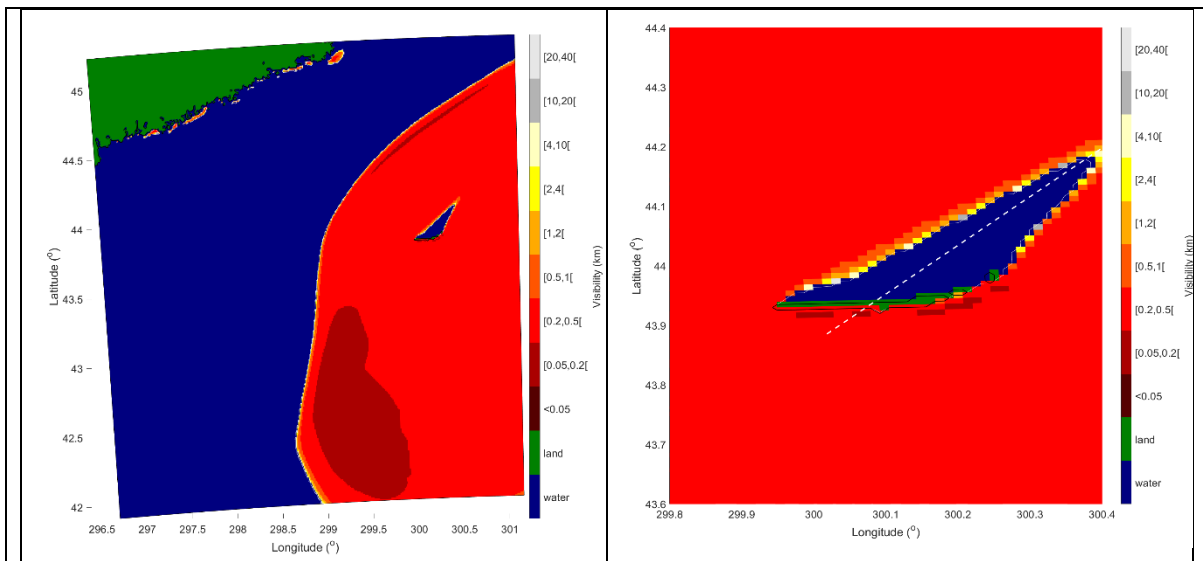


Figure 10: A 27-hour COAMPS® forecast of the horizontal visibility at the lowest thermodynamic level (1.5 m) valid at 15 UTC on 24 July 2022. A full innermost nest with 1 km grid spacing (left panel), and an enlarged area centered over Sable (right panel). Nests are depicted in Appendix H. The dashed white line in the right panel shows the location of the southwest-northeast vertical cross-section used for studies. A black solid line indicates coastline, and a white solid line in the left panel represents the fog (appear in red around the island) boundary. At this resolution in the innermost nested grid, Sable Island is barely resolved and the eastern flank of the island is narrower than the rest of the island. It appears as separate small islands in the model because even at 1 km the grid resolution is too coarse to resolve the actual width.

491 An in-depth analysis of fog shadow, including hindcasts using finer, sub-1-km
 492 horizontal grid spacing will be presented in Gaberšek et al. (2024). The investigator zeal

493 following the observance of fog shadows in simulations led to a super-IOP (IOP10) on the 23
494 July. In addition, fortuitously, R/V-Condor was slated to sail southward on the 22 July to make
495 its final N-S transect south of Sable Island across the Gulf Stream, and an intrepid decision was
496 made to change its course for a coordinated [sub]campaign between SI and R/V-Condor crews
497 to hunt for the fog shadow.

498 During IOP10, the fog shadow was unequivocally observed, mostly in the early
499 afternoon, by instrumentation at Sable Island and in satellite imagery, with its streamwise
500 length close to the predictions (Appendix I). Two mechanisms of fog-shadow genesis were
501 hypothesized, namely: (i) evaporation of fog during (adequate) land surface heating, and (ii)
502 increased turbulence as a result of the development of IBLs at the leading and lee edges of
503 Sable. Extensive observations supported the former (discussed in Bardoel et al. 2024), and thus
504 the fog shadow here appears to have similarities to fog holes over urban areas due to heat island
505 (Gautam & Singh 2018; Theethai et al. 2023).

506 The R/V-Condor arrived northeast of Sable at the wee hours of 26 July to begin
507 IOP11/ISP5 sub-campaign, named “Sable Lee Observing Period (SLOP)” wherein
508 synchronized rawinsonde launches were made, 38 each, from the Sable Island and R/V-
509 Condor. Fig. 11(a-c) provides a measurement summary of SLOP. The data prompted a unique
510 case study of IBLs in the presence of fog and highly localized surface heterogeneity at coastal
511 margins.

512 While the ship was enroute toward Sable, disappointingly, the 24 July forecast made for
513 the 26 July was reversed on 25 July, to a no-fog/shadow day, which was prescient. On the
514 Sable, the visibility was in the ‘mist’ regime until 1000 UTC 26 July and the same with
515 occasional fog patches prevailed at R/V-Condor (Fig 11e). Thereafter, the visibility at both the
516 ship and Sable was high (~ 5-15 km), indicating no fog shadow. Fog appeared on Sable at 2100
517 UTC 26 July but with high visibility on the ship until 0100 27 July UTC, thus suggesting a
518 different fog-shadow genesis mechanism than the land heating mechanism above. The ship and
519 Sable captured horizontal (positive) gradients in visibility downstream of the island, which
520 holds implications for IBL effects on fog shadow, optical propagation, and fog-surface
521 interactions. The synoptic conditions, rather than local thermodynamics (Sable heating),
522 seemingly played a decisive role in fog-shadow suppression on 26 July. More details of SLOP
523 study will be presented in Ortiz-Suslow et al. (2024).

524

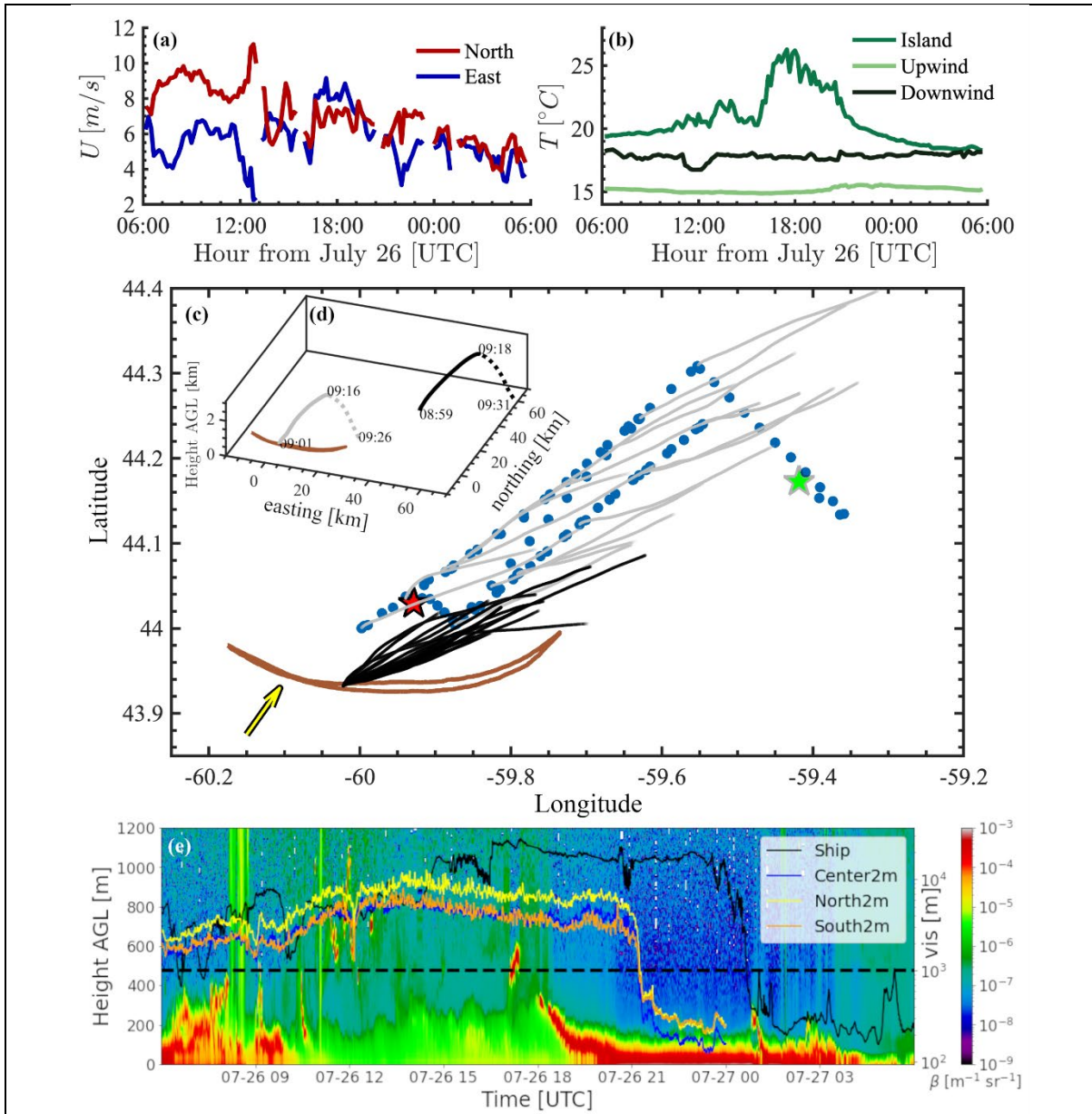
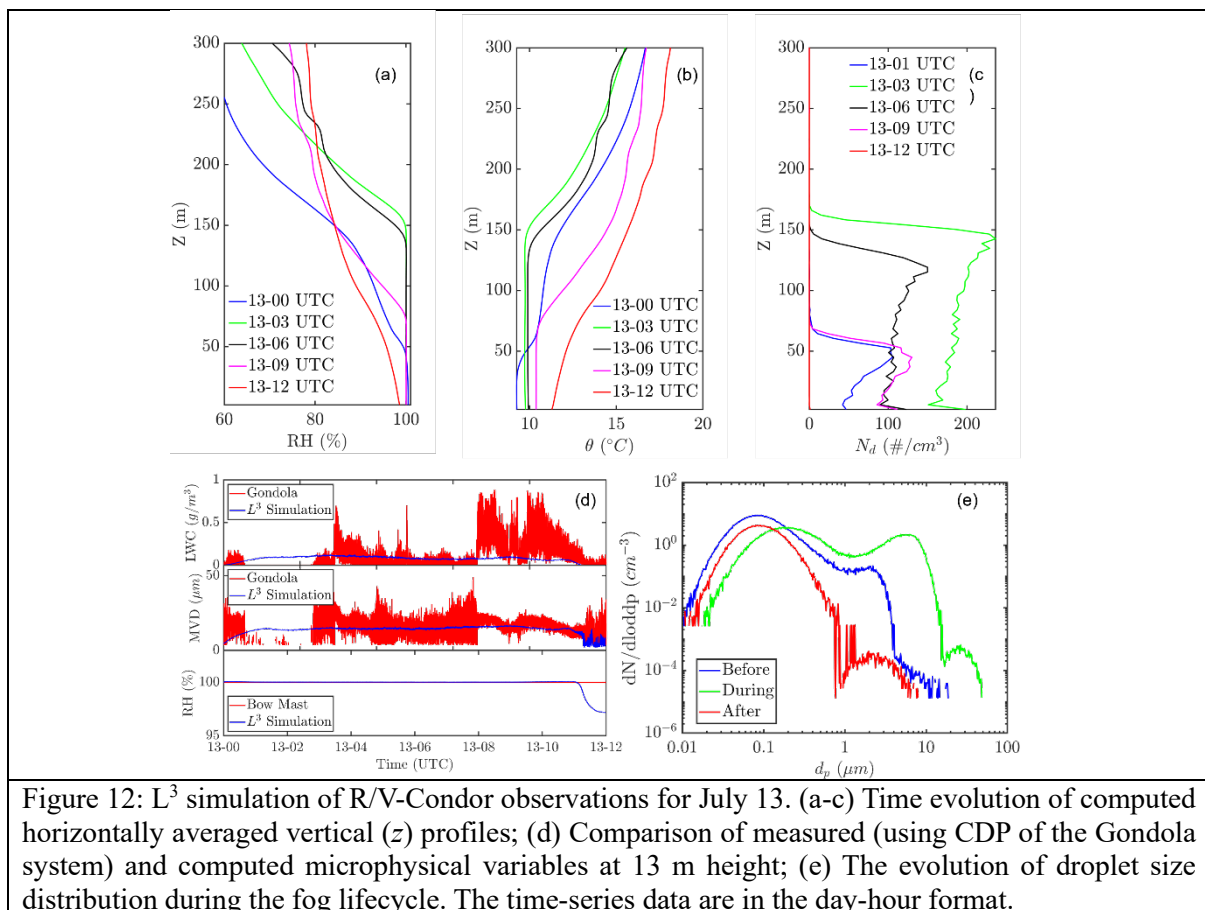


Figure 11: An overview of SLOP case study, 0600 UTC 26 July to 0300 UTC 27 July. (a) From the R/V-Condor bow mast, southwesterly surface winds driven by low level jet that builds through the local morning and then diminishes steadily through the remainder of the IOP was observed; (b) Surface T records from Sable (radiometric skin T, corrected for DWR), a small wave buoy 3 km south of the island (upwind, thermistor on the buoy hull 10 cm from the surface), and R/V-Condor (downwind, radiometric skin T via ROSR); (c) Overview of the sampling downstream of Sable, with R/V-Condor track marked in blue circles. Stars denote the beginning (green) and end (red) positions. The grey/black lines show rawinsonde trajectories from the ship/island, which were deployed in an up-down ABL mode using the controlled leak technique. The black (encircling a white) arrow shows the mean surface wind vector from the ship's bow mast; (d) An example of the coordinated ship (black)-island (gray) up-down rawinsonde launches with distances from West Light station of Sable (brown). (e) Ceilometer backscatter with altitude from R/V-Condor (colormap) overlaid by FD70 visibility at the ship and PWD-22s on Sable towers.

525 **Fog Microphysics via High Resolution Simulations**

526 A Large-Eddy Simulation (LES) combined with large-scale dynamics (LSD) and
 527 Lagrangian Cloud Model (LCM) -- acronymized L^3 coupling -- was used to simulate selected

528 fog events. As an example, simulation for July 13 (ISP1) is discussed below, with model details
529 briefly in Appendix J and in Barve et al. (2024). At the simulation time, R/V-Condor was on
530 the Hibernia Grid (defined later in Fig.13a). The computations were initialized at 2100 UTC
531 on 11 July with initial meteorological conditions derived from ERA5 (Hersbach et al. 2023).
532 The initial aerosol distribution was approximated as bimodal, the sum of two lognormal
533 distributions with $N_d = 800 \text{ cm}^{-3}$. The simulations continued until 1500 UTC on 13 July. As for
534 observations, the 12 July showed shallow, intermittent (<50 m thick) fog, with visibility
535 fluctuating above and below 1 km, whereas on the 13 July fog was continuous. Figs. 12(a-c)
536 show the computed evolution of horizontally averaged RH, potential temperature (θ) and N_d
537 profiles. Computed LWC, mean volume diameter (MVD) and RH vis-à-vis the direct
538 measurements at R/V-Condor for 13 July are shown in Fig 12(d).



539 The simulated fog onset occurs ~ 0100 UTC, defined by $\text{LWC} > 0.01 \text{ g m}^{-3}$ and RH
540 approaching 100%. This is earlier than the recorded observations (0300 UTC).
541 Notwithstanding, the model well replicates the observed fog dissipation time ($\sim 11:00$ UTC).
542 According to Fig. 12a, fog was initially confined near the surface (<50 m), but later the
543 longwave radiative cooling at the fog top led to top-down convection, contributing to the
544 growth and homogeneity of fog layer, which peaked at 150 m thickness. Fig. 12(e) presents the

545 evolution of droplet size distribution, which was bimodal before and after the fog, but a third
546 peak (at $\sim 8 \mu m$) emerged during fog, indicating the activation of the accumulation mode
547 aerosols that are responsible for increased LWC. Overall, the general consistency of field
548 observations and simulations of LWC, MVD and RH trends indicate the promise of L^3 as a
549 simulation tool.

550 *Nexus of Continental Shelf Turbulence and Fog*

551 Guided by the hypothesis that enhanced turbulence over shelf or shelf break favors fog
552 formation due to intensified air-sea interactions and lateral mixing (see Appendix A), and since
553 limited measurements during 2018 C-FOG field campaign to the south of Nova Scotia could
554 not fully verify this hypothesis (Lozovatsky et al. 2021), further measurements were conducted
555 in the Hibernia region of Newfoundland shelf and across the NS shelf not far from the Sable
556 and toward the Gulf Stream cold wall. Up-rising VMP-250 was used for hydro-physical and
557 turbulence measurements at 68 stations (Fig. 13a). The data analysis on the Hibernia Grid
558 reported here consisted of shelf and shelf break stations.

559 Characteristic station averaged profiles of temperature $T(z)$, salinity $S(z)$, and
560 buoyancy frequency $N^2(z)$ and the profiles of TKE dissipation rate ε and eddy diffusivity
561 estimated using $K_N = 0.2 \varepsilon / N^2$ (Lozovatsky et al. 2021) are shown in Fig. 13b. The near-
562 surface turbulence on the shelf break ($\varepsilon \approx 10^{-5} \text{ m}^2 \text{ s}^{-3}$, $K_N \approx 10^{-1} \text{ m}^2 \text{ s}^{-1}$) was weaker compared
563 to that on the shelf ($10^{-4} \text{ m}^2 \text{ s}^{-3}$, $1 \text{ m}^2 \text{ s}^{-1}$). The cumulative distribution functions of the diffusivity
564 $\text{CDF}(K_N)$ calculated using data sets of 8 shelf (over the depth range $-65 < z < -30 \text{ m}$) and 5
565 shelf break ($-90 < z < -30 \text{ m}$) stations, with depth ranges encompassing the thermocline, could
566 be approximated by the generalized extreme value distributions, as was for the NS shelf
567 (Lozovatsky et al. 2021), but parameters of the distributions were drastically different (not
568 shown). The median diffusivity for the Hibernia shelf was $4.1 \times 10^{-6} \text{ m}^2 \text{ s}^{-1}$, only slightly below
569 the shelf-break diffusivity $5.3 \times 10^{-6} \text{ m}^2 \text{ s}^{-1}$, and both were much lower than diffusivities at the
570 Nova Scotia shelf ($3 \times 10^{-5} \text{ m}^2 \text{ s}^{-1}$) and shelf break ($5.8 \times 10^{-5} \text{ m}^2 \text{ s}^{-1}$) during C-FOG. RV-Condor
571 encountered fog recurrently within the Hibernia grid (see ISP1 and ISP2), but a definite
572 association of fog prevalence and surface or thermocline turbulence awaits further data
573 analysis.

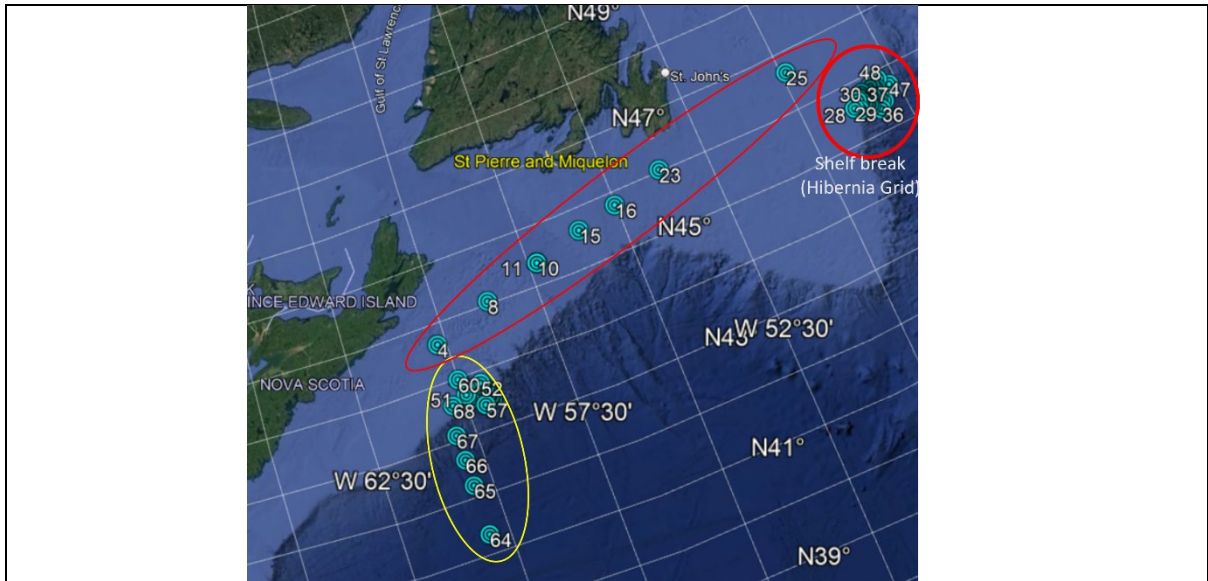


Figure 13(a): Locations of VMP-250 stations covered by R/V-Condor. Stations 4-48 were covered during 8-16 July, with Stations 4-25 (lighter red ellipse) on the shelf, and 26-48 (dubbed Hibernia Grid; dark red circle) on both the shelf and shelf break. R/V-Condor entered Hibernia Grid on ~ 09 July 0600 UTC and left 16 July 1900 UTC. July 21-31 covered stations 50-68 (yellow ellipse) in the Sable area. Within the Hibernia Grid, shelf stations (26, 27, 29-31, 40, 41, and 44) and shelf break (28, 32, 39, 45 and 48) were separately analyzed. Some station numbers are not legible because of overlap.

574

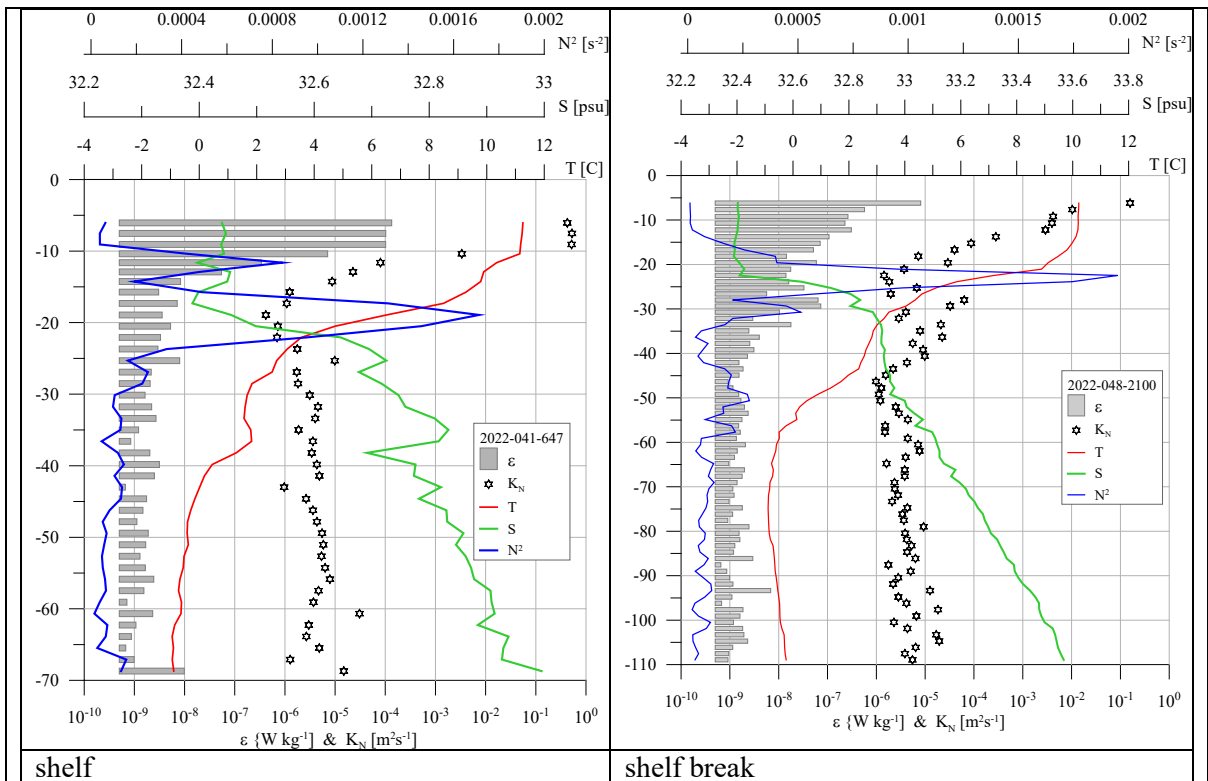


Figure 13b: Stratification profiles T , S , N^2 and turbulent variables ε and K_N at the Hibernia grid (for details see Figure 13(a)). The vertical axis is the depth (in m) below the mean sea surface located at $z = 0$. The T , S , and depth (z) are from the VMP-250, and ε was evaluated using shear profiles. K_N was calculated using the standard techniques (Lozovatsky et al. 2021).

575

576 **Exploring Frontier Technologies**

577 The following are examples of novel measurement technologies attempted during
578 Fatima-GB: (i) Simultaneous vertical profiling of microphysics and turbulence above the sea
579 surface using C-CAMS (Fig. 2), and (ii) the Super Combo (Fig. 3h,i) for the measurement of
580 TKE (at K scale) and temperature fluctuations dissipation (O-C scale).

581 ***C-CAMS***

582 A major design challenge of C-CAMS was to obtain a motion-stable platform to safely
583 mount research-grade sensor payloads of larger size, weight, and power supply tethered to a
584 crane wire to allow sampling at different heights above the sea level at a distance uninfluenced
585 by the ship hull. The solution was a reinforced fiberglass pallet container mounted with a
586 horizontal 10-ft tower section to overhang meteorological instrumentation above the ocean
587 surface. The instrument suite characterized the near-surface visibility, meteorology,
588 thermodynamics, turbulence and microphysics. C-CAMS measurements on 14 July 2022
589 (Super IOP5) are shown in Fig. 14, highlighting its capability of sampling a range of variables.
590 Also overlaid are the data from D-CAMS (deck-mounted version of C-CAMS) and from the
591 ship bow mast to extend the vertical data coverage.

592 The visibility measurements show that fog extended above the level of D-CAMS. In
593 fog, C-CAMS visibility increased toward the surface. Of interest are a stably stratified surface
594 layer ($\bar{\theta}$ profile) accompanied by an increase of water vapor with height in both clear and foggy
595 conditions. Since the clear condition is at near saturation (RH = 95-98%), significant increases
596 of T with height resulted in an ‘anomalous’ vertical gradient in the mixing ratio r under stable
597 clear condition, and the increase of r with height is consistent with observed negative latent
598 heat fluxes. In the fog case, the near-surface upward water vapor fluxes are at odds with
599 previous measurements, which call for further study by invoking the role of stable-
600 stratification. Large negative sensible heat fluxes were identified in both conditions, consistent
601 with the stable T gradient near the surface. Significant vertical gradients are evident for all
602 three fluxes, particularly for the momentum flux, in both fog and clear conditions, a clear
603 violation of the constant flux surface layer assumption. Further details on C-CAMS will be
604 presented in Yamaguchi et al. (2025).

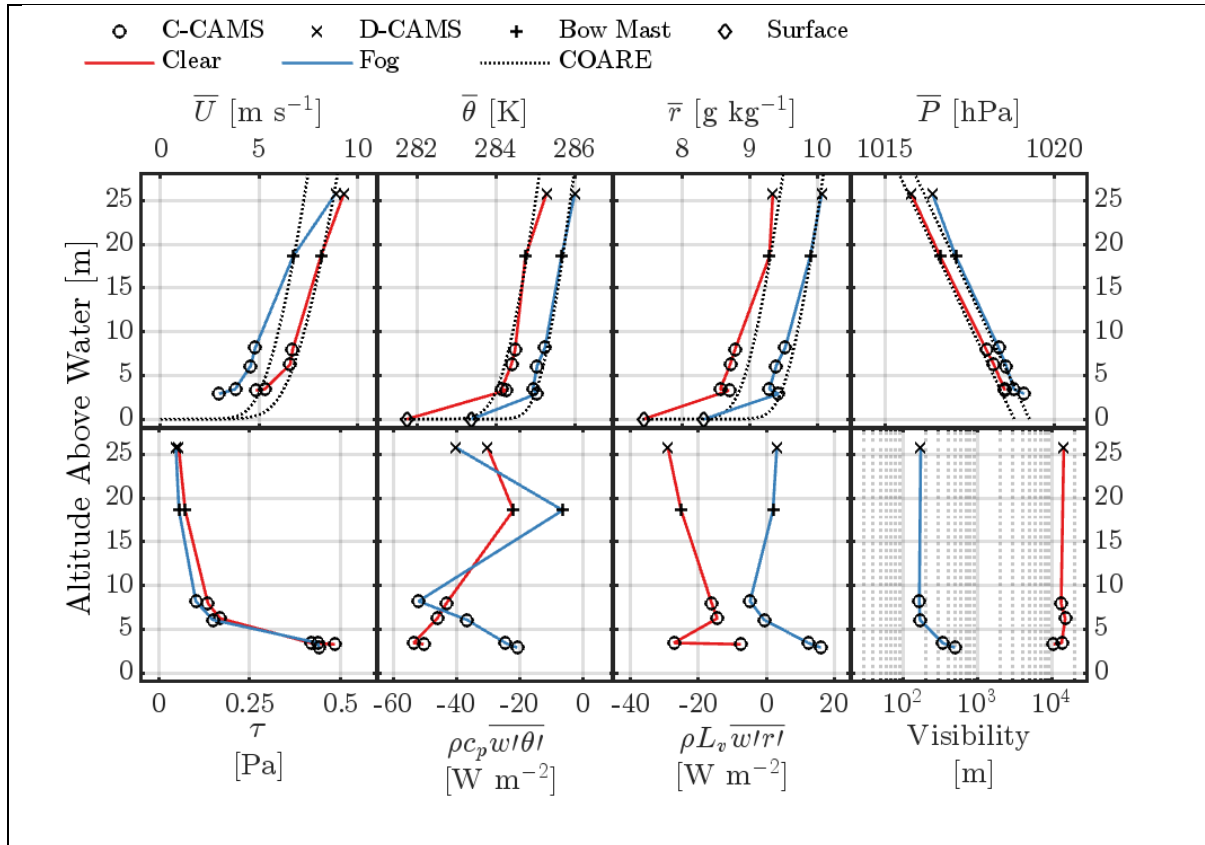


Figure 14: C-CAMS measured vertical profiles of bulk meteorological parameters (mean values of wind speed \bar{U} , potential temperature $\bar{\theta}$, water vapor mixing ratio \bar{r} , pressure \bar{P} , momentum flux τ , sensible heat flux $\rho c_p \overline{w'\theta'}$, latent heat flux $\rho L_v \overline{w'r'}$ and visibility (For C-CAMS details, see Fig. 2, et seq.). The figure shows measurements (circles) on 14 July 2022 during clear (red) and foggy (blue) conditions at 16:02 UTC and 19:50 UTC, respectively, during the nominal 1-hour deployment periods. The bow-mast (+) and D-CAMS (x) data are added to extend the altitude to 18.6 m and 25.4 m above the water level, respectively. The bow-mast and D-CAMS data are time-averaged over the entire C-CAMS sampling period, while each C-CAMS datapoint represents 10 mins averaging during stable and level sampling at three discrete heights. As well, the SST and derived sea surface mixing ratio are shown in the $\bar{\theta}$ and \bar{r} profiles. The bow-mast and shipboard ROSR data were used as inputs to the COARE 3.0 algorithm (Fairall et al. 2003) to obtain canonical mean profiles shown with dotted lines in the top row.

605 ***Super Combo – A Probe System for Penetrating Dissipation Scales of MABL Turbulence***

606 The ‘Super Combo’ (Figs. 3h,i) is an assemblage of high-resolution probes for
 607 simultaneous direct measurement of dissipating (K and O-C) microscales, with additional
 608 information retrievable on LWC, MVD and N_d . The probe system was on a gimbled platform,
 609 controlled by a neural network to align the probes in the wind direction, a requirement for hot-
 610 wire probe operation (Kit et al. 2017). All hot-wires were operated in constant temperature
 611 anemometry (CTA) mode. The technique developed by Goldschmidt & Householder (1969)
 612 for wind tunnels was adopted that converts voltage fluctuations needed by CTA to maintain its
 613 temperature upon impaction of droplets into droplet parameters.

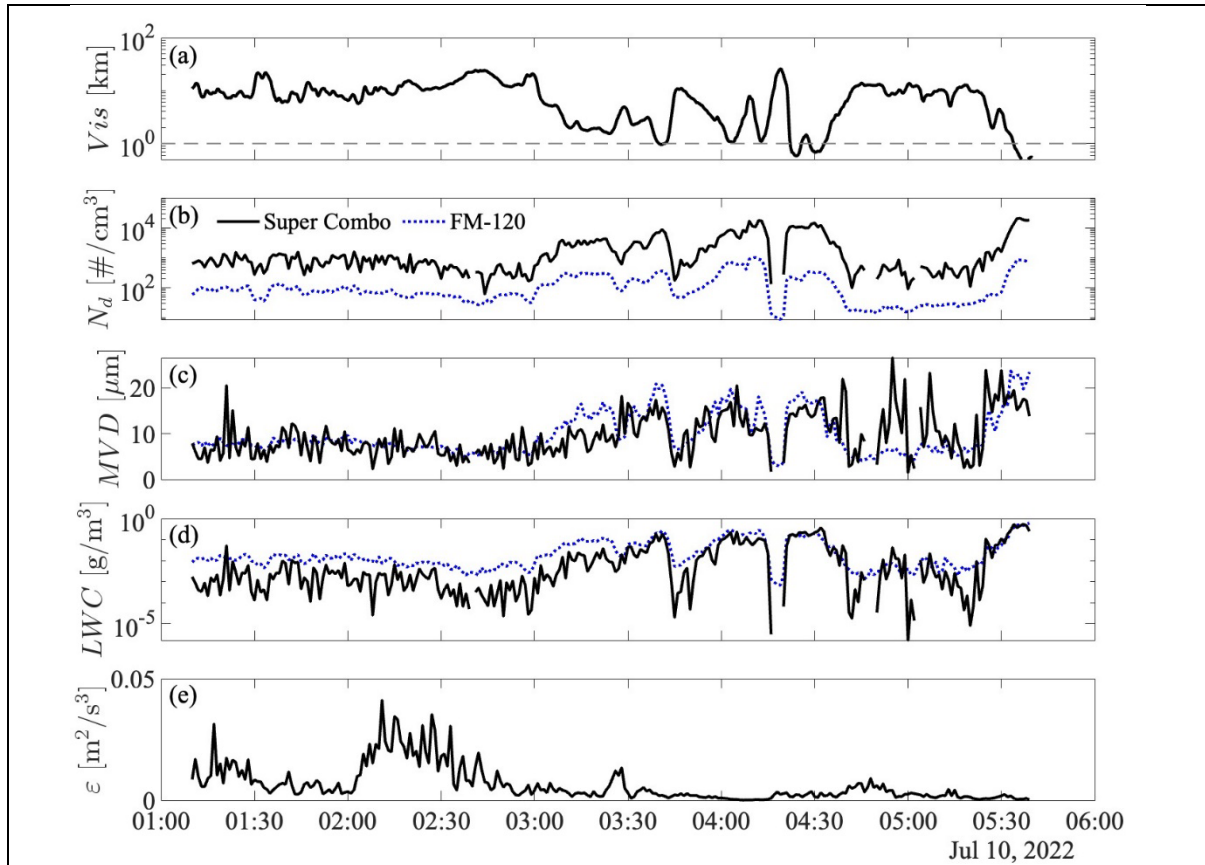


Figure 15: The Super Combo system uses a sonic anemometer to measure larger-scales and a fine-wire probe assembly on a platform that rotates to align with the flow direction to measure the turbulence. The probe assortment consists of high-resolution sensors – two X-wires (TSI 1241-20-film), one parallel array probe (Dantec 55P71-film), and two nano-scale cold-wires (T-NSTAPs) – all collocated with a sonic (RM Young 81000). Shown in the figure are the Visibility (Vis) from FD70 (a) and representative time-series measurements from the Super-Combo system taken on 10 July (IOP3). Gray dashed line in (a) represents the threshold visibility 1 km. For comparison, data from FM120 are included in (b, c, d) with dotted lines. Super combo can resolve droplets ($\sim 1 \mu m$) smaller than that by FM120 ($\sim 2-5 \mu m$), and hence the measurement disparity. As expected, low Vis corresponds to higher N_d and lower levels of turbulence.

614 Fig. 15 shows a representative dataset of one-minute averaged visibility (teetering at
 615 the fog threshold), directly-measured TKE dissipation rate ϵ and microphysical parameters.
 616 Compared with conventional instruments, FM120 in particular, the Super Combo is able to
 617 capture trends of microphysical parameters at a higher space-time resolution. Measured MVD
 618 and LWC are on comparable scales with FM120. The Super Combo gives N_d approximately
 619 one order of magnitude higher than that by the FM120, likely due to its higher sensitivity to
 620 small droplet sizes. Further details will be presented in Huang et al. (2024).

621 Summary and Challenges

622 Prediction of marine fog is one of the most challenging endeavors in meteorology, due
 623 mainly to strong (bio)physicochemical interactions spanning 15-decades of space-time scales
 624 that underlie its lifecycle. Paucity of knowledge, lack of adequate relevant high-fidelity data

625 due to measurement difficulties across synoptic to submicron scales in logistically challenging
626 environments, and non-stationarity and inhomogeneity of marine fog have stymied the progress
627 in fog research, notwithstanding important applications of fog forecasting in transportation,
628 agriculture, industrial and defense sectors. Fatima-GB was a comprehensive multidisciplinary
629 field campaign augmented by NWP modeling and high-resolution (research-grade) simulations
630 to study fog in shallower, non-coastal waters -- categorized as Sea Fog. The study mainly
631 covered the Grand Banks area on North Atlantic shelf, one of the foggiest places on Earth in
632 the summer. Access to an isolated islet (Sable Island) south of Grand Banks, located in the
633 advection pathway of warm Gulf-Stream air toward colder Grand-Banks water conditioned by
634 Labrador current, helped study both sea fog lifecycle and fog-turbulence-land interactions. A
635 ship (R/V-Condor) and the Sable Island were densely instrumented with an unprecedented array
636 of sensors that collected extensive set of data. Some novel sensors/sensor-systems were among
637 those deployed. Data analysis showed that the long-held hypothesis that advection of warm air
638 over colder water causes marine fog was oversimplistic, and a synoptic trigger (e.g., moving
639 high-low systems) is needed for fog genesis. Upper-ocean turbulence measurements cast
640 another hypothesis into doubt, that [intense] shelf-break turbulence may favor air-sea
641 interactions and Sea Fog. Study of cloud lowering events shaped by low-level
642 convergence/divergence illustrated the importance of finer details of meteorological and
643 turbulence structure, highlighting the role of sub-grid microphysical processes of NWP in
644 predicting Sea Fog. First ever long/short wave radiation balance measurements at the fog top
645 using an instrumented tethered balloon system opened up new avenues for future
646 numerical/theoretical studies on fog-top convection and its interaction with surface turbulence
647 during fog evolution. FCNs are imperative for fog, and chemical analyses illustrated that 1-100
648 micron sized coarse (hygroscopic) Sea Salt Aerosols facilitated Sea Fog but were removed by
649 scavenging during fog evolution, leaving behind compounds that might have formed due to
650 chemical reactions between gases and interstitial aerosols. Novel bioaerosol sensors
651 adumbrated some association between hydrometeors and bioaerosols, and broached future
652 opportunities for delineating the role of (~ 10 nm scale) bioaerosols as FCNs, a topic that has
653 invited debate. Overall, accounting for such biochemophysical processes in microphysical
654 schemes of NWP models will be a captivating research topic for the future. Prompted by
655 NWP modeling, a coordinated sub-campaign between the groups at Sable Island and R/V-
656 Condor uncovered the "Fog Shadow" phenomenon - a clearing in the wake of an island in an
657 otherwise foggy area. The existence of a tens of km sized fog shadow behind the ~ 1 km long
658 Sable Island was confirmed for some days. Fog shadow was a result of differential surface

659 heating between the island and surrounding ocean, but was sensitively modulated by synoptic
660 conditions and internal boundary layers. While COAMPS® modeling was the first to elicit fog
661 shadow, the onset and disappearance times of fog shadow in model had disparities with
662 observations, which is a topic for future research.

663 **Acknowledgments**

664 Fatima-GB was an ambitious ‘big-science’ project that was only possible through
665 international scientific cooperation, involvement of a bevy of diverse, skilled and dedicated
666 personnel, munificent support of many organizations, and a special multidisciplinary funding
667 mechanism. Daniel Gibson, Rodrigo Menafrá, Gregory Siddall and Scott Simone of Canadian
668 National Network of Centers of Excellence (MEOPAR) shepherded the utilization as well as
669 conversion of deep-sea supply vessel Atlantic Condor to a research vessel. ONR Naval Vessels
670 Program Manager Rob Sparrock facilitated renting of the vessel. The support and beneficence
671 of Jason Surette (Operations Manager) and his colleagues (Mathieu D’Astous, Greg Stoud and
672 Sarah Medill) at the Sable Island National Park Reserve were vital for the Sable Island
673 campaign. The Sable Science Lead Cornelia (Nell) den Heyer of the Bedford Institute of
674 Oceanography for Fisheries and Oceans, Canada helped gaining access to electricity and
675 accommodation resources at the island. Brilliant logistician Marvin Willis carried a heavy load,
676 from renting a hangar at the Halifax Airport as the operations center to arranging charter flights,
677 helicopters and sea-lift/barges (from Sable Air and Air Borealis, Vision Air and Dominion
678 Diving, respectively) to timely replenishing of food supplies and hardware at the Sable Island
679 and R/V-Condor. He was joined by Paul LeBlanc, who resided partly at Sable Island, to ensure
680 smooth operations. Shawn Quinn of Compliance in Motion Inc. (CiM) was relegated with safety
681 and compliance of transported items. Reno Sit of ECCC led instrumented UAV operations, and
682 Alexis Trottier-Pacquet, Evan Newman Lauren Robinson, Phillippe Gauvin-Bourdon, Baban
683 Nagare and Minghong Zhang were part of the Fatima support group. This work was funded by
684 the Grant N00014-21-1-2296 of the Office of Naval Research (see Appendix A). Additional
685 support was provided by the Wayne and Diana Murdy Fund at UND and the administrations
686 of UND and UU. Finally, our sincere appreciation to ONR Program Managers Dan Eleuterio
687 (who also contributed to this manuscript), Josh Cossuth and Kate Mulreany for their crucial
688 assistance in numerous ways.

689 Sadly, one of the Fatima team members, Professor Iossif Lozovatsky, who prepared
690 Fig. 13, passed away unexpectedly on 23 December 2023. We dedicate this paper to his
691 memory and celebrate his contributions to Physical Oceanography over the past four decades.

692 **Availability Statement**

693 The data used herein have been collected by four research groups (UND/ PSL-NOAA, NPS,
694 UU, Scripps/UCSD) consisting of PIs as well as five collaborating groups (DU, YorkU, AFIT,
695 UMAN, OntTechU); see Appendix A for acronyms. All data are available in a single shared
696 google drive at UND with metadata. A backup drive is also maintained. After an embargo
697 period for the PIs to conduct research, all data will be able to scientific community after 01
698 August 2025, unrestricted. This data base includes raw, intermediate and QC/QA data,
699 COAMPS® and WRF hourly outputs (plots), satellite data and daily weather forecasts from
700 multiple sources.

701 **Appendices**

702 **Appendix A: General Project Information and Summary Hypotheses**

703 The Fatima project seeks leaps in the fundamental understanding of Sea Fog (SF) via
704 multidisciplinary research. It was funded under a Multidisciplinary University Research
705 Initiative (MURI) of the Marine Meteorology and Space Weather Program of the Office of
706 Naval Research (2021-2026). The *Objectives* are to understand and quantify processes
707 underlying the lifecycle of SF, and represent them in NWP models via: (i) deploying leading-
708 edge instrumentation, including novel measurement technologies, to probe from synoptic to
709 smallest scales of ABL turbulence (i.e., K and O-C scales $\sim 1\text{mm}$) and aerosols ($\sim 10\text{-}100\text{ nm}$);
710 (ii) theoretical/numerical analyses of two-phase turbulence; (iii) delving into droplet/aerosol
711 microphysics and dynamics, thermodynamics, surface processes and forcing; (iv) developing
712 microphysical parameterizations for improved visibility predictions using NWPs; and (iv)
713 studying impacts of fog on electro-optical propagation. Seven guiding hypotheses were used:
714 (1) Warmer humid airflow along negative SST gradients, in collusion with sea-surface cooling
715 by air-sea fluxes, provide favorable conditions for SF. Air-sea interactions is abetted by
716 enhanced upper oceanic turbulence (e.g., shelf/shelf-break mixing). Synoptic forcing on ABL
717 is also a key factor;
718 (2) Unlike for low-level (e.g., stratocumulus) clouds, sea-surface processes control fog
719 lifecycle through air-sea fluxes and ABL dynamics (in particular, wave boundary layer,
720 LW/SW radiation and shear). FCNs are significantly contributed by sea surface aerosols (SSA)
721 produced by wave breaking;
722 (3) Precipitation from clouds above the fog layer has profound impacts on SF lifecycle by
723 moistening the sub-cloud layer, scavenging fog droplets, suppressing SSA production and
724 modifying surface waves and turbulent fluxes;

725 (4) While synoptic to microscales strongly affect SF genesis, a critical (rate determining) step
726 is outer (integral) scale eddies feeding TKE to K scales via Kolmogorov (nonlinear) energy
727 cascade down the inertial subrange. It is within K eddies that temperature/moisture
728 homogenizes and spawns fog droplets around embedded FCNs by vapor deposition under
729 specific conditions;

730 (5) Radiative cooling and heating are crucial for the lifecycle of SF through their link to
731 microphysical and turbulence processes.

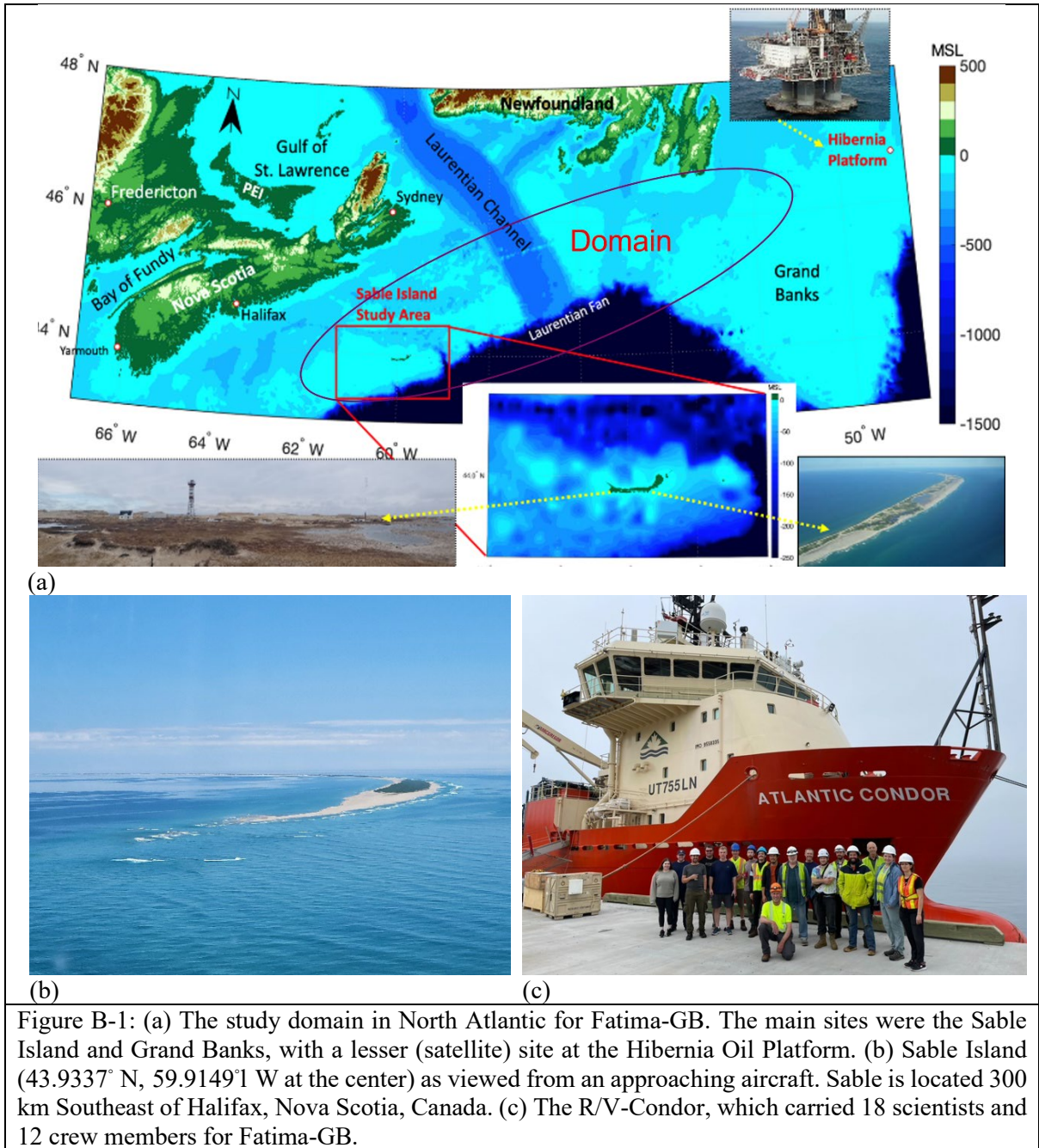
732 (6) Optical attenuation in fog can be parameterized using fog-integrated microphysical and
733 turbulence parameters.

734 (7) A two-wavelength microwave MW and near infra-red NIR scintillometer can be used to
735 infer microphysical properties of fog, forms of precipitation, and evolutionary stages of fog.

736 Fatima enlists a multidisciplinary team of researchers for melding theory, simulations,
737 field observations, technological developments and NWP modeling. It is led by five
738 Universities: University of Notre Dame (UND), Naval Postgraduate School (NPS), Scripps
739 Institute of Oceanography, University of California, San Diego (Scripps/UCSD), University of
740 Utah (UU), and University of Minnesota (UM). Collaborating institutions from the US are the
741 Airforce Institute of Technology (AFIT), Argonne National Laboratory (ANL), Army
742 Research Laboratory (ARL), Pacific Northwest National Laboratory (PNNL) and the Physical
743 Sciences Laboratory at NOAA (PSL-NOAA). The international participants are: Bedford
744 Institute of Oceanography (BIO), Canada; Dalhousie University (DU), Canada; Digital
745 Environment, WSP, Canada (WSP); Korea Institute of Ocean Science and Technology
746 (KIOST), Republic of Korea ROK; University of Manchester (UMAN), UK; Ontario Technical
747 University (OntTechU), Canada; Yonsei University (YU), ROK; and York University
748 (YorkU), Canada.

749 **Appendix B: Grand Banks and Sable Island – Domain Covered by R/V**

750 A backdrop of Fatima-GB campaign with ocean and land domains covered is shown in
751 Fig. B-1, including measurement platforms.



752

753

754 **Appendix C: Instrument Layout at Sable Island**

755 An extensive array of instruments at Sable was packed into two clusters, as shown in Fig. C1.

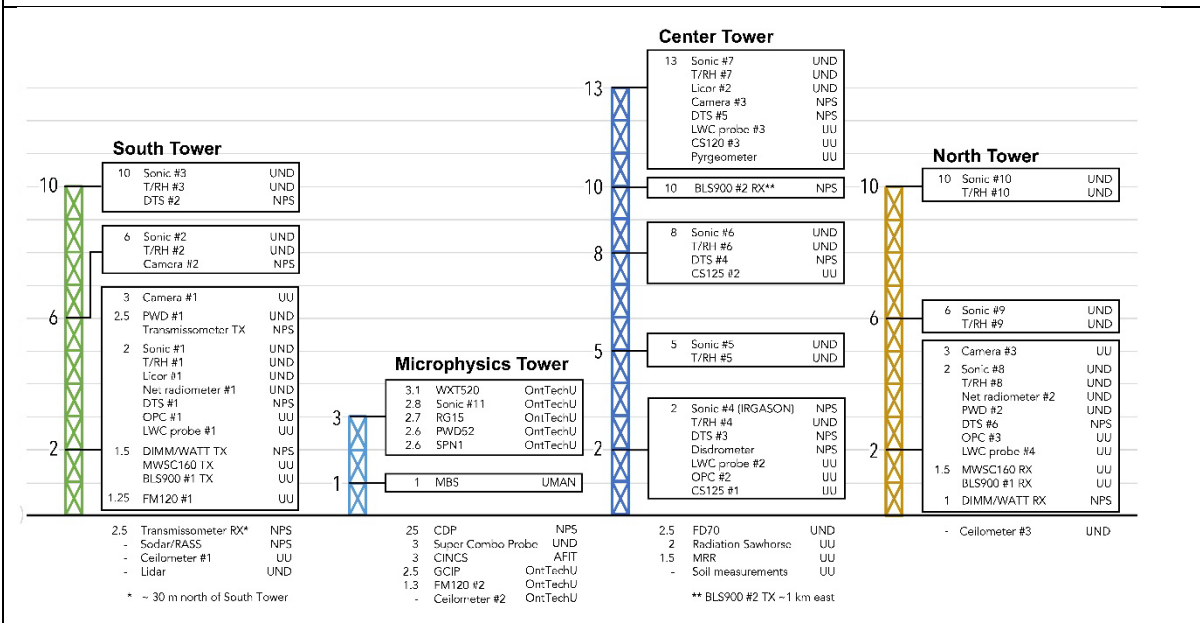
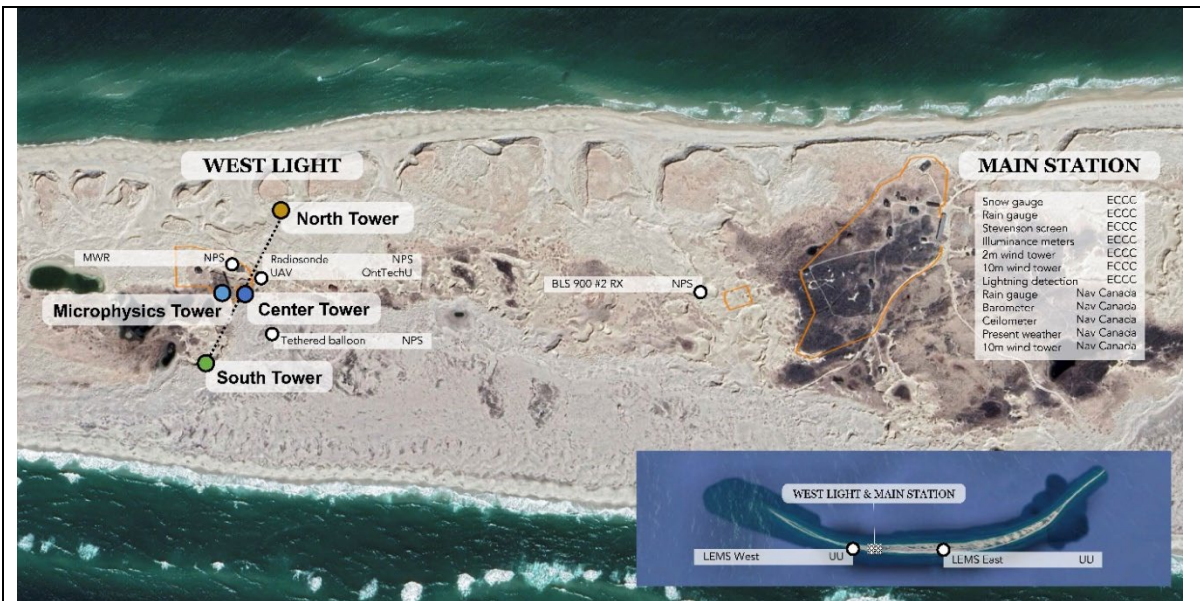


Figure C-1: Top: Two principal campaign locations – West Light and Main Station. Backbone of towers in West Light (South, Center, Microphysical, and North) around which instrumentation is clustered. Default Parks-Canada instruments in Main Station from (Environment and Climate Change Canada, ECCC) and Nav Canada. Inset: LEMS locations, with the shaded rectangle denoting the zoomed-in area. Below: Instruments on each tower and their location, with surrounding instruments in each cluster. All heights (numbers) are in m and instrumentation are described in text and Appendix K.

756

757

758 **Appendix D: Hourly Aerosol Concentration Statistics**

759 The 25th percentile (p25), 50th percentile (p50), 75th percentile (p75), mean, and
 760 standard deviation (std) of hourly aerosol concentrations for aerosols with diameter larger than
 761 10, 100 and 200 nm during fog and no fog at R/V-Condor are presented in Table D1.

762 **Table D1:** Statistical data on hourly aerosol concentration

763

#/cm ⁻³	N 10		N 100		N 200	
	fog	nofog	fog	nofog	fog	nofog
p25	329	358	125	152	33	44
p50	565	828	251	317	85	74
p75	904	1229	448	517	129	115
mean	630	831	300	361	91	94
std	349	517	207	255	66	75

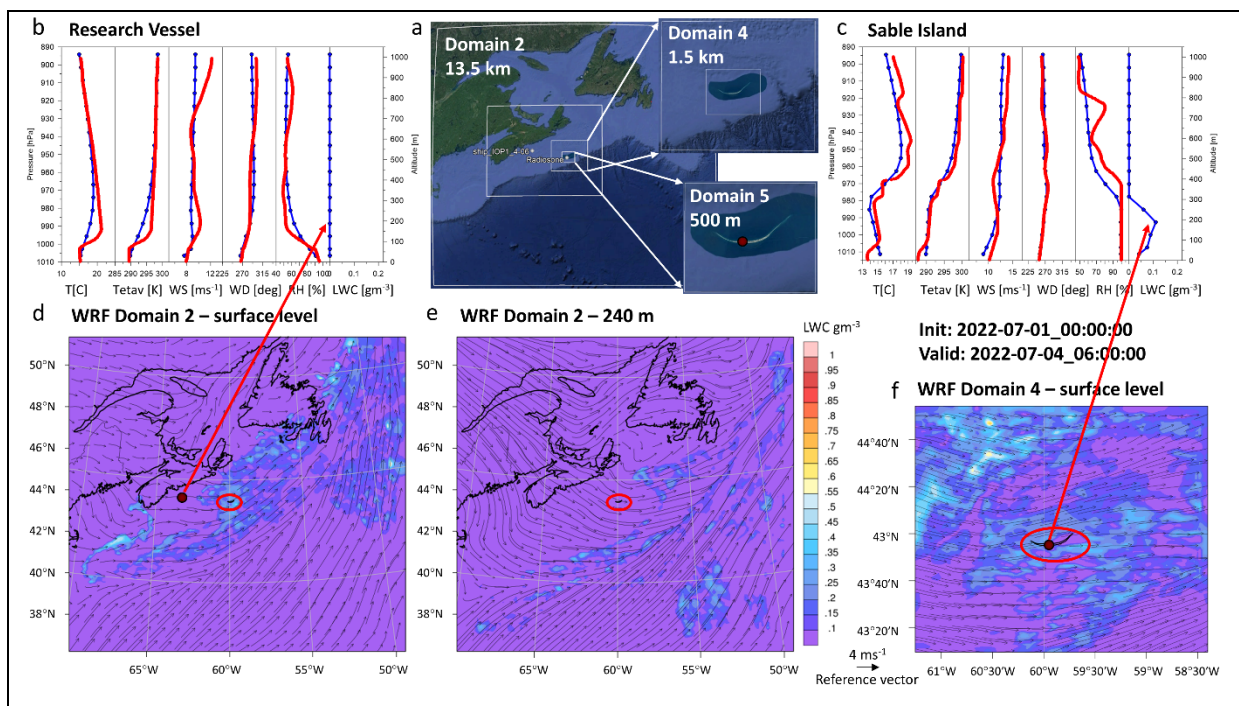
764

765 **Appendix E: WRF Simulation of IOP1, Illustrating Synoptic Influence on Fog Genesis**

766 Following the identification of synoptic trigger in fog formation during IOP1, WRF
 767 V3.9.1 with the Advanced Research WRF (ARW) dynamical solver (Skamarock et al. 2008)
 768 was used for detailed studies of relevant physical processes. Therein, six Lambert projection
 769 nested domains with parent-to-child horizontal resolution ratio of 3:1 and resolution from 40.5
 770 km to 500 m were used. Modifications were made to the static data of topography and land use
 771 to accurately capture the details of Sable Island. Two arc-second digital elevation datasets were
 772 implemented: Shuttle Radar Topography Mission SRTM 1 (NASA;
 773 <https://lta.cr.usgs.gov/SRTM1Arc>) and North American Land Cover Monitoring System
 774 NALCMS_2015_30m data (USGS; <http://www.cec.org/nalcms>). The NALCMS 19 classes
 775 were adapted to the modis_landuse_20class_30s_with_lakes land cover data; for a full
 776 description of general procedure, see Vladimirov et al. (2018). The model was implemented
 777 with 50 pressure-based terrain-following vertical levels with more levels in the lowest 1 km.
 778 The model top was set to 50 hPa. The initial and boundary conditions were derived from the
 779 0.25°×0.25° NCEP Final Operational Model Global Tropospheric Analyses
 780 (<http://rda.ucar.edu/datasets/ds083.3/>) with datasets available every 6 h. The option for grid
 781 nudging (fdda) was used only for the outermost domain 1 (D1) for all vertical levels. The
 782 simple ocean mixed-layer model following Pollard et al. (1972) was activated as a model option
 783 to provide SST).

784 The WRF physics package included: the Radiative Transfer Model parametrization
 785 (Mlawer et al. 1997) for LW and Dudhia (1989) scheme for SWR to compute radiation at every
 786 1 min; Noah land surface model (Chen and Dudhia 2001); and the Grell-Freitas cumulus

787 parametrization, for the first two domains only (Grell and Freitas 2014). The same
 788 configuration was used in Dimitrova et al. (2021) covering the identical area. Therein different
 789 microphysical and PBL parametrizations were compared and the two-double-moment option
 790 of the National Severe Storms Laboratory (NSSL) microphysics scheme (Mansell et al. 2010)
 791 was found to perform better than alternative schemes tested, when used with both non-local
 792 (Yonsei University; Hong et al. 2006) and local (Mellor–Yamada, Nakanishi and Niino level-
 793 2.5 parametrizations; Nakanishi and Niino 2006) planetary boundary layer (PBL) schemes.
 794 Therefore, the same NSSL microphysics and Shin-Hong PBL schemes (Shin and Hong, 2015),
 795 coupled with Revised MM5 Monin-Obukhov surface layer scheme (Jiménez et al. 2012) were
 796 selected for Fatima-GB simulations. The new Shin-Hong PBL scheme has been developed to
 797 address the so called “grey zone” challenges by using scale aware PBL parametrizations; they
 798 implement scale-dependent vertical transport in convective conditions and vertical mixing in
 799 the stable PBL and free atmosphere.



800

801 Figure E-1: (a) Domains used for WRF simulations, (b) simulated vertical profiles of main
 802 meteorological variables compared with observations from R/V-Condor located in domain 2
 803 (red – observations, blue – simulations); (c) Observations versus simulations from Sable Island
 804 located in Domain 5; (d) horizontal sections of LWC at the surface level for Domain 2; (e)
 805 LWC for 240 m elevation for Domain 2; (f) Surface level for Domain 4 showing that LWC or
 806 fog is confined beneath an inversion layer. The surface velocity vectors are
 807 westerly/southwesterly at the Sable Island, (d, f). Simulations were started at 0000 UTC on 01
 808 July, the plots shown are at 0600 UTC 04 July. Sable Island is encircled by a red ellipse and
 809 R/V-Condor by a red circle. No fog was observed at R/V-Condor during this IOP at SI (Fig.
 810 4).

811 WRF results of IOP1 are presented in Figure E-1, in the context of synoptic triggers
812 discussed in Fig. 7 of the paper. For brevity, a time (06:00 UTC, 04 July) between the long and
813 short fog periods are presented. The simulation results are in reasonable agreement with the
814 data taken at R/V-Condor and SI. Synoptic conditions prior to fog formation were a deep low-
815 pressure center over NE Canada with a trough that extended along the Atlantic coast and over
816 the Sable Island with strong southwesterly winds and a broad cloud band, in agreement with
817 Fig. 7 (a,b). An eastbound ridge encroached existing surface moisture and clouds, causing fog.
818 Fog coverage followed the line of convergence below the inversion layer (also see Hintz et al.
819 2024). Fog formation was most likely due to the convergence of the flow within a thin marine
820 boundary layer topped by an inversion layer (domain 4) as discussed following the Fig. 7(d).
821 The presence of deeper isothermal layers topped by dry inversions as a precursor to the second
822 fog event was also evident from domain d04 simulations.

823 **Appendix F: Delving into Recondite Bioaerosol Connection**

824 (i) AFIT/NPS deployed CINCS, a unique instrument that was specifically adapted for
825 bioaerosols detection. CINCS consists of two primary components: (i) Uniquely engineered
826 Liquid Spot Sampler (LSS) that ‘gently’ ingests ultra-fine through coarse mode aerosols
827 (ranging in size from 5nm through 10um); and (ii) Electro-chemical Detection Sensor (EDS)
828 that employs square-wave voltammetry (SWV) and electrodes treated with antibodies specific
829 to bioaerosol of interest (*Pseudomonas syringae* - *PS*). The LSS operates on the same principles
830 as that associated with standard, nano-aerosol condensation particle counting CPC (Balendra
831 et al. 2024; Deng et al. 2024). The initial SWV data as profiled in the Fig. F-1 suggest an
832 increased presence of *PS* on 29 and 30 July as compared to the other days. It is noted that this
833 is the very first deployment of CINCS, and to evaluate actual quantities of *PS* a controlled
834 calibration series (say with FM120) is necessary, which was not possible in time for Fatima-
835 GB due to scheduling conflicts.

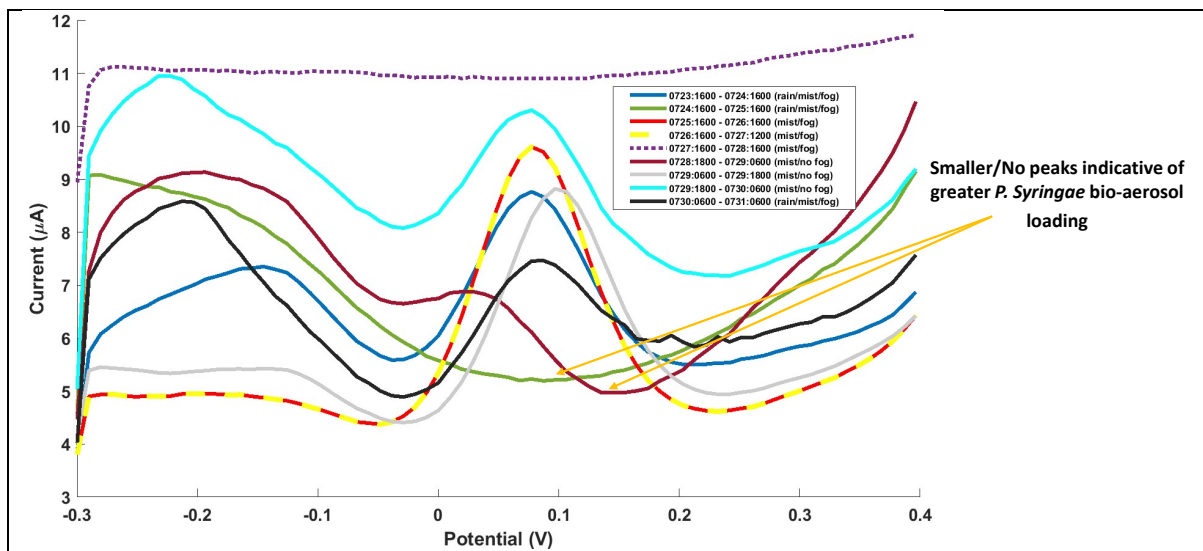


Figure F-1: Initial SWV results. Decreased and/or no peaks in the output current suggest an increased proportion and loading of *PS* in the Sable Island ambient air. Note smaller peaks (greater *PS*) on 29 and 30 July, indicating possible association of rain with *PS* population. Note that during 0727:1600 and 0728:1800 plots represent periods that SWV failed and hence anomalous SWV tests. (Time is in ADT)

836 (ii) The MBS deployed by UMAN detects primary bioaerosols and fluorescent
 837 aerosols in real-time via the interrogation of single particle autofluorescence and morphology.
 838 The MBS excites a single particle with a 280 nm filtered Xenon flashlamp and detects resultant
 839 fluorescent emissions over 8 channels between 305 and 655 nm. Particle size is resolved via
 840 Mie scattering of a 635 nm laser (detection range of 0.5 to 15 μm in diameter) and particle
 841 morphology is approximated via recording of two parallel chords of the 2D scattering pattern
 842 with a dual CMOS array; for a full description, see Crawford et al. (2023). Classification of
 843 particles into representative groups of interest was accomplished using the single particle
 844 fluorescent spectra, following Freitas et al. (2022). First, 3-sigma and 9-sigma thresholding is
 845 conducted simultaneously to retain weakly fluorescent populations of interest (e.g., sea spray
 846 with organic content), clipping all negative values in each channel at 0 after threshold
 847 subtraction (Crawford et al. 2020). FSSA are defined as those which exceed the 3-sigma
 848 threshold but not the 9-sigma threshold; HFSSA exceeds the 9-sigma threshold where the
 849 maximum intensity is not observed in the 2nd channel; and PBAP exceed the 9-sigma threshold
 850 with the maximum intensity observed in the 2nd channel. Particles which do not exceed the 3-
 851 sigma threshold are classified as non-fluorescent. A timeseries of the different classes is then
 852 produced using a 5-minute integration period, which is shown in Fig. F-2 (a,b).

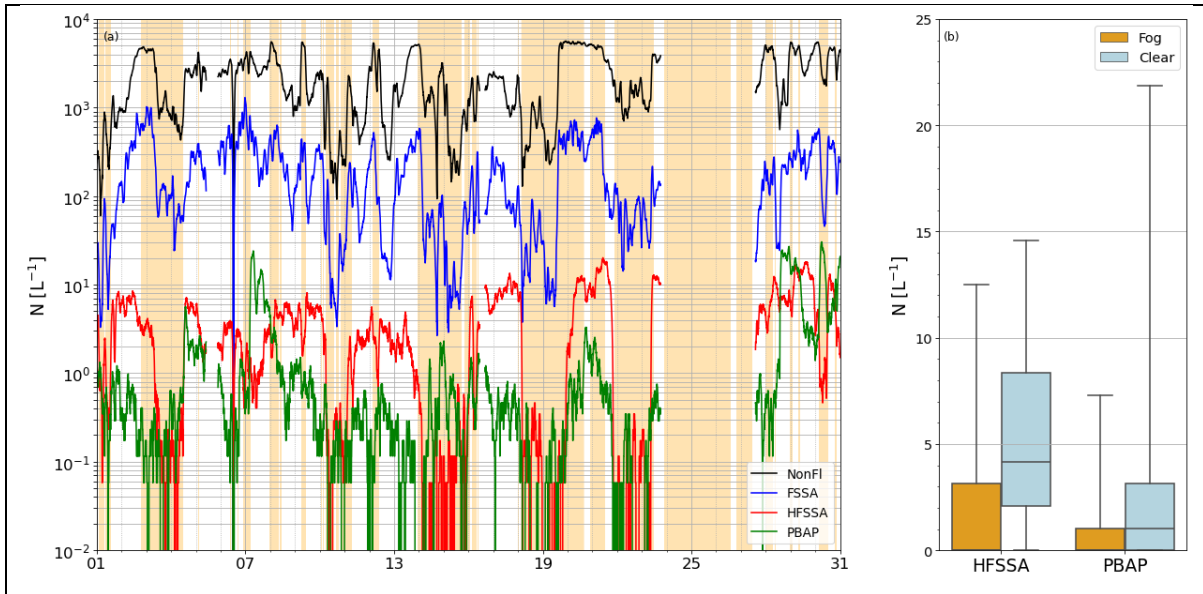
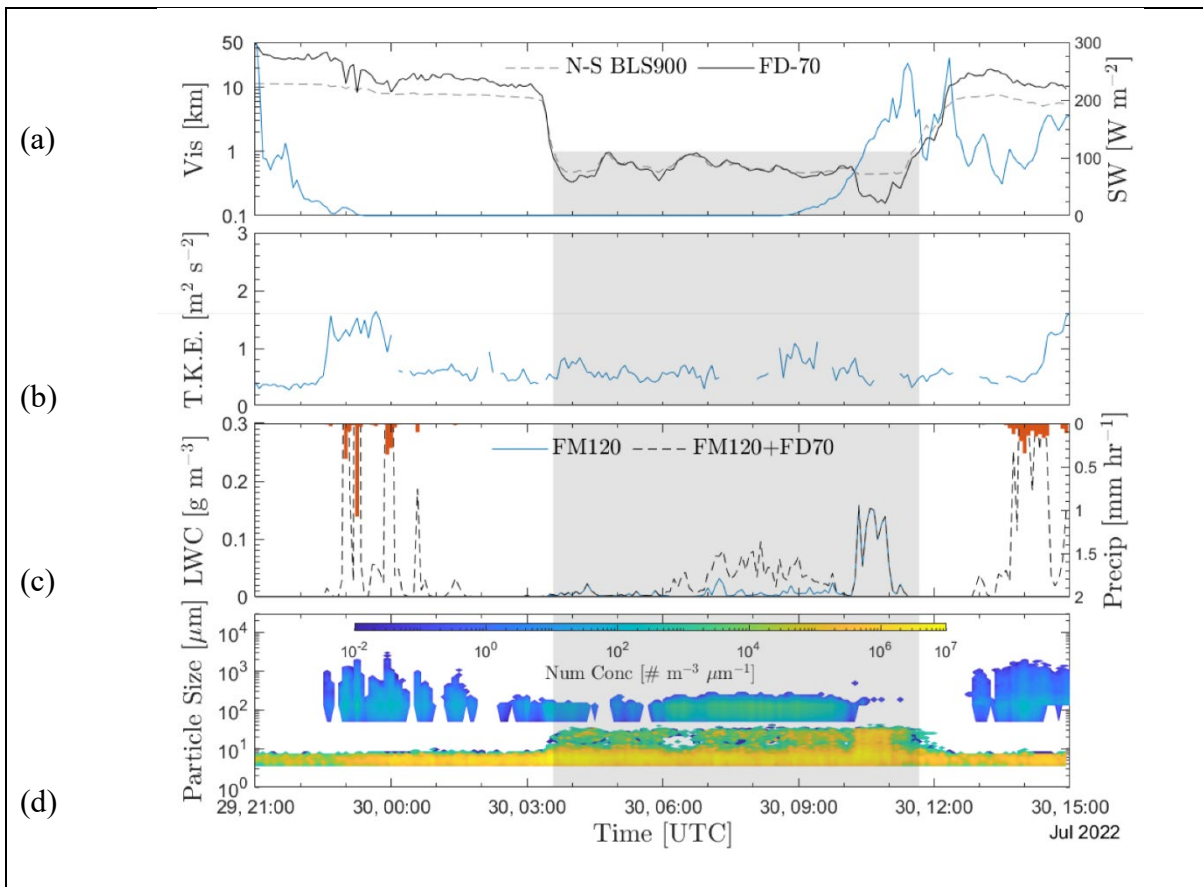


Figure F-2: (a) MBS aerosol concentrations N from 01-31 July based on above characterization. A 3-hourly rolling average has been applied to the 5-minute integrated timeseries for clarity. Shading shows fog periods identified by (1-min averaged) visibility < 1 km. (b) A box and whisker plot showing the impact of fog on the HFSSA and PBAP classes. Whiskers denote 5th and 95th percentile.

853



854 Figure G-1: (a) Timeseries of visibility from FD70 and BLS900 scintillometer along with net SWR
 855 (blue). SWR and FD70 were both near the Center tower while scintillometer gave a spatially integrated
 856 measurement from the North tower to the South tower. Thus, a disparity between FD70 and BLS900

857 indicate hydrometeor inhomogeneities. (b) Time series of TKE from the 8-m level at the Center tower.
858 (c) LWC calculated from FM120 as well as the combined LWC from the FM120 and FD70. Red
859 indicates precipitation from FD70. (d) Timeseries of droplet size distribution from FD70 and FM120.
860 Gray highlighted area denotes persistent fog. Note that the number concentration from FD70 is only an
861 estimate, which should be viewed with circumspection along with the corresponding LWC retrievals.
862

863 **Appendix G: Homogeneity of Fog Across SI and Monitoring Droplet Evolution**

864 Useful microphysical and visibility data that supplement meteorological information in
865 Fig. 9 pertinent to a cloud-lowering fog event is given in Fig. G1.

866 **Appendix H: A Brief Overview of COAMPS® Modeling**

868 Coupled Ocean Atmosphere Mesoscale Prediction System (COAMPS®) was used in
869 real-time to support Fatima-GB, wherein 48-hour forecasts were launched four times a day at
870 00, 06, 12 and 18 UTC. The numerical setup for the Sable Island utilized three nested domains
871 with decreasing horizontal grid spacing from 9 to 1 km, as shown in Fig. H1. In the vertical
872 direction, there were 23 model levels in the lowest 1 km, starting at 3 m close to the surface,
873 then increasing with height, for a total of 68 layers with the model top at 28 km. The time step
874 for the coarsest mesh was 30 s. The grids encompassing the position of R/V-Condor was also
875 evaluated.

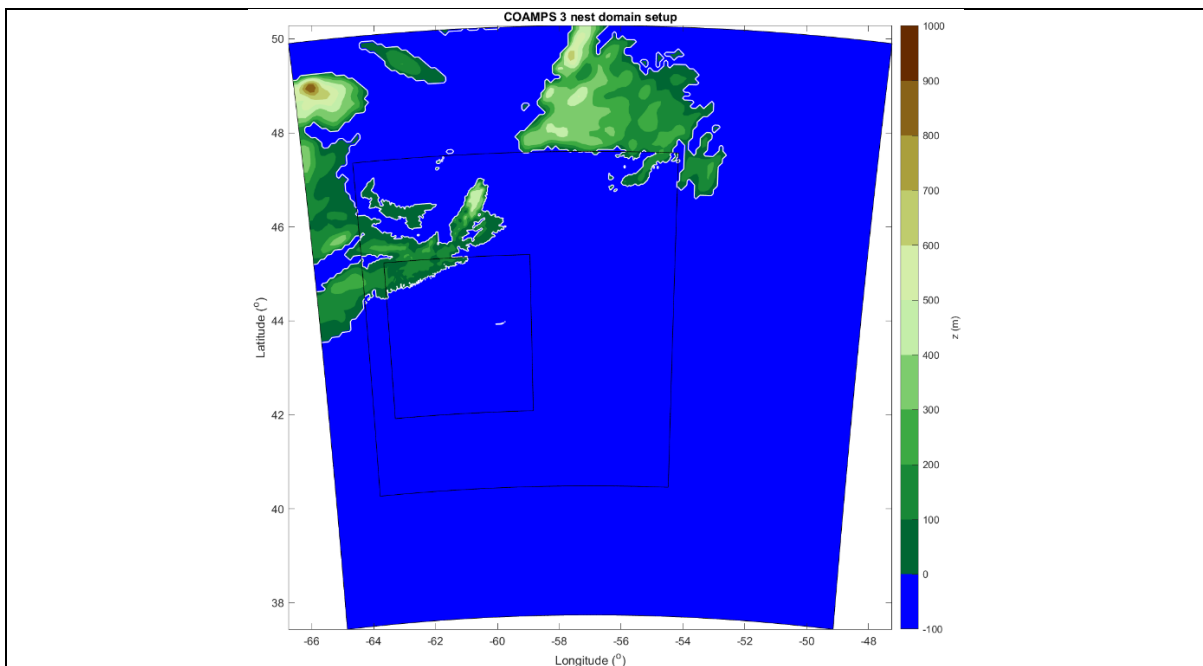


Figure H-1: COAMPS® nests (9, 3, and 1 km) over the Northwestern Atlantic, centered over Sable Island, used for the real time support of Fatima-GB

876 COAMPS® is a fully compressible, non-hydrostatic limited area model developed and
877 used operationally by the US Navy (Hodur 1997). The initial and lateral boundary conditions
878 for COAMPS® were provided using GFS fields. The sea surface temperature gradient between

879 the Labrador Current and Gulfstream that plays an important role in fog life cycle is relatively
880 stationary during each forecast (not shown), justifying not coupling the ocean component in
881 COAMPS[®]. The SST was captured by the data assimilation cycle, and provided as the bottom
882 boundary condition for the atmospheric component of COAMPS[®].

883 Appendix I: Satellite Evidence of Fog Shadow

884 Brightness Temperature Difference (BTD) fields observed by specific wavelength
885 channels of satellites can be used to roughly identify smaller water droplets (and hence fog or
886 stratus) in the lower atmosphere (Amani et al. 2020). This property was exploited to identify
887 Sable Island's fog shadow in the images of GOES-18 satellite shown in Fig. I-1. Fog shadow
888 extends well beyond the spatial resolution limits of GOES-18.

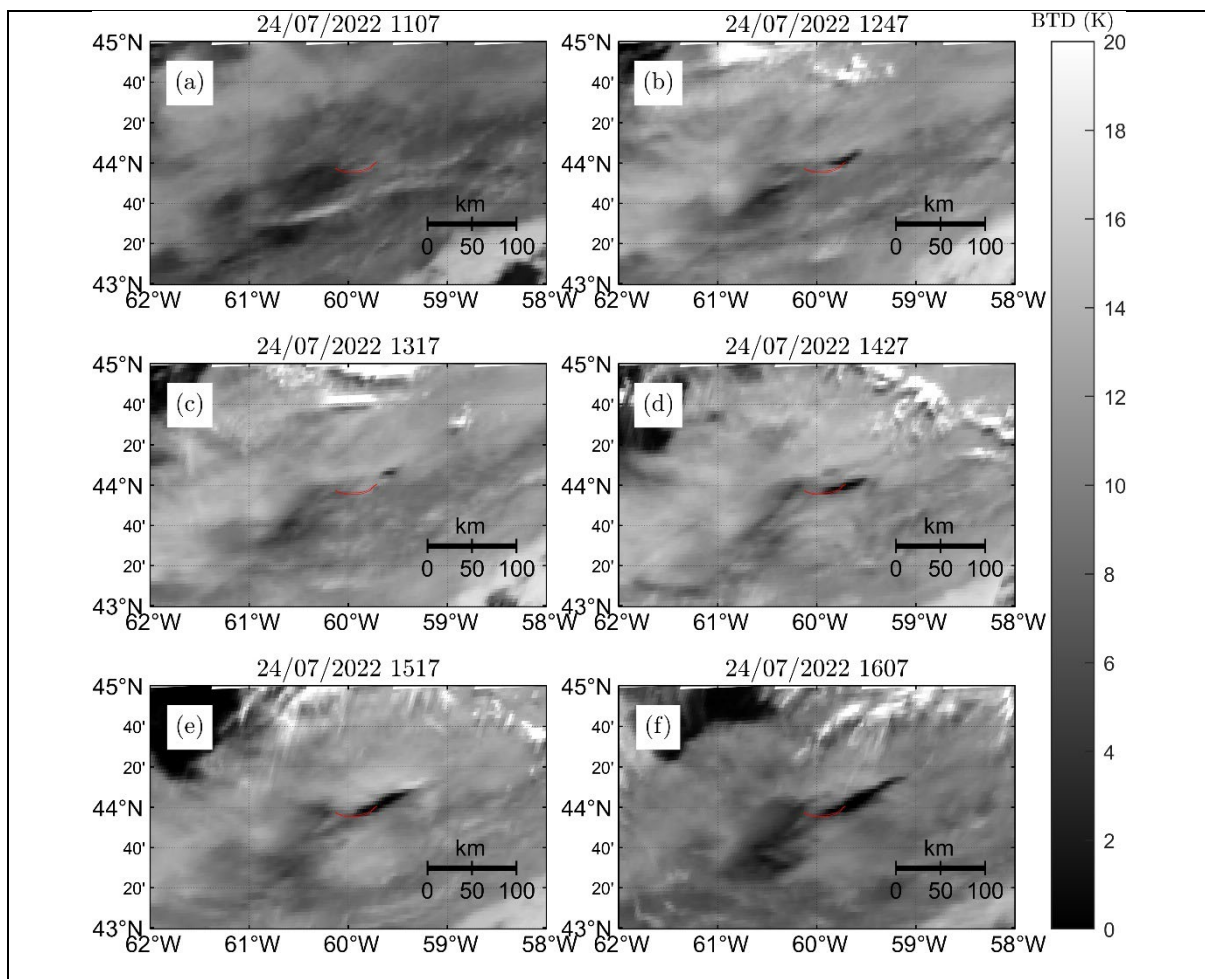


Figure I-1: BTD calculated based on (10.35 μm - 3.9 μm) wavelength channels of GOES-18 satellite observed in the vicinity of Sable on July 24, 2022 (IOP10) at different observation times; see Bardoel et al. (2024). The times of images are shown on the top in ADT (Atlantic Daylight Time). A region of improved visibility appears after 1200 ADT on 24 July (dark region) in the lee (northeast) of Sable that persists, with varying intensities, at least until 1600 ADT. The dark region that extends ~ 30 km downstream can be construed as the 'fog shadow' predicted by COAMPS[®].

889 Appendix J: Simulating Fog Dynamics via Coupled Modeling

890 LES resolves turbulent eddies down to the scale of grid-size, and provides insights into
 891 much smaller microscale conditions that govern the lifecycle of fog. Following Fatima-GB,
 892 LES coupled with LSD and LCM models (dubbed L^3) helped understand and predict
 893 microscale dynamics of fog. L^3 solves the following governing equations numerically using a
 894 finite-difference spatial discretization and second-order time integration. The role of each term
 895 is identified beneath the curly brackets.

$$\begin{aligned}
 \frac{\partial \tilde{u}_i}{\partial t} = & \underbrace{-\tilde{u}_j \frac{\partial \tilde{u}_i}{\partial x_j}}_{\text{resolved}} - \underbrace{\frac{1}{\rho_0} \frac{\partial \tilde{p}}{\partial x_i}}_{\text{pressure}} - \underbrace{\frac{\partial \tau_{ij}}{\partial x_j}}_{\text{subgrid}} + \underbrace{\delta_{i,3} \frac{\tilde{\theta}_v - \langle \tilde{\theta}_v \rangle}{\tilde{\theta}_v}}_{\text{buoyancy}} + \underbrace{\varepsilon_{ij3} f(\tilde{u}_j - \langle u_{g,j}^{LS} \rangle)}_{\text{Coriolis}} - \underbrace{\left\langle u_j^{LS} \frac{\partial u_i^{LS}}{\partial x_j} \right\rangle}_{\text{LS advection}} \\
 & - \underbrace{\langle w^{LS} \rangle \frac{\partial \tilde{u}_i}{\partial z}}_{\text{LS subsidence}} + \underbrace{\frac{1}{\tau_n} (\langle u_i^{LS} \rangle - \langle \tilde{u}_i \rangle)}_{\text{relaxation}} + \underbrace{\frac{1}{\rho_a} S^m}_{\text{source}}
 \end{aligned} \tag{J1}$$

$$\begin{aligned}
 \frac{\partial \tilde{\phi}}{\partial t} = & \underbrace{-\tilde{u}_j \frac{\partial \tilde{\phi}}{\partial x_j}}_{\text{resolved}} - \underbrace{\frac{\partial \pi_j}{\partial x_j}}_{\text{subgrid}} - \underbrace{\left\langle u_j^{LS} \frac{\partial \phi^{LS}}{\partial x_j} \right\rangle}_{\text{LS advection}} - \underbrace{\langle w^{LS} \rangle \frac{\partial \tilde{\phi}}{\partial z}}_{\text{LS subsidence}} + \underbrace{\frac{1}{\tau_n} (\langle \phi^{LS} \rangle - \langle \tilde{\phi} \rangle)}_{\text{relaxation}} + \underbrace{\frac{1}{\rho_a} S^h}_{\text{source}}
 \end{aligned} \tag{J2}$$

896 Here, \tilde{u}_i is the filtered velocity and θ_v the virtual potential temperature. $\tilde{\phi}$ is a generic
 897 scalar, which can be either the potential temperature ($\tilde{\theta}$) or the total specific humidity (\tilde{q}). The
 898 large-scale advective tendencies and subsidence and the Coriolis term that accounts for the
 899 large-scale pressure gradients are the LSD terms. A relaxation term is introduced as a
 900 safeguard, nudging the LES toward a true mean state. A dynamic subgrid-scale (SGS) model
 901 developed by Germano et al. (1991) is used for modeling SGS stresses. The LCM model
 902 addresses the interaction between fog droplets and the background flow, providing a detailed
 903 representation of fog formation and growth processes.

904 The size of the computational domain used to simulate the Hibernia area, a locality
 905 covered by R/V-Condor, is 500 m x 500 m x 500 m in the x, y and z (upward) directions,
 906 respectively. This domain is divided into 128 x 128 x 128 grid points with 3.9 m grid spacing
 907 in each direction. Periodic boundary conditions are applied horizontally, while at the bottom
 908 surface the Monin-Obukhov similarity theory defines surface conditions with a roughness
 909 length of 3.2×10^{-5} m. The ocean surface is forced by SST derived from ERA5, updated hourly,

924 and specific humidity is adjusted to maintain 100% relative humidity at the surface. The large-
 925 scale tendencies are derived from ERA5 and interpolated on the LES grid. The relaxation time
 926 is set to 1 hour. For the LCM, the initial aerosol distribution is based on the C-FOG campaign
 927 data (Fernando et al. 2021) and includes accumulation and coarse modes with peaks at 0.1 μm
 928 and 1 μm with hygroscopicities of 0.6 and 1.2, respectively.

929 **Appendix K: Instrumentation for Fatima-GB**

930 Instruments and instrument systems used in Fatima-GB are given below.

931 **Table K1: Instrumentation on R/V Atlantic Condor**

Instrument	Manufacturer & Model	Measurement	Location	Institution
Microwave Rain Radar (MRR)	METEK MRR-PRO	Vertical profiling of droplet size distribution, rain rate and liquid water content	On ship	UND
Vertical Microstructure Profiler (VMP)	Rockland Scientific Uprising VMP-250	Ocean microstructure, turbulent kinetic energy dissipation evaluation	On ship	UND
Optical Disdrometer	Eigenbrodt ODM 470	Rain drop or snow particle size distribution	On ship	UND
Remote Ocean Sensing Radiometer (ROSR)	Remote Measurements & Research Co.	Sea-surface skin temperature (SSST)	On ship	UND
Microwave Radiometer	Radiometrics MP-3000A	Vertical profile of temperature, water vapor and liquid water	On ship	UND
Visible and Cloud/IR Cameras	Moonglow Technologies SKY Camera; FLIR DUO Pro R IR Thermal Camera	Full color video view of the entire sky; real-time image capture plus MSX multi-spectral imaging enhancement	On ship	UND
Visibility and Present Weather Detection (PWD) Sensor	Vaisala FD70	Meteorological condition code and MOR (visibility), rain drop or snow particle size distribution	On ship	UND
Ceilometer-CL61	Vaisala CL61	Vertical profiles of aerosol backscatter with depolarization; precipitation, differentiation between solid, liquid and mixed-phase clouds	On ship	UND
Scanning Doppler Lidar	Halo Photonics Streamline Allsky	Profiles of Doppler velocity and fluctuations, aerosol backscatter	Motion-Stabilized Platform	UND
W-Band FMCW Cloud Radar	Radiometric Physics RPG-FMCW-94-DP-G1	Vertical profiles of Reflectivity, Doppler Velocity, 2.2 mm wavelength, range resolution 1 m, information of scatterers (rain, clouds, snowflakes, fog)	Motion-Stabilized Platform	UND
CTD	SeaBird SBE 25plus	Conductivity, Temperature and Depth sensors, and	On ship	UND/MEOPAR

		auxiliary sensors — dissolved oxygen, pH, fluorescence, oil, radiance, light transmission, turbidity, nitrates		
300 kHz ADCP	Teledyne Workhorse	Ship mounted, bottom referenced velocity and current profile measurement	On ship	UND/MEOPAR
Sea Snake	Built by NOAA (YSI 46040 precision thermistor in a custom-fabricated floating hose)	Sea surface temperature at ~ 3-5 cm below sea surface	On ship	UND/PSL-NOAA
3D Ultrasonic Anemometer	Gill Gill R3A	3D wind velocity (@20Hz at 18.6m above the surface	(Ship) Bowmast	PSL-NOAA/UND
Fast Water Vapor Infrared Gas Analyzer	LiCOR 7500A	Water vapor (@10Hz) at 18m above the surface	Bowmast	PSL-NOAA/UND
Weather Transmitter	Vaisala WXT520	Temperature, RH, pressure, rain and wind speed/direction (@ 1Hz) at 18m above the surface	Bowmast	PSL-NOAA/UND
GPS Heading System	Hemisphere Crescent VS100	GPS coordinates	Bowmast	PSL-NOAA/UND
HMP Pressure Sensor	Vaisala	Pressure at 16.25 m above the surface	Bowmast	PSL-NOAA/UND
Pyrometers	Eppley PIR	Downwelling longwave radiative flux (on the bridge at ~ 16-17 m height)	Bowmast	PSL-NOAA/UND
Pyrometers	Kipp & Zonen CM22 and CMP22	Downwelling shortwave radiative flux (on the bridge at ~ 16-17 m height)	Bowmast	PSL-NOAA/UND
Moored Wave Buoy	Sofar Ocean, Spotter	Ocean wave directional spectra and bulk wave statistics (significant wave height, direction, period), bulk water temperature	3 km south of Sable Island	NPS
Rawinsonde (Vaisala MW41)	Vaisala DigiCORA MW41 Sounding System	Upper air soundings of temperature, relative humidity, pressure, wind speed and wind direction	Off ship	NPS
Ocean Surface and Scene Visualization Cameras	1x Campbell Scientific Field Camera, 2x InVid Technology Bullet Cameras	Optical/Infrared images (full motion video and stills)	On ship	NPS
Integrated CO2 and H2O Open-Path Gas Analyzer and 3-D Sonic Wind Anemometer	Campbell Scientific IRGASON	Perturbation of three-dimensional wind vector, sonic air temperature, H2O/CO2 gas concentration	C-CAMS and D-CAMS	NPS
Dual Antenna GNSS-Aided Inertial Navigation System	VectorNav VN-300	Platform motion (GNSS position, velocity, attitude)	C-CAMS and D-CAMS	

Humidity and Temperature Probe	Vaisala HMP155	Bulk temperature and relative humidity	CCAMS and D-CAMS	NPS
Fast-Response Barometer	Paroscientific MET4A	Pressure perturbation w/ aspirated temperature and relative humidity	C-CAMS	NPS
Upwelling Infrared Pyrometer	Heitronics CT15.85	Radiometric sea surface temperature (9.6 - 11.6 μm)	C-CAMS and D-CAMS	NPS
Net Radiometer	Apogee SN-500-SS	Net longwave and shortwave radiation	C-CAMS	NPS
Radar Altimeter	Ainstein US-D1	Surface elevation	C-CAMS	NPS
Soot Photometer	Brechtel Tricolor Absorption Photometer (TAP)	Aerosol absorption (red, green, blue)	C-CAMS	NPS
Portable Optical Particle Spectrometer	Handix Scientific POPS	Aerosol size spectra (120 nm - 3 μm)	C-CAMS	NPS
Visibility and Present Weather Detection (PWD) Sensor	Campbell Scientific CS-125	Infrared forward-scattering meteorological optical range (visibility)	C-CAMS and D-CAMS	NPS
Fog Monitor	Droplet Measurement Technologies FM120	Droplet size spectra (2 - 50 microns)	C-CAMS and D-CAMS	NPS
3-Wavelength Integrating Nephelometer	EcoTech Aurora 3000	Aerosol scattering (red, green, blue)	On ship	AFIT/NPS
Black Carbon Aethalometer	Magee Scientific AE33	Aerosol absorption (7 wavelength, UV-NIR)	On ship	AFIT/NPS
(Water-based) Condensation Particle Counter	Aerosol Devices MAGIC210 CPC	Aerosol number concentration (5nm - 2.5 μm), moderated aerosol growth with internal water cycling, condensation particle counter	On ship	AFIT/NPS
Pygeometer	Apogee SL-510, SL-610	Longwave down- and upwelling radiation	TLS Mounted on ship	UU
Optical Particle Counter (OPC)	AlphaSense OPC-N3 model	PM1, PM2.5, PM10 and particle size distribution (0.35 to 40 μm with 24 bins)	TLS Mounted on ship	UU
Fog Water Collector	Caltech Active Strand Cloud Water Collector 2	Droplets > 3.5 μm	On ship	DU
Scanning Mobility Particle Sizer (SMPS)	TSI Inc. 3938 Differential-Mobility Analyzer 3081 + Electrostatic Classifier 3082 + Condensation Particle Counter 3772	Submicrometer particle size distribution: Aerosol size spectra 10 - 500 nm	On ship	DU
Aerodynamic Particle Sizer (APS)	TSI Inc. 3321	Aerosol size spectra (0.36 to 13 μm)	On ship	DU
Fog Monitor	DMT FM120	Droplet size spectra (2 μm - 50 μm)	On ship	DU
Back-Scatter Cloud Probe	DMT BCP	Particle size distribution (5 μm to 75 μm)	Gondola	OntTechU

Cloud Droplet Probe	DMT CDP-2	Particle size distribution (2um to 50 µm)	Gondola	OntTechU
Micro Orifice Uniform Deposit Impactor (MOUDI)	Model 100-NR, MSP Corp (A TSI Company), Shoreview, MN	0.1-10 µm, aerosol during fog	On ship	YorkU
Nano-MOUDI-II	Model 122-R, MSP Corp (TSI)	0.01-10 µm, ambient aerosol	On ship	YorkU
Ion Chromatograph	Thermo Scientific ICS-6000	Aerosol major anions and cations	On ship	YorkU
Gas Monitors	Ecotech EC9841, EC9830, S10, S40	CO, NO, NO2, total reactive nitrogen, NH3, and O3	On ship	YorkU
Fog Monitor	DMT FM-120	Droplet size spectra (2um - 50 um)	A/V Wallace	Scripps/UCSD
Flux Mast (sonics)	Gill R3-50 (x2)	3D wind speed & fluxes	A/V Wallace	Scripps/UCSD
Towed CTD	RBR Concerto	Ibid, Dissolved Oxygen, Fluorometer	A/V Wallace	Scripps/UCSD
500 Hz ADCP (downward looking)	Nortek Signature 500	Current profiler	A/V Wallace	Scripps/UCSD
Visible and IR 360 Camera	ASV	Surface IR and visible imagery	A/V Wallace	Scripps/UCSD
X-Band Radar	Furuno	X-Band backscatter	A/V Wallace	Scripps/UCSD
3D Ultrasonic Anemometer	Gill R3-50	3D winds and fluxes	Wave Gliders (x3)	Scripps/UCSD
Weather Station	Vaisala WXT530	Temperature, RH, pressure, rain and wind speed/direction (@ 1Hz)	Wave Gliders (x3)	Scripps/UCSD
CTD	Seabird GPCTD	Ibid, at the surface and sub depth (~8-9m)	Wave Gliders (x3)	Scripps/UCSD
300 KHz ADCP	Teledyne Workhorse	Ibid, Current profile	Wave Gliders (x3)	Scripps/UCSD
Upward-Looking Current Profiler	Nortek Signature 1000	Upward-looking current profiler at 8m depth	Wave Gliders (x3)	Scripps/UCSD
Dual GPS Receiver	Hemisphere V104	Position, platform velocity, and directional wave spectra	Wave Gliders (x3)	Scripps/UCSD
CTD	RBR Concerto installed on profiling Winch	Ibid, profiling from 8m to 150m depth (installed on only one Wave Glider)	Wave Gliders (x3)	Scripps/UCSD
GPS-IMU	Novatel SPAN OEM7720 GPS Receiver with Dual GPS Antennas and Epson EG320N IMU	Position, platform attitude and velocity, directional wave spectra	Wave Gliders (x3)	Scripps/UCSD

932

933 **Table K2:** Instrumentation on Sable Island

Instrument	Manufacturer & Model	Measurement	Institution
Visibility and Present Weather Detection (PWD) Sensor	Vaisala FD70	Ibid	UND

Visibility and Present Weather Detection (PWD) Sensor	Vaisala PWD22	Meteorological condition code and MOR (meteorological optical range, or visibility)	UND
Scanning Doppler Lidar	Halo Photonics Streamline Allsky	Ibid	UND
Super Combo Probe	In-House Built (miscellany of hotwire and nanowire sensors aligning with the wind to capture dissipation scales)	High frequency measurement of wind velocity and temperature fluctuations with resolution approaching dissipation scales	UND
Net Radiometers	Campbell Scientific CNR1 Net Radiometer	Net LW/SW radiation	UND
Fast Water Vapor Infrared Gas Analyzer	LI-COR LI-7500A	Ibid	UND
Sonic Anemometers	Gill Gill R3A	ibid	UND
Fine Wire T/Relative Humidity Sensors	Vaisala HMP45C	Temperature and RH	UND
Ceilometer-CL31	Vaisala CL31	Vertical profiles of aerosol backscatter	UND
Microwave Radiometer (MWR)	Radiometrics MP-3000A	ibid	NPS
Wind Profiling Monostatic Sodar	Scintec SFAS	Vertical profiles of wind speed/direction and structure function parameter of temperature (10-500 m)	NPS
Scintillometer	Scintec BLS 900	Fried parameter (r_0), structure function parameter of index of refraction (C_n^2)	NPS
Differential Imaging Motion Monitor	NAWCWD China Lake - DIMM	Fried parameter (r_0), structure function parameter of index of refraction (C_n^2)	NPS
Wide Angle Teleradiometric Transmissometer	NAWCWD China Lake - WATT	Optical transmission	NPS
Non-coherent Extended Source Beacon	NAWCWD China Lake - NESB	Shortwave IR transmitter for DIMM/WATT systems	NPS
Rawinsonde (Vaisala MW41)	Vaisala DigiCORA MW41 Sounding System	Upper air soundings of temperature, relative humidity, pressure, wind speed and wind direction	NPS
Tethered Lifting System (TLS); Balloon and Winch	Allsopp Helikite DS25	Lifting meteorological payload to various elevations	NPS
Visibility and Present Weather Sensor	Campbell Scientific CS-120	Infrared forward-scattering meteorological optical range (visibility)	NPS
Cloud Droplet Probe (CDP) on communication tower	DMT CDP-2	ibid	NPS
Transmissometer	Vaisala LT31	Optical transmission	NPS
Differential Temperature Sensor (DTS)	Omega Type-E Thermocouple	Structure function parameter of temperature (CT_2) from 3 unequally spaced fast-response thermocouples	NPS
Integrated CO ₂ and H ₂ O Open-Path Gas Analyzer and 3-D Sonic Wind Anemometer	Campbell Scientific IRGASON	Ibid	NPS
Video Cameras	Axis Communications M30 Dome Camera	Visual documentation of environmental conditions	NPS

Microwave Rain Radar (MRR)	METEK MRR-PRO	Ibid	UU
Ceilometer-CL31	Vaisala CL31	Ibid	UU
EM Scintillometer (TX and RX: Transmitter and Receiver)	Scintec BLS-900#1TX, BLS-900#1RX,	Atmospheric turbulence, heat flux and crosswind	UU
Microwave Scintillometer (MWS)	Radiometer Physics RPG-MWSC-160 (TX and RX)	Sensible and latent Heat Fluxes	UU
Precision Radiation Balance Sawhorse	CGR4 pyreometers, CMP21 pyranometers, up- and downwelling; in-house built	4 components of SW, LW and net radiation	UU
Pyreometer (on TLS)	Apogee SL-510, SL-610	Longwave down- and upwelling radiation	UU
Optical Particle Counter	Alphasense OPC	PM1, PM2.5, PM10 and particle size distribution (0.35 to 40 μm with 24 bins N3)	UU
Visibility Cameras (Webcams)	Microseven 5MP	Time lapse photos (1 per minute)	UU
LWC Probes	in house built	liquid water content	UU
Self-Calibrating Soil Heat Flux Sensor	Hukseflux HFP01SC	Soil heat flux	UU
30 cm Soil Moisture and Temperature Sensor	Campbell Scientific CS650	Soil moisture and temperature	UU
Averaging Soil Thermocouple Probe	Campbell Scientific TCAV	Soil temperature	UU
Visibility and Present Weather Sensor	Campbell Scientific CS125	Infrared forward-scattering meteorological optical range (visibility)	UU
LEMS (automated weather station)	In-house assembled	T, RH, wind speed and direction, soil T, surface T, SW and OPC-N3 (0.38 - 17 μm with 24 bins)	UU
Ceilometer	Vaisala CL51	Vertical profiles of aerosol backscatter	OntTechU
Weather Transmitter	Vaisala WXT520	Ibid	OntTechU
Visibility and Present Weather Detection (PWD) Sensor	Vaisala PWD52	Meteorological condition code and MOR (visibility) and rain	OntTechU
Fog Monitor	DMT FM120	Ibid	OntTechU
Ground Cloud Imaging Probe (GCIP)	DMT	Particle size spectra (7.5 μm to 960 μm)	OntTechU
Young 3D Sonic Anemometer (Model 81000)	R.M. Young Company	Horizontal and vertical wind speed and direction and turbulence, 20Hz	OntTechU
Sunshine Pyranometer	Delta-T Devices SPN1	Global (Total) and diffuse irradiance; DNI (Direct Normal Irradiance) calculation	OntTechU
Digital Camera	General	Local pictures looking at the south	OntTechU
CINCS (Cloud Ice Nucleation Characterization System)	Aerosol Devices, Inc.	Bioaerosols tens of nm, possibly of fog/ice condensation nuclei nature	AFIT/NPS
Multi-parameter Bioaerosol Spectrometer (MBS-MR)	University of Hertfordshire	Ultraviolet-light induced fluorescence spectrometer; Primary bioaerosol particles, detection range 0.5-15 μm	UMAN

934
935

936 **Table K3:** Instrument Systems on R/V Atlantic Condor

System	Location	Institution
Bow Mast	Ship bow	PSL-NOAA/UND
C-CAMS	Crane operated (ship)	NPS
D-CAMS	Deck mounted on ship	NPS
Tethered System+Payload Lifting	Ship and Sable Island	ARL/UU/UND
Gondola	Ship (fixed)	OntTechU
Instrument Wave Glider	Launched from Ship	SCRIPPS/UCSD
R/V Wallace: Autonomous Boat Instrumented for Air-Sea Interaction Research	Launched from Ship	SCRIPPS/UCSD
Flux Towers (Appendix C)	Sable Island	UND/UU
LEMS	Sable Island	UU
Motion Stabilized Doppler Lidar	Ship	UND
Motion Stabilized W-Band Radar	Ship	UND
Super Combo Probe	Sable Island	UND
Radiation Balance Sawhorse	Sable Island	UU
Instrumented UAV (Unmanned Aerial Vehicle)	Sable Island/2 weeks	OntTechU
Microphysical Tower	Sable Island	OntTechU

937

938 **Appendix L: Commonly Encountered Acronyms**

939 (For acronyms for instruments, see Appendix K)

- 940 ABL – Atmospheric Boundary Layer
- 941 AGL – Above Ground Level
- 942 a.s.l – above sea level
- 943 BTD – Brightness Temperature Difference
- 944 COAMPS - Coupled Ocean/Atmosphere Mesoscale Prediction System
- 945 CTD – Conductivity, Temperature, Depth
- 946 DWR – Downwelling Radiation (Irradiance)
- 947 ERA5 – Fifth generation ECMWF atmospheric reanalysis
- 948 FCN – Fog Condensation Nuclei
- 949 FSSA – Fluorescent Sea Spray Aerosols
- 950 GFS – Global Forecast System
- 951 HFSSA – Highly Fluorescent Sea Spray Aerosols
- 952 IBL – Internal Boundary Layer
- 953 IOP/ISP – Intense Operational (or Study) Period
- 954 K – Kolmogorov
- 955 L3 – Coupling of LES, LSD and LCM
- 956 LCM – Lagrangian Cloud Model

957 LES – Large Eddy Simulations
958 LSD – Large Scale Dynamics
959 LEMS – Local Energy Budget Measurement System
960 LWC – Liquid Water Content
961 LWR – Long Wave Radiation
962 MABL – Marine Atmospheric Boundary Layer
963 MSLP – Measured Sea Level Pressure
964 MVD – Mean Volume Diameter
965 NWP – Numerical Weather Prediction Model
966 Nd – Aerosol Number Concentration
967 O-C – Obukhov-Corrsin Scale
968 PBAP – Primary Biological Aerosol Particles
969 RH – Relative Humidity
970 SLOP – Sable Lee Observing Period
971 SSA – Sea Surface Aerosols
972 SST – Sea Surface Temperature
973 SWR – Short Wave Radiation (Irradiance)
974 T – Temperature
975 TKE – Turbulent Kinetic Energy
976 WRF (ARW) – Weather Research and Forecasting Model (Advanced Research ARW)
977 WS and WD – Wind Speed and Direction

978

979 **References:**

980 Amani, M., Mahdavi, S., Bullock, T. and Beale, S., 2020: Automatic nighttime sea fog
981 detection using GOES-16 imagery. *Atmos. Res.*, 238, 104712.
982 Bardoel, S., Hoch, S., Ruiz-Placarte, J., Lenain, L., Gultepe, I., Grachev, A., Gaberšek, S.,
983 Wang, Q., and Fernando, H.J.S., 2024: Study of fog dissipation in an internal boundary
984 layer on Sable Island. *Quart. J. Roy. Meteor. Soc.*, Accepted.
985 Balendra, S., Kale, A., Pongetti, J., Kazemimanesh, M., Haugen, M., Weller, L. and Boies, A.,
986 2024: Condensation particle counters: Exploring the limits of miniaturization. *J.*
987 *Aerosol Sci.*, 175, 106266.
988 Barve, A., Gultepe, I., Fernando, H.J.S., Wang, Q., and Shen, L., 2024: Large Scale Dynamics
989 · Large-Eddy Simulation · Lagrangian Clous Modeling (L3) Coupling for Studying the
990 Marine Fog Life Cycle. *Quart. J. Roy. Meteor. Soc.*, Accepted

991 Bertram, T.H., Cochran, R.E., Grassian, V.H. and Stone, E.A., 2018: Sea spray aerosol
992 chemical composition: elemental and molecular mimics for laboratory studies of
993 heterogeneous and multiphase reactions. *Chem. Soc. Rev.*, 47(7), 2374-2400.

994 Bhushan, B., 2020: Design of water harvesting towers and projections for water collection from
995 fog and condensation. *Phil. Tran. Roy. Soc. A*, 378(2167), 20190440.

996 Boutle, I., Price, J., Kudzotsa, I., Kokkola, H. and Romakkaniemi, S., 2018: Aerosol–fog
997 interaction and the transition to well-mixed radiation fog. *Atmos. Chem. Phys.*, 18(11),
998 7827-7840.

999 Chen, F., and Dudhia, J., 2001: Coupling an advanced land surface–hydrology model with the
1000 Penn State–NCAR MM5 modeling system. Part I: Model implementation and
1001 sensitivity. *Mon. Wea. Rev.*, 129, 569–585. [https://doi.org/10.1175/1520-
1002 0493\(2001\)129<0569:CAALSH>2.0.CO;2](https://doi.org/10.1175/1520-0493(2001)129<0569:CAALSH>2.0.CO;2).

1003 Chisholm, N., Nagare, B., Wainwright, C., Creegan, E., Salehpoor, L., VandenBoer, T.C.,
1004 Bullock, T., Croft, B., Lesins, G., Osthoff, H. and Fernando, H.J.S., 2021:
1005 Characterizing Atmospheric Aerosols off the Atlantic Canadian Coast During C-
1006 FOG. *Bound. Layer Meteorol.*, 181, 345-364.

1007 Crawford, I., Topping, D., Gallagher, M., Forde, E., Lloyd, J.R., Foot, V., Stopford, C., and
1008 Kaye, P., 2020: Detection of Airborne Biological Particles in Indoor Air Using a Real-
1009 Time Advanced Morphological Parameter Uv-Lif Spectrometer and Gradient Boosting
1010 Ensemble Decision Tree Classifiers. *Atmos.*, 11, 1039.

1011 Crawford, I., Bower, K., Topping, D., Di Piazza, S., Massabò, D., Vernocchi, V., and
1012 Gallagher, M., 2023: Towards a UK Airborne Bioaerosol Climatology: Real-Time
1013 Monitoring Strategies for High Time Resolution Bioaerosol Classification and
1014 Quantification. *Atmos.*, 14, 1214. <https://doi.org/10.3390/atmos14081214>

1015 Crilley, L.R., Lao, M., Salehpoor, L. and VandenBoer, T.C., 2023: Emerging Investigator
1016 Series: An instrument to Measure and Speciate the Total Reactive Nitrogen Budget
1017 Indoors: Description and Field Measurements. *Environ. Sci.: Processes &
1018 Impacts*, 25(3), 389-404.

1019 Deng, Z., Ran, L., Xu, X., Yan, P., Tian, P., Lin, W., Wu, Y., Zhang, R., Pan, W. and Lu, D.,
1020 2024: Size-resolved Cloud Condensation Nuclei Activity of Aerosol Particles Sampled
1021 Above the Mixing Layer. *Aero. Sci. Tech.*, 1-13.

1022 Dimitrova, R., Sharma, A., Fernando, H.J.S., Gultepe, I., Danchovski, V., Wagh, S., Bardoel,
1023 S.L., and Wang, S., 2021: Simulations of Coastal Fog in the Canadian Atlantic with the

1024 Weather Research and Forecasting Model. *Boundary-Layer Meteor.*, 181, 443–472.
1025 <https://doi.org/10.1007/s10546-021-00662-w>.

1026 Dorman, C.E., Mejia, J., Koraćin, D. and McEvoy, D., 2020: World marine fog analysis based
1027 on 58-years of ship observations. *Intl. J. Climatol.*, 40(1), 145-168.

1028 Dorman, C.E., Mejia, J., Koraćin, D. and McEvoy, D., 2017: Worldwide marine fog occurrence
1029 and climatology. *Marine fog: Challenges and Advancements in Observations,*
1030 *Modeling, and Forecasting*, 7-152, Springer.

1031 Dudhia, J., 1989: Numerical Study of Convection Observed During the Winter Monsoon
1032 Experiment using a Mesoscale Two-Dimensional Model. *J. Atmos. Sci.*, 46(20), 3077–
1033 3107. [https://doi.org/10.1175/1520-0469\(1989\)046<3077:NSOCOD>2.0.CO;2](https://doi.org/10.1175/1520-0469(1989)046<3077:NSOCOD>2.0.CO;2).

1034 Fairall, C.W., Bradley, E.F., Hare, J.E., Grachev, A.A., and Edson, J.B., 2003: Bulk
1035 Parameterization of Air-Sea Fluxes: Updates and Verification for the COARE
1036 Algorithm. *J. Climate*, 16, pp 571-591.

1037 Farmer, D.K., Boedicker, E.K. and DeBolt, H.M., 2021: Dry deposition of atmospheric
1038 aerosols: Approaches, observations, and mechanisms. *Ann. Rev. Phys. Chem.*, 72, 375-
1039 397.

1040 Fathalli, M., Lac, C., Burnet, F. and Vié, B., 2022: Formation of Fog due to Stratus Lowering:
1041 An Observational and Modelling Case Study. *Quar. J. Roy. Meteor. Soc.*, 148(746),
1042 2299-2324.

1043 Fernando, H.J.S., Gultepe, I., Dorman, C., Pardyjak, E., Wang, Q., Hoch, S., Richter, D.,
1044 Creegan, E., Gaberšek, S., Bullock, T., Hocut, C., Chang, R., Alappattu, D., Dimitrova,
1045 R., Flagg, D., Grachev, A., Krishnamurthy, R., Singh, D.K., Lozovatsky, I., Nagare, B.,
1046 Sharma, A., Wagh, S., Wainwright, C., Wroblewski, M., Yamaguchi, R., Bardeel, S.,
1047 Coppersmith, R., Chisholm, N., Gonzalez, E., Gunawardena, N., Hyde, O., Morrison,
1048 T., Olson, A., Perelet, A., Perrie, W., Wang, S., and Wauer, B., 2021: C-FOG: Life of
1049 Coastal Fog. *Bull. Amer. Meteor. Soc.*, 102(2).

1050 Freitas, G.P., Stolle, C., Kaye, P.H., Stanley, W., Herlemann, D.P.R., Salter, M.E., and Zieger,
1051 P., 2022: Emission of Primary Bioaerosol Particles from Baltic Seawater. *Environ. Sci.*
1052 *Atmos*, 2, 1170–1182.

1053 Gaberšek, S., Gapp, N., Fernando, H.J.S., Ruiz-Plancarte, J., Ortiz-Suslow, D.G., Wang, Q.,
1054 Pardyjak E., Hoch, S., Gultepe, I., and Dorman C., 2024: Fog clearing in the lee of an
1055 isolated, flat island: A fog shadow. *Quart. J. Roy. Meteor. Soc.*, Submitted.

1056 Gautam, R. and Singh, M.K., 2018: Urban heat island over Delhi punches holes in widespread
1057 fog in the Indo-Gangetic Plains. *Geophys. Res. Letts.* 45(2), 1114-1121.

1058 Ge, X., Zhang, Q., Sun, Y., Ruehl, C.R. and Setyan, A., 2012: Effect of aqueous-phase
1059 processing on aerosol chemistry and size distributions in Fresno, California, during
1060 wintertime. *Env. Chem.*, 9(3), 221-235.

1061 Gerber, H.E., 1981: Microstructure of a radiation fog. *J. Atmos. Sci.*, 38(2), 454-458.

1062 Goldschmidt, V.W. and Householder, M.K., 1969: The Hot Wire anemometer as an Aerosol
1063 Droplet Size Sampler. *Atmos. Env.*, 3(6), pp.643-651.

1064 Grare, L., Statom, N.M., Pizzo, N. and Lenain, L., 2021: Instrumented wave gliders for air-sea
1065 interaction and upper ocean research. *Front. Marine Sci.*, 8, 664728.

1066 Greenfield, S.M., 1957: Rain scavenging of radioactive particulate matter from the
1067 atmosphere. *J. Atmos. Sci.*, 14, 115–125. [https://doi.org/10.1175/1520-](https://doi.org/10.1175/1520-0469(1957)014<0115:RSORPM>2.0.CO;2)
1068 [0469\(1957\)014<0115:RSORPM>2.0.CO;2](https://doi.org/10.1175/1520-0469(1957)014<0115:RSORPM>2.0.CO;2)

1069 Grell, G. A. and Freitas, S. R., 2014: A Scale and Aerosol Aware Stochastic Convective
1070 Parameterization for Weather and Air Quality Modeling, . *Atmos. Chem. Phys.*, 14,
1071 5233–5250. <https://doi.org/10.5194/acp-14-5233-2014>.

1072 Gultepe, I., Müller, M.D. and Boybeyi, Z., 2006: A new visibility parameterization for warm-
1073 fog applications in numerical weather prediction models. *J. App. Meteor. Climatol.*
1074 45(11): 1469–1480.

1075 Gultepe, I., Pearson, G., Milbrandt, J.A., Hansen, B., Platnick, S., Taylor, P., Gordon, M.,
1076 Oakley, J.P. and Cober, S.G., 2009: The fog remote sensing and modeling field project.
1077 *Bull. Amer. Meteor. Soc.*, 90, 341–359

1078 Gultepe, I., Fernando, H.J.S, Pardyjak, E.R., Hoch, S.W., Silver, Z., Creegan, E., Leo, L.S.,
1079 Pu, Z., De Wekker, S.F.J., and Hang, C., 2016: An Overview of the MATERHORN
1080 Fog Project: Observations and Predictability. *Pure App. Geophys.*, 173 (9), 2983–3010.

1081 Gultepe, I., Heymsfield, A.J., Fernando, H.J.S., Pardyjak, E., Dorman, C.E., Wang, Q.,
1082 Creegan, E., Hoch, S.W., Flagg, D.D., Yamaguchi, R. and Krishnamurthy, R., 2021: A
1083 review of coastal fog microphysics during C-FOG. *Bound. Layer Meteor.*, 181, 227-
1084 265.

1085 Hintz, T.J., Huang, K.Y., Hoch, S.W., Bardoel, S.L., Gaberšek, S., Gultepe, I., Ruiz-Plancarte,
1086 J., Pardyjak, E.R., Wang, Q. and Fernando, H.J.S, 2024: A mechanism for coastal fog
1087 genesis at evening transition. *Quart. J. Roy. Meteor. Soc.*, 150(762), 2727-2743.

1088 Hersbach, H., Bell, B., Berrisford, P., Biavati, G., Horányi, A., Muñoz Sabater, J., Nicolas, J.,
1089 Peubey, C., Radu, R., Rozum, I., Schepers, D., Simmons, A., Soci, C., Dee, and D.,

1090 Thépaut, J.-N. 2023: ERA5 Hourly Data on Pressure Levels from 1940 to Present.
 1091 *Copernicus Climate Change Service (C3S) Climate Data Store (CDS)*.

1092 Hong, S.Y., Noh, Y., and Dudhia, J., 2006: A New Vertical Diffusion Package with an Explicit
 1093 Treatment of Entrainment Processes. *Mon. Wea. Rev.*, 134, 2318–2341.
 1094 <https://doi.org/10.1175/MWR3199.1>.

1095 Hodur, R. M., 1997: The Naval Research Laboratory’s Coupled Ocean/Atmosphere Mesoscale
 1096 Prediction System (COAMPS). *Mon. Wea. Rev.*, 125, 1414–1430.

1097 Huang, S., Hu, W., Chen, J., Wu, Z., Zhang, D., and Fu, P. 2021: Overview of biological ice
 1098 nucleating particles in the atmosphere. *Environ. International*, 146, 106197.

1099 Huang, Kelly, Hintz, T., and Kit, E., and Fernando, H.J.S., 2024: An Equilibrium Radius of
 1100 Fog Droplets in Turbulent Environments, *In preparation*.

1101 Isaac, G.A., Bullock, T., Beale, J. and Beale, S., 2020: Characterizing and Predicting Marine
 1102 Fog Offshore Newfoundland and Labrador. *Wea. Forecast.*, 35(2), 347-365.

1103 Jiménez, P.A., Dudhia, J., Gonzalez-Rouco, J.F., Navarro, J., Montavez, J.P., Garcia-
 1104 Bustamante, E., 2012: A revised scheme for the WRF surface layer formulation. *Mon.*
 1105 *Wea. Rev.*, 140, 898-918.

1106 Jumper, E.J. and Gordeyev, S., 2017: Physics and Measurement of Aero-Optical Effects: Past
 1107 and Present. *Ann. Rev. Fluid Mech.*, 49, 419-441.

1108 Jung, J., Furutani, H., Uematsu, M., Kim, S. and Yoon, S., 2013: Atmospheric inorganic
 1109 nitrogen input via dry, wet, and sea fog deposition to the subarctic western North Pacific
 1110 Ocean. *Atmos. Chem Phys*, 13(1), 411-428.

1111 Karimi, M., 2020: Direct Numerical Simulation of Fog: The Sensitivity of a Dissipation Phase
 1112 to Environmental Conditions. *Atmos.*, 11(1), 12 doi:10.3390/atmos11010012.

1113 Kecorius, S., Hoffmann, E.H., Tilgner, A., Barrientos-Velasco, C., van Pinxteren, M.,
 1114 Zeppenfeld, S., Vogl, T., Madueño, L., Lovrić, M., Wiedensohler, A. and Kulmala, M.,
 1115 2023: Rapid growth of Aitken-mode particles during Arctic summer by fog chemical
 1116 processing and its implication. *PNAS nexus*, 2(5), 124.

1117 Kit, E., Hocut, C.M., Liberzon, D. and Fernando, H.J.S., 2017: Fine-scale turbulent bursts in
 1118 stable atmospheric boundary layer in complex terrain. *J. Fluid Mech.*, 833, 745-772.

1119 Köhler, H., 1936: The Nucleus in and the Growth of Hygroscopic Droplets. *Trans. Faraday*
 1120 *Soc.*, 32, 1152-1161.

1121 Koračin, D. and Dorman, C.E. eds., 2017: *Marine fog: Challenges and Advancements in*
 1122 *Observations, Modeling, and Forecasting*. Springer.

- 1123 Koračin, D., Lewis, J., Thompson, W.T., Dorman, C.E. and Businger, J.A., 2001: Transition
1124 of Stratus into Fog along the California Coast: Observations and Modeling. *J. Atmos.*
1125 *Sci.*, 58(13), 1714-1731.
- 1126 Koračin, D., Dorman, C.E., Lewis, J.M., Hudson, J.G., Wilcox, E.M. and Torregrosa, A., 2014:
1127 Marine Fog: A Review. *Atmos. Res.*, 143, 142-175.
- 1128 Knopf, D.A., Alpert, P.A. and Wang, B., 2018: The Role of Organic Aerosol in Atmospheric
1129 Ice Nucleation: A Review. *ACS Earth and Space Chem.*, 2(3), 168-202.
- 1130 Leipper, D.F., 1994: Fog on the U.S. West Coast, a Review. *Bull. Amer. Meteor. Soc.*, 72, 229–
1131 240.
- 1132 Lakra, K. and Avishek, K., 2022: A Review on Factors Influencing Fog Formation,
1133 Classification, Forecasting, Detection and Impacts. *Rendiconti Lincei. Scienze Fisiche*
1134 *e Naturali*, 33(2), 319-353.
- 1135 Lozovatsky, I., Wainwright, C., Creegan, E., and Fernando, H.J.S., 2021: Ocean Turbulence
1136 and Mixing near the Shelf Break Southeast of Nova Scotia, *Bound. Layer Meteor.*, 181,
1137 425–441, <https://doi.org/10.1007/s10546-020-00576-z>
- 1138 MacDonald, M., Kurowski, M.J. and Teixeira, J., 2020: Direct numerical simulation of the
1139 moist stably stratified surface layer: Turbulence and Fog Formation. *Bound. Layer*
1140 *Meteor.*, 175(3), 343-368.
- 1141 Mansell, E.R., Ziegler, C. L., and Bruning, E. C., 2010: Simulated electrification of a small
1142 thunderstorm with two-moment bulk microphysics. *J. Atmos. Sci.*, 67(1), 171-194,
1143 <https://doi.org/10.1175/2009JAS2965.1>.
- 1144 Meng, Z. and Seinfeld, J.H., 1994: On the Source of the Submicrometer Droplet Mode of Urban
1145 and Regional Aerosols. *Aero. Sci. Tech.*, 20(3), 253-265.
- 1146 Mlawer, E.J., Taubman, S.J., Brown, P.D., Iacono, M.J., and Clough, S.A., 1997: Radiative
1147 transfer for inhomogeneous atmospheres: RRTM, a validated correlated-k model for
1148 the longwave. *J. Geophys. Res.: Atmos.*, 102(D14), 16663–16682,
1149 <https://doi.org/10.1029/97JD00237>.
- 1150 Myers, J.N., 1968: Fog, *Sci. Amer.*, 219(6), 74-83.
- 1151 Nakanishi, M., 2000: Large-eddy Simulation of Radiation Fog. *Bound. Layer Meteor.*, 94(3),
1152 461–493.
- 1153 Nakanishi, M., and Nino, H., 2006: An improved Mellor_Yamada level-3 model: its numerical
1154 stability and application to a regional prediction of advection fog. *Bound. Layer*
1155 *Meteor.*, 119, 397–407, <https://doi.org/10.1007/s10546-005-9030-8>.

- 1156 Niece, M., and Kaiser, C., 2018: Directed Energy Outreach. *Proc. Directed Energy*
 1157 *Educational Outreach Campaign*, Directed Energy Professional Society, 11,
 1158 <https://www.deps.org/DEPSpages/DEoutreach.html>
- 1159 NWS 2024: Super Fog, <https://www.weather.gov/safety/fog-super> (Accessed Apr 25, 2024)
- 1160 Ortiz-Suslow, D., Ruiz-Plancarte J., Yamaguchi R., Kalogiros, J., Fernando, H.J.S, Creegan,
 1161 E., Pardyjack, E., Gaberšek, S., Gultepe, I., and Wang, Q., 2024: A Case Study of
 1162 Boundary Layer Development Downstream of a Small Maritime Island, *Quart. J. Roy.*
 1163 *Meteor. Soc.*, Submitted.
- 1164 Pawlak, R.J., 2012: Recent developments and near term directions for Navy laser weapons
 1165 system (LaWS) testbed. *High-Power Lasers 2012: Technology and Systems* (Vol.
 1166 8547, p. 854705). International Society for Optics and Photonics.
 1167 <https://doi.org/10.1117/12.976031>.
- 1168 Perram, G.P., Cusumano, S.J., Hengehold, R.L., and Fiorino, S.T., 2010: *An introduction to*
 1169 *laser weapon systems*. Hard back Textbook, 463 Pages, Directed Energy Professional
 1170 Society.
- 1171 Place, B.K., Young, C.J., Ziegler, S.E., Edwards, K.A., Salehpoor, L. and VandenBoer, T.C.,
 1172 2018. Passive sampling capabilities for ultra-trace quantitation of atmospheric nitric
 1173 acid (HNO₃) in remote environments. *Atmos. Environ.*, 191, 360-369.
- 1174 Poku, C., Ross, A.N., Blyth, A.M., Hill, A.A. and Price, J.D., 2019: How important are aerosol–
 1175 fog interactions for the successful modelling of nocturnal radiation fog? *Wea.*, 74(7),
 1176 237-243.
- 1177 Pollard, R., Rhines, P., and Thompson, R., 1972: The Deepening of the Wind-Mixed Layer.
 1178 *Geophys. Fluid Dyn.*, 4(4), 381–404.
 1179 <https://www.tandfonline.com/doi/abs/10.1080/03091927208236105>
- 1180 Pruppacher, H.R. and Klett, J.D., 2010: Microstructure of atmospheric clouds and
 1181 precipitation. *Microphys. Clouds and Precip.*, 10-73. Springer, Dordrecht.
- 1182 Pu, Z., Pardyjak, E.R., Hoch, S.W., Gultepe, I., Hallar, A.G., Perelet, A., Beal, R., Carrillo-
 1183 Cardenas, G., Li, X., Garcia, M. and Oncley, S., 2023: Cold Fog Amongst Complex
 1184 Terrain. *Bull. Amer. Meteor. Soc.*, 104(11), E2030-E2052.
- 1185 Richter, D.H., MacMillan, T. and Wainwright, C., 2021: A Lagrangian Cloud Model for the
 1186 Study of Marine Fog. *Bound. Layer Meteor.*, 1-20.
- 1187 Rodhe, B., 1962: The Effect of Turbulence on Fog Formation. *Tellus*, 14(1), 49-86.

- 1188 Salehpoor, L. and VandenBoer, T.C., 2023: Suppressor and calibration standard limitations in
1189 cation chromatography of ammonium and 10 alkylamines in atmospheric samples.
1190 *Analy. Methods*, 15(31), 3822-3842.
- 1191 Sasakawa, M., Ooki, A. and Uematsu, M., 2003: Aerosol size distribution during sea fog and
1192 its scavenge process of chemical substances over the northwestern North Pacific. *J.*
1193 *Geophys. Res.: Atmos.*, 108(D3).
- 1194 Schiffer, J.M., Mael, L.E., Prather, K.A., Amaro, R.E. and Grassian, V.H., 2018: Sea Spray
1195 Aerosol: Where Marine Biology Meets Atmospheric Chemistry. *ACS Central*
1196 *Sci.*, 4(12), 1617-1623.
- 1197 Shin, H H., and Hong, S. Y., 2015: Representation of the Subgridscale Turbulent Transport in
1198 Convective Boundary Layers at Gray-Zone Resolutions. *Mon. Wea. Rev.*, 143, 250–
1199 271, <https://doi.org/10.1175/MWR-D-14-00116.1>.
- 1200 Skamarock, W.C., Klemp, J.B., Dudhia, J., Gill, D.O., Barker, D., Duda, M.G., Huang, X.,
1201 Wang, W., and Powers, J. G., 2008: A Description of the Advanced Research WRF
1202 Version 3. NCAR Tech Rep (NCAR/TN-475+STR), University Corporation for
1203 Atmospheric Research, <http://dx.doi.org/10.5065/D68S4MVH>.
- 1204 Singh, D.K., Hoch, S.W., Gultepe, I. and Pardyjak, E.R., 2024: A Case study of the Life Cycle
1205 of a Stratus-Lowering Coastal-Fog Event in Newfoundland, Canada. *Quart. J. Roy.*
1206 *Meteor. Soc.*, 150(759), 641-662.
- 1207 Soveizi, N., Latifi, A.M., Mehrabian, S. and Akhavan Sepahi, A., 2023: Bacterial Ice
1208 Nucleation Proteins: Features, Structure, and Applications. *J. App. Biotech. Rep*, 10(3),
1209 1041-1054.
- 1210 Spirig, R., Vogt, R., Larsen, J.A., Feigenwinter, C., Wicki, A., Franceschi, J., Parlow, E., Adler,
1211 B., Kalthoff, N., Cermak, J. and Andersen, H., 2019: Probing the Fog Life Cycles in
1212 the Namib Desert. *Bull. Amer. Meteor. Soc.*, 100(12), 2491-2507.
- 1213 Taylor, G.I., 1917: The Formation of Fog and Mist. *Quart. J. Roy. Meteor. Soc.*, 43, 241–268.
- 1214 Theethai J., A., Jayakumar, A., Gupta, K., Mohandas, S., Hendry, M.A., Smith, D.K., Francis,
1215 T., Bhati, S., Parde, A.N., Mohan, M. and Mitra, A.K., 2023: Implementation of the
1216 urban parameterization scheme in the Delhi model with an improved urban
1217 morphology. *Quart. J. Roy. Meteor. Soc.*, 149(750), 40-60.
- 1218 Torregrosa, A., O'Brien, T.A., and Faloon, I.C., 2014: Coastal Fog, Climate Change, and the
1219 Environment. *Eos Trans. AGU*, 95(50), 473–474.
- 1220 Vladimirov, E., Dimitrova, R., and Danchovski, V., 2018: Sensitivity of WRF Model Results
1221 to Topography and Land Cover: Study for the Sofia Region. *Annuaire de l'Université*

1222 *de Sofia "St. Kliment Ohridski", Faculté de Physique, 111, 87-101,*
1223 https://www.phys.uni-sofia.bg/annual/archive/111/full/GSU-Fizika-111_07_color.pdf.

1224 Van der Hoven, I., 1957: Power Spectrum of Horizontal Wind Speed in the Frequency Range
1225 from 0.0007 to 900 cycles per hour. *J. Atmos. Sci.*, 14(2), 160-164.

1226 Van der Velde, I. R., Steeneveld, G. J., Schreur, B. W., and Holtslag, A. A. M., 2010: Modeling
1227 and Forecasting the Onset and Duration of Severe Radiation Fog under Frost
1228 Conditions. *Monthly Wea. Rev.*, 138(11), 4237-4253.

1229 Wagh, S., Krishnamurthy, R., Wainwright, C., Wang, S., Dorman, C.E., Fernando, H.J.S. and
1230 Gultepe, I., 2021: Study of Stratus-lowering Marine-Fog Events Observed During C-
1231 FOG. *Bound. Layer Meteor.*, 181, 317-344.

1232 Wu, S., Tao, J., Ma, N., Kuang, Y., Zhang, Y., He, Y., Sun, Y., Xu, W., Hong, J., Xie, L.,
1233 Wang, Q., Su, H., and Cheng, Y., 2022: Particle number size distribution of PM1 and
1234 PM10 in fogs and implications on fog droplet evolutions. *Atmos. Environ.*, 277,
1235 119086. <https://doi.org/10.1016/j.atmosenv.2022.119086>.

1236 WMO, 1992: *International Meteor. Vocabulary*. WMO, Geneva, Switzerland.

1237 Yamaguchi, R., Ruiz-Plancarte, J., Ortiz-Suslow, D. G., Chang, R., Creegan, E. D., Fernandez,
1238 D., Kalogiros, J. A., Fernando, H. J. and Wang, Q., 2024: A shipboard atmospheric
1239 surface layer profiling system for air-sea interaction and fog studies. In Preparation for
1240 *Quart. Jour. Royal Meteor. Soc.*

1241 Zhao, S., Yan, J., Lin, Q., Yao, L., Park, K., Jung, J., Chen, L., Xu, S., Sun, M., Wang, S. and
1242 Yang, H., 2022. Changes in aerosol particle composition during sea fog formation
1243 events in the sea ice regions of the Arctic Ocean. *Atmos. Environ.*, 272, 118943.6.

1244